

Super*B* Progress Reports

The Detector

March 15, 2010

Abstract

This report details the progress made in by the Super*B* Project in the area of the Detector since the publication of the Super*B* Conceptual Design Report in 2007 and the Proceedings of Super*B* Workshop VI in Valencia in 2008.

Contents

1	Introduction	1
1.1	The Physics Motivation	1
1.2	The Super <i>B</i> Project Elements	1
1.3	The Detector Design Progress Report	2
2	Overview	2
2.1	Physics Performance	3
2.2	Challenges on Detector Design	6
2.3	Open Issues	6
2.4	Detector R&D	7
3	Silicon Vertex Tracker	9
3.1	Detector concept	9
3.1.1	SVT and Layer0	9
3.1.2	Performance Studies	9
3.1.3	Background Conditions	11
3.2	Layer0 options under study	12
3.2.1	Triplets	12
3.2.2	Hybrid Pixels	12
3.2.3	MAPS	12
3.2.4	Pixel Module Integration	13
3.3	A MAPS-based all-pixel SVT using a deep P-well process	14
3.4	R&D Activities	16
4	Drift Chamber	17
4.1	System Design	17
4.1.1	Backgrounds	17
4.2	Mechanical Structure	18
4.3	Drift Chamber Geometry	18
4.4	Gas Mixture	18
4.5	Cell Design and Layout	19
4.6	R&D work	19
5	Particle Identification	21
5.1	Detector concept	21
5.1.1	Charged particle identification at Super <i>B</i>	22
5.1.2	<i>BABAR</i> DIRC	22
5.2	Barrel PID at Super <i>B</i>	23
5.2.1	Performance optimization	23
5.2.2	Design and R&D status	25
5.3	Forward PID at Super <i>B</i>	26
5.3.1	Motivation for a forward PID detector	26
5.3.2	Forward PID requirements	27
5.3.3	Status of the forward PID R&D effort	27

6	Electromagnetic Calorimeter	30
6.1	Barrel Calorimeter	30
6.2	Forward Endcap Calorimeter	31
6.3	Backward Endcap Calorimeter	33
6.4	R&D	36
6.4.1	Barrel Calorimeter	36
6.4.2	Forward Calorimeter	38
6.4.3	Backward Calorimeter	38
7	Instrumented Flux Return	39
7.1	Performance optimization	39
7.1.1	Identification Technique	39
7.1.2	Baseline Design Requirements	39
7.1.3	Design optimization and performance studies	40
7.2	R&D	41
7.2.1	R&D tests and results	41
7.2.2	Prototype	42
7.3	Baseline Detector Design	43
7.3.1	Flux Return	43
8	Electronics, Trigger, DAQ and Online	44
8.1	Overview of the Architecture	44
8.1.1	Trigger Strategy	44
8.1.2	Trigger Rates and Event Size Estimation	46
8.1.3	Dead Time and Buffer Queue Depth Considerations	46
8.2	Electronics, Trigger and DAQ	46
8.2.1	Fast Control and Timing System	47
8.2.2	Clock, Control and Data Links	48
8.2.3	Common Front-End Electronics	49
8.2.4	Readout Module	50
8.2.5	Experiment Control System	50
8.2.6	Level 1 Hardware Trigger	51
8.3	Online System	52
8.3.1	ROM Readout and Event Building	53
8.3.2	High Level Trigger Farm	53
8.3.3	Data Logging	53
8.3.4	Event Data Quality Monitoring and Display	53
8.3.5	Run Control System	54
8.3.6	Detector Control System	54
8.3.7	Other Components	54
8.3.8	Software Infrastructure	54
8.4	Front-End Electronics	55
8.4.1	SVT Electronics	55
8.4.2	DCH Electronics	55
8.4.3	PID Electronics	56
8.4.4	EMC Electronics	57
8.4.5	IFR Electronics	59
8.5	R&D	60

8.6	Conclusions	60
9	Software and Computing	61
9.1	The baseline model	61
9.1.1	The requirements	62
9.2	Computing tools and services for the Detector TDR studies	63
9.2.1	Detector fast simulation	63
9.2.2	Bruno: the SuperB full simulation tool	63
9.3	Simulation output: Hits and MonteCarlo Truth	63
9.4	Staged simulation	63
9.5	Interplay with fast simulation	64
9.5.1	The distributed production environment	64
9.5.2	The software development and collabaritive tools	64
10	Mechanical Integration	65
11	Budget and Schedule	65
11.1	Detector Costs	66
11.2	Schedule	71

1 Introduction

1.1 The Physics Motivation

The Standard Model successfully explains the wide variety of experimental data that has been gathered over several decades with energies ranging from under a GeV up to several hundred GeV. At the start of the millennium, the flavor sector was perhaps less explored than the gauge sector, but the PEP-II and KEK-B asymmetric B Factories, and their associated experiments *BABAR* and Belle, have produced a wealth of important flavor physics highlights during the past decade [1]. The most notable experimental objective, the establishment of the Cabibbo-Kobayashi-Maskawa phase as consistent with experimentally observed CP-violating asymmetries in B meson decay, was cited in the award of the 2008 Nobel Prize to Kobayashi & Maskawa [2].

The B Factories have provided a set of unique, over-constrained tests of the Unitarity Triangle. These have, in the main, been found to be consistent with Standard Model predictions. The B factories have done far more physics than originally envisioned; *BABAR* alone has published more than 400 papers in refereed journals to date. Measurements of all three angles of the Unitarity Triangle - $\sin 2\alpha$ and γ , in addition to $\sin 2\beta$; the establishment of $D^0\bar{D}^0$ mixing; the uncovering of intriguing clues for potential New Physics in $B \rightarrow K^{(*)}l^+l^-$ and $B \rightarrow K\pi$ and decays; and unveiling an entirely unexpected, new spectroscopy, are some examples of important experimental results beyond those initially contemplated.

With the LHC now beginning operations, the major experimental discoveries of the next few years will probably be at the energy frontier, where we would hope not only to complete the Standard Model by observing the Higgs particle, but to find signals of New Physics which are widely expected to lie around the 1 TeV energy scale. If found, the New Physics phenomena will need data from very sensitive heavy flavor

experiments if they are to be understood in detail. Determining the nature of the New Physics involved requires the information on rare b, c and τ decays, and on CP violation in b and c quark decays that only a very high luminosity asymmetric B Factory can provide [3]. On the other hand, if such signatures of New Physics are not observed at the LHC, then the excellent sensitivity provided at the luminosity frontier by Super*B* provides another avenue to observing New Physics at mass scales up to 10 TeV or more through observation of rare processes involving B and D mesons and studies of LFV in τ decays.

1.2 The Super*B* Project Elements

It is generally agreed that the physics being addressed by a next-generation B factory requires a data sample that is some 50-100 times larger than the existing combined sample from *BABAR* and Belle, or at least $50\text{-}75\text{ ab}^{-1}$. Acquiring such an integrated luminosity in a 5 year time frame requires that the collider run at a luminosity of at least $10^{36}\text{ cm}^{-2}\text{ s}^{-1}$.

For a number of years, an Italian led, INFN hosted, collaboration of scientists from Canada, Italy, Israel, France, Norway, Spain, Poland, UK and the US have worked together to design and propose a high luminosity 10^{36} asymmetric B Factory project, called Super*B* to be built at or near the Frascati laboratory [4]. The project, which is managed by a project board, includes divisions for the accelerator, the detector, the computing, and the site & facilities.

The accelerator portion of the project employs lessons learned from modern low-emittance synchrotron light sources and ILC/CLIC R&D, and an innovative new idea for the intersection region of the storage rings [5], called crab waist, to reach luminosities over 50 times greater than those obtained by earlier B factories at KEK and SLAC. There is now an attractive, cost-effective accelerator design, including polarization, which is being further refined and optimized [6]. It is designed to incorporate many PEP-II components. This facility promises to deliver fundamen-

tal discovery-level science at the luminosity frontier.

There is also an active international proto-collaboration working effectively on the design of the detector. The detector team draws heavily on its deep experience with the *BABAR* detector, which has performed in an outstanding manner both in terms of scientific productivity and operational efficiency. *BABAR* serves as the foundation of the upgraded Super*B* detector.

To date, the project has been very favorably reviewed by several international committees. This international community now awaits a decision by the Italian government on its support of the Super*B* project.

1.3 The Detector Design Progress Report

This document describes the design and development of the Super*B* detector, which is based on a major upgrade of *BABAR*. This is one of several descriptive "Design Progress Reports (DPR)" being produced by the Super*B* project during the first part of 2010 to motivate and summarize the development, and present status of each major division of the project (Physics, Accelerator, Detector, and Computing) so as to present a snapshot of the entire project at a intermediate stage between the CDR, which was written in 2007, and the TDR that is being developed during the next year.

This "Detector DPR" begins with a brief overview of the detector design, the challenges involved in detector operations at the luminosity frontier, the approach being taken to optimize the remaining general design choices, and the R&D program that is underway to develop and validate the system and subsystem designs. Each of the detector subsystems and the general detector systems are then described in more detail, followed by a description of the integration and assembly of the full detector. Finally, the paper concludes with a discussion of detector costs and a schedule overview.

References

- [1] C. Amsler *et al.* (Particle Data Group), Physics Letters B667, 1 (2008).
- [2] http://nobelprize.org/nobel_prizes/physics/laureates/2008/press.html, and <http://www-public.slac.stanford.edu/babar/Nobel2008.htm>.
- [3] D. Hitlin *et al.* "Proceedings of Super*B* Workshop VI: New Physics at the Super Flavor Factory"; arXiv:0810.1312v2 [hep-ph].
- [4] M. Bona *et al.* "Super*B*: A High-Luminosity Heavy Flavour Factory: Conceptual Design Report"; arXiv:0709.0451v2 [hep-ex], INFN/AE - 07/2, SLAC-R-856, LAL 07-15.
- [5] P. Raimondi, 2nd LNF Workshop on Super*B*, Frascati, Italy, March 16-18 2006, and Proceedings of the 2007 Particle Accelerator Conference (PAC 2007) Albuquerque, New Mexico, USA, June 25-29.
- [6] Design Progress Report for the Super*B* Accelerator (2010) in preparation.

2 Overview

The Super*B* detector concept is based on the *BABAR* detector, with those modifications required to operate at a luminosity of 10^{36} or more, and with a reduced center-of mass boost. Further improvements needed to cope with higher beam-beam and other beam-related backgrounds, as well as to improve detector hermeticity and performance, are also discussed, as is the necessary R&D required to implement this upgrade. Cost estimates and the schedule are described in Section ??.

The current *BABAR* detector consists of a tracking system with a 5 layer double-sided silicon strip vertex tracker (SVT) and a 40 layer drift chamber (DCH) inside a 1.5T magnetic

field, a Cherenkov detector with fused silica bar radiators (DIRC), an electromagnetic calorimeter (EMC) consisting of 6580 CsI(Tl) crystals and an instrumented flux-return (IFR) comprised of both limited streamer tube (LST) and resistive plate chamber (RPC) detectors for K_L^0 detection and μ identification.

The Super B detector concept reuses a number of components from *BABAR*: the flux-return steel, the superconducting coil, the barrel of the EMC and the fused silica bars of the DIRC. The flux-return will be augmented with additional absorber to increase the number of interactions lengths for muons to roughly 7λ . The DIRC camera will be replaced by multi-channel plate (MCP) photon detectors in focusing configuration with fused silica optics to reduce the impact of beam related backgrounds and improve performance. The forward EMC will feature cerium-doped LSO (lutetium orthosilicate) or LYSO (lutetium yttrium orthosilicate) crystals, hereafter referred to as L(Y)SO crystals, which have a much shorter scintillation time constant, a lower Molière radius and better radiation hardness than the current CsI(Tl) crystals, again for reduced sensitivity to beam backgrounds and better position resolution.

The tracking detectors for Super B will be new. The current SVT cannot operate at $\mathcal{L} = 10^{36}$, and the DCH has reached the end of its design lifetime and must be replaced. To maintain sufficient Δt resolution for time-dependent CP violation measurements with the Super B boost of $\beta\gamma = 0.24$, the vertex resolution will be improved by reducing the radius of the beam pipe, placing the inner-most layer of the SVT at a radius of roughly 1.2 cm. This innermost layer of the SVT will be constructed of either silicon triplets or MAPS or other pixelated sensors, depending on the estimated occupancy from beam-related backgrounds. Likewise the cell size and geometry of the DCH will be driven by occupancy considerations. The hermeticity of the Super B detector, and thus its performance for certain physics channels will be improved by including a backwards "veto-quality" EMC detector comprising a lead-scintillator stack. The

justification for inclusion of a forward PID is less clear on balance and remains under study. The baseline design concept is a fast Cherenkov light-based time-of-flight system.

[WE NEED A NEW FIGURE.]

The Super B detector concept is shown in Fig. 1. The top portion of this elevation view shows the minimal set of new detector components, with the most reuse of current *BABAR* detector components; the bottom half shows the configuration of new components required to cope with higher beam backgrounds and to achieve greater hermeticity.

2.1 Physics Performance

The Super B detector design as described in the Conceptual Design Report [1] left open a number of questions that have a large impact on the overall detector geometry. The main ones include estimating the effect of a PID device in front of the forward EMC, the need of an EMC in the backward region, the position of the innermost layer of the SVT and its internal geometry, the SVT-DCH transition radius, and the amount and distribution of absorber in the IFR.

The study of these options has been performed by evaluating the physics reach of a set of benchmark decay channels or the overall performance in the reconstruction of charged and neutral particles. To accomplish this task a fast simulation specifically developed for Super B has been used (sec. 9), combined with a complete set of analysis tools inherited for the most part from the BaBar experiment. The main sources of background have also been simulated to estimate the subsystems occupancy as a function of the position. The main results of the ongoing performance studies are summarized in this section.

Time-dependent measurements are an important part of the Super B physics program. To keep a time resolution comparable to what was measured at *BABAR*, the Super B reduced boost must be compensated with a much better vertex resolution by placing the innermost layer of the SVT (Layer0) as close as possible to the IP. The main factor limiting the minimum distance from

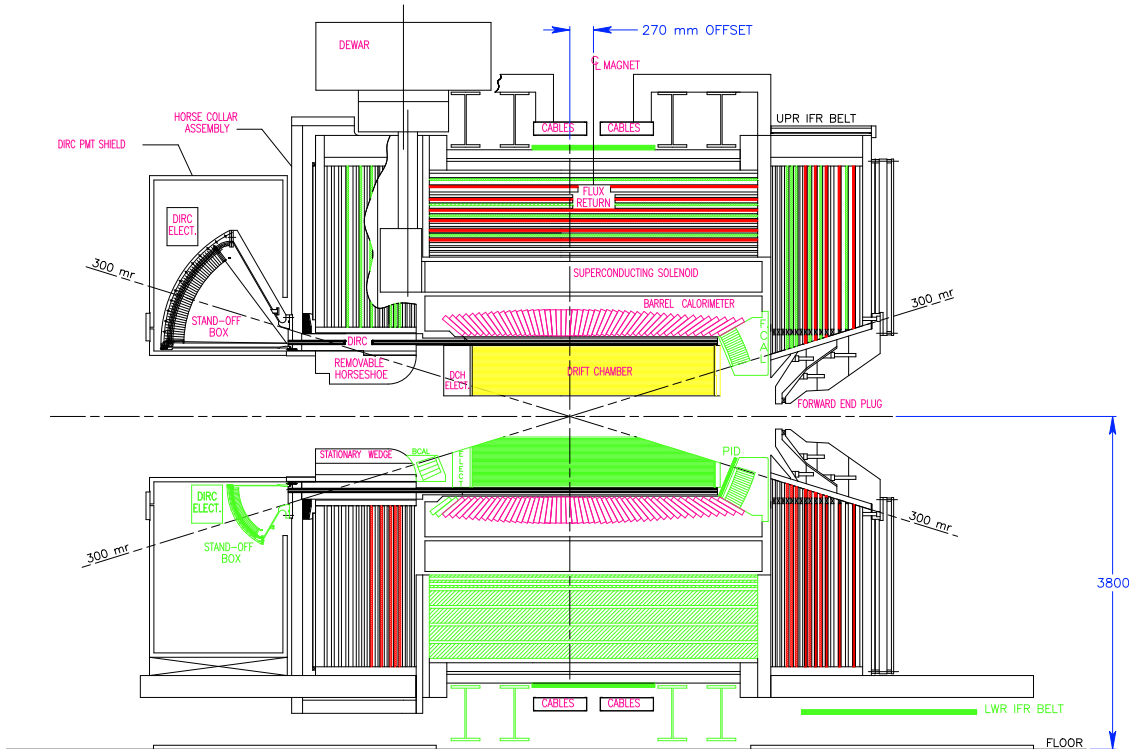


Figure 1: Concept for the SuperB detector. The upper half shows the baseline concept, and the bottom half adds a number of detector optional configurations.

the IP is the hit rate from $e^+e^- \rightarrow e^+e^-e^+e^-$ background events. In this context the performances of the hybrid pixels (1.08% X_0 , $14\mu\text{m}$ hit reso.) and triplets (0.40% X_0 , $8\mu\text{m}$ hit reso.) have been compared. Simulation studies of $B^0 \rightarrow \Phi K_S^0$ decays have shown that with the boost $\beta\gamma = 0.28$ the hybrid pixels and the triplets reach a $\sin 2\beta_{\text{eff}}$ per event error equal to *BABAR* at a distance of 1.5 cm and 2.0 cm, respectively. With $\beta\gamma = 0.24$ the error increases by 7-8%. Similar conclusions apply to $B^0 \rightarrow \pi^+\pi^-$. These results will help deciding what is the most appropriate technology and position for the Layer0.

The *BABAR* SVT five-layer design was motivated by the request of standalone tracking for low- p_T tracks and redundancy in case several modules failed during operations. The default SuperB SVT design consisting of a Layer0 plus a *BABAR*-like SVT detector has been compared with two alternative models made of a total

of 5 or 4 layers. Studies of track parameters resolutions and $B \rightarrow D^*K$ kinematic variables and reconstruction efficiency have shown that when the number of layers is reduced the low- p_T track efficiency decreases significantly, while the tracks quality is basically unaffected. These results support a six-layer layout.

Studies have also shown that the best overall SVT+DCH tracking performance would be achieved when the outer radius of the SVT is kept small (14 cm as in *BABAR* or even less) and the inner wall of the DCH is as close to the SVT as possible. However, though in the SuperB detector there is not a fixed support tube as there was in *BABAR*, space between SVT and DCH must be left to allocate a removable support structure to be inserted when access to the inner part of the detector is needed. This constraint is expected to limit the minimum DCH inner radius to about 20-25 cm.

The estimate of the impact of a forward PID device is done analyzing the physics reach in channels such as $B \rightarrow K^{(*)}\nu\bar{\nu}$ by weighting the advantage of having a better PID information in the forward region with the drawbacks arising from more material in front of the EM calorimeter and a slightly shorter DCH. Three detector configurations have been compared: *BABAR*, the *SuperB* baseline (no forward PID device), and the configuration with the addition of a time-of-flight detector between the DCH and the forward EMC. The results for the decay mode $B \rightarrow K\nu\bar{\nu}$ with the tag side reconstructed in the semileptonic modes are reported in Fig. 2. The study shows that moving from *BABAR* to the *SuperB* detector instrumented with the TOF device the precision $S/\sqrt{S+B}$ increases by about 13%, of which 7-8% arises from the increase of the overall detector acceptance because of the reduced boost and 5-6% is due to the improved pion/kaon separation in the forward region.

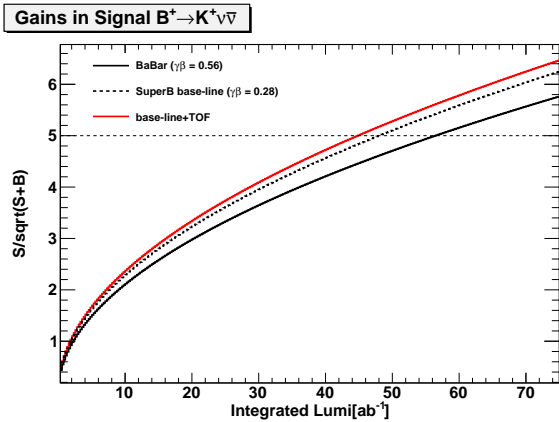


Figure 2: $S/\sqrt{S+B}$ of $B \rightarrow K\nu\bar{\nu}$ as a function of the integrated luminosity in three detector configurations.

The backward calorimeter under consideration is designed to be used in veto mode. Its impact on physics can be estimated by studying the sensitivity of rare B decays with one or more neutrinos in the final state, which benefit from having a more hermetic detection of neutrals to reduce the background contamination. One of the most important benchmark channels

of this kind is $B \rightarrow \tau\nu$. Preliminary studies indicate that when the backward calorimeter is introduced, the statistical precision $S/\sqrt{S+B}$ is enhanced by about 10%. The results are summarized in Fig. 3. The top plot shows how $S/\sqrt{S+B}$ changes as a function of the cut on E_{extra} (the total energy of charged and neutral particles that cannot be directly associated with the reconstructed daughters of the signal or tag B) with and without the backward EMC. The signal is peaked at zero. The bottom plot shows the ratio of $S/\sqrt{S+B}$ as a function of the E_{extra} cut. The possibility of using the backward calorimeter as a PID time-of-flight device is under study.

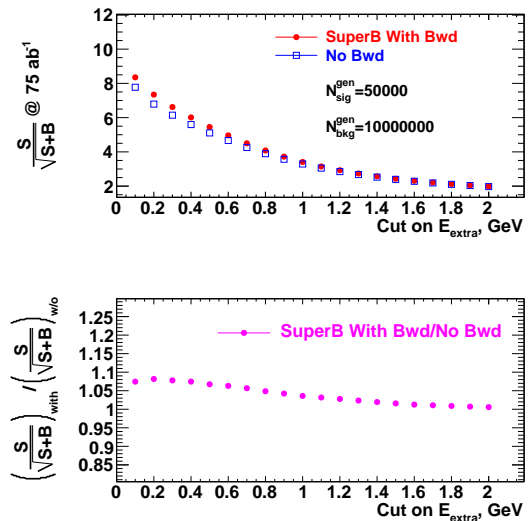


Figure 3: Top: $S/\sqrt{S+B}$ as a function of the cut on E_{extra} with (circles) and without (squares) the backward EMC. Bottom: ratio of $S/\sqrt{S+B}$ as a function of the E_{extra} cut.

The presence of a forward PID or backward EMC affects the maximum extension of the DCH and therefore the tracking and the dE/dx performance in those regions. The impact of the TOF PID detector is practically negligible because it only takes a few centimeters from the DCH. On the other hand, the effect of a forward RICH device (~ 20 cm DCH length reduction)

or the backward EMC (~ 30 cm) is somewhat larger. For example, it is found a $\sigma(p)/p$ increase of about 25% and 35% for tracks with polar angle of 23° and 150° , respectively. Even in this case, however, the overall impact is generally quite limited because only a small fraction of tracks cross the extreme forward and backward regions.

The IFR system will be upgraded by replacing the *BABAR*'s RPCs and LSTs with layers of much faster extruded plastic scintillator coupled to WLS fibers read out by APDs operated in Geiger mode. The identification of muons and K_L^0 is optimized with a GEANT4 simulation by tuning the amount of iron absorber and the distribution of the active detector layers. The current baseline design has an iron thickness of 92 cm segmented with 8 layers of scintillator. Preliminary estimates give a muon efficiency of about 87% when the pion misidentification rate is 2% (effects of background not included).

2.2 Challenges on Detector Design

The problem of the machine background is one of the leading challenges of the Super*B* project: each subsystem must be well protected to prevent deterioration from radiation damage and it must be designed so that its performances are minimally degraded because of the occupancy produced by the background hits. In effect, what is required is to achieve detector performances and operational lifetimes similar or better than those achieved in *BABAR* but at a two order of magnitude higher luminosity.

The cross section for the production of primaries background particles at the interaction point (IP) is order of 200 mb that corresponds at nominal luminosity to a rate order of 200 GHz. The main process is “radiative Bhabha” $e^+e^- \rightarrow e^+e^-\gamma$. One of the incoming beam particles loses a significant fraction of its energy by the emission of a photon then the magnetic elements downstream the IP oversteers these primaries particles into the vacuum chambers material starting electromagnetic showers whose final products are the backgrounds particles seen by the subsystem.

The particles of these electromagnetic showers can also excite the giant nuclear resonance of the material around the beam line expelling neutrons from the nucleus.

A careful optimization of the mechanical aperture of the vacuum chambers and of the optical functions is needed to keep a large stay clear for the off-energy primaries particles hence reducing the background rate.

The first Geant4 full Monte Carlo simulations of this process at Super*B* indicates that a shield around the beam line will be required to keep the electrons, positrons, photons and neutrons away from the detector both to keep occupancies and radiation damage at a comfortable level.

Besides the “radiative Bhabha” the “quasi elastic Bhabha” process was also considered. The cross section for producing a primary particle reconstructed by the detector via this process is order of 100 nb that correspond to a rate order of 100 kHz. It is reasonable to assume that this will be the driving term of the level one trigger rate. Beam gas contribution is in fact expected to be of the same order of the *BABAR* one being the nominal beam currents and the vacuum pressure in the final focus section comparables to present ones.

The final issue related to high luminosity is the production of electron positron pairs at the IP by the two photons process $e^+e^- \rightarrow e^+e^-e^+e^-$ whose total cross section evaluated at leading order with the Monte Carlo generator DIAG36 [2] is 7.3 mb that corresponds at nominal luminosity to a rate of 7.3 GHz. The pairs produced by this process are characterized by a very low transverse momentum p_t . The solenoidal magnetic shields quite efficiently the outer sub systems from this kind of background, the production rate of these particles as a function of the maximum radial extent reached is reported on Fig.4.

2.3 Open Issues

The basic geometry, structure and physics performance of the Super*B* detector is predetermined, in the main, by the retention of the

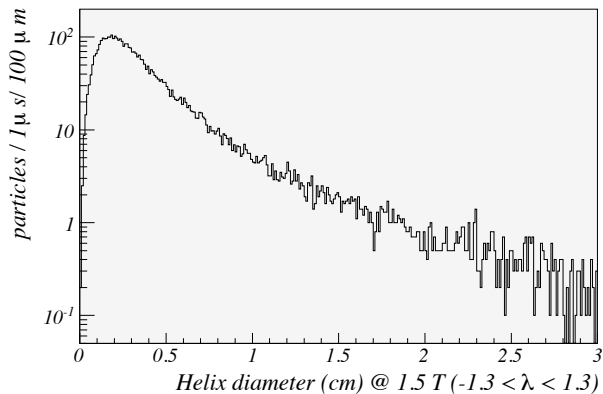


Figure 4: Production rate of particles as a function of the track helix diameter.

overall magnet, return steel, and support structure from the BaBar detector, and a number of its largest, and most expensive, subsystems. In fact, even though this fixes both the basic geometry, and much of the physics performance, it does not really constrain the expected performance of the SuperB detector in any important respect. BaBar was already a fully optimized B-factory detector for physics, and any improvements in performance that could come from changing the overall layout or rebuilding the large subsystems would be modest overall. The primary challenge for SuperB is to retain physics performance similar to BaBar in the higher background environment described in subsection 2.2, while operating at much higher ($\times 50$) data taking rates.

Within this overall constraint, optimization of the geometrical layout and new detector elements for the most important physics channels remains of substantial interest. The primary tools for sorting through the options are (1) simulation, performed under the auspices of a "Detector Geometry Working Group", that studies basic tracking, PID, and neutrals performance of different detector configurations, including their impact on each other, and studies the physics reach for a number of benchmark channels; and (2) detector R&D, including prototyping, developing new subsystem technologies, and understanding the costs, and robust-

ness of systems, as well as their impacts on each other. The first item, discussed in subsection 2.1, clearly provides guidance to the second, as discussed in subsection 2.4 and the subsystem chapters which follow, and vice versa.

At the level of the overall detector, the immediate issue is to define the detector envelopes. Optimization can and will continue for some time yet within each detector system. The studies performed to date leave us with the default detector proposal, with only a few open options remaining at the level of the detector geometry envelopes. These open issues are: (1) whether there is a forward PID detector, and, if so, at what z location does the DCH end and the EMC begin, and (2) whether there is, or is not, a backward EMC. These open issues are expected to be resolved by the Technical Board within the next few months following further studies by the Detector Geometry Working Group, in collaboration with the relevant system groups.

2.4 Detector R&D

The SuperB detector concept rests, for the most part, on well validated basic detector technology. Nonetheless, each of the detectors has many challenges due to the high rates and demanding performance requirements with R&D initiatives ongoing in all detector systems to improve the specific performance, and optimize the overall detector design. These are described in more detail in each subsystem section.

The SVT innermost layer has to provide good space resolution while coping with high background. Although silicon striplets are a viable option at moderate background levels, a pixel system would certainly be more robust against background. Keeping the material in a pixel system low enough not to deteriorate the vertexing performance is challenging, and there is considerable activity to develop thin hybrid pixels or, even better, monolithic active pixels. These devices may be part of planned upgrade path and installed as a second generation layer 0. Efforts are directed towards the development of sensors, high rate readout electronics, cooling

systems and mechanical support with low material content.

In the DCH, many parameters must be optimized for SuperB running, such as the gas mixture and the cell layout. Precision measurements of fundamental gas parameters are ongoing, as well as studies with small cell chamber prototypes and simulation of the properties of different gas mixtures and cell layouts. A possible improvement of the performance of the DCH is the innovative Cluster Counting method, in which single cluster of charge are resolved time-wise and counted, improving the resolution on the track specific ionization and the space accuracy. This technique requires significant R&D to be proven feasible in the experiment.

Though the Barrel PID system takes over major components from BaBar, the camera and readout are a significant step forward requiring extensive R&D. The challenges include the performance of pixelated PMTs for DIRC, the design of the fused silica optical system, the coupling of the fused silica optics to the existing bar boxes, the mechanical design of the camera, and the choice of electronics. Many of the individual components of the new camera are now under active study by members of the PID group, and runs are underway with a single bar prototype located in a cosmic ray telescope. A full scale (1/12 azimuth) prototype incorporating the complete optical design is planned for cosmic ray tests during the next two years.

End cap PID devices are less well understood, and whether or not they are well motivated for the overall detector remains to be demonstrated. Present R&D is centered on developing a good conceptual understanding of different proposed concepts, on simulating how their performance effects the physics performance of the detector, and on conceptual R&D for components of specific devices to validate concepts and highlight the technical and cost issues.

The EMC barrel is a well understood device at the lower luminosity of BaBar. Though there will be some technical issues associated with refurbishing, the main R&D needed at present is to understand the effects of pile-up in simula-

tion, so as to be able to design the appropriate front-end shaping time for the readout.

The forward and backward EMCs are both new devices, using cutting edge technology. Both will require one or more full beam tests, hopefully at the same time, within the next year or two. Prototypes for these test are being designed and constructed.

Systematic studies of IFR system components have been performed in a variety of bench and cosmic ray tests, leading to the present proposed design. This design will be beam tested in a full scale prototype currently being prepared for a Fermilab beam. This device will demonstrate the muon identification capabilities as a function of different iron configurations, and will also be able to study detector efficiency and spatial resolution.

At present, the Electronics, DAQ, and Trigger (ETD), have been designed for the base luminosity of $1 \times 10^{36} \text{ cm}^{-2} \text{ sec}^{-1}$, with adequate headroom. Further R&D must continue in order to understand the requirements at a luminosity up to 4 times greater, and to insure that there is a smooth upgrade path when the present design is inadequate. On a broad scale, as discussed in the system chapter, each of the many components of ETD have numerous technical challenges that will require substantial R&D as the design advances.

References

- [1] *SuperB Conceptual Design Report*, <http://www.pi.infn.it/SuperB/CDR> arXiv:0709.0451v2 [hep-ex]
- [2] F. A. Berends, P. H. Daverveldt and R. Kleiss, "Monte Carlo Simulation of Two Photon Processes. 2. Complete Lowest Order Calculations for Four Lepton Production Processes in electron Positron Collisions," *Comput. Phys. Commun.* **40**, 285 (1986).

3 Silicon Vertex Tracker

3.1 Detector concept

3.1.1 SVT and Layer0

The main task of the Silicon Vertex Tracker is to provide precise position information on charged tracks to perform measurement of time- dependent CP asymmetries in B^0 decays, which form the basis of the SuperB scientific program, as it did for the first generation of asymmetric B Factories. In addition, charged particles with transverse momenta lower than 100 MeV/c will not reach the central tracking chamber, so for these particles the SVT must provide the complete tracking information.

These goals have been reached in the BABAR detector with a five layer of silicon strip detectors, shown schematically in Fig. 5. The BaBar SVT showed excellent performance for the whole life of the experiment, thanks to a robust design that took into account the physics requirements as well as enough safety margin, to cope with the machine background, and redundancy considerations. The SuperB SVT design is based on the BaBar vertex detector layout with the addition of an innermost layer very close to the IP (Layer0). This new layer is needed, with the reduced beam energy asymmetry, to improve the vertex resolution and to keep a time resolution for CP measurement comparable to what was measured at BaBar. Physics studies and background conditions, as explained in detail in the next two sections, set stringent requirements on the Layer0 design: radius of about 1.5 cm, high granularity ($50 \times 50 \mu\text{m}^2$ pitch), low material budget (about 1% X_0), adequate radiation resistance.

For the Technical Design Report preparation several options are under study for the Layer0 technology, with different levels of maturity, expected performance and safety margin against background conditions: stripless modules based on high resistivity sensors with short strips, hybrid pixels and other thin pixel sensors based on CMOS Monolithic Active Pixel Sensor (MAPS).

The current baseline configuration for the Layer0 is based on the stripless option, being the one that gives the better physics performance, as detailed in next section. Nevertheless options with pixel sensors, more robust in high background conditions, are being developed, with specific R&D programs, in order to meet all the Layer0 requirements (i.e. low pitch and material budget, high readout speed and radiation hardness). This will allow the replacement of the Layer0 stripless modules in a "second phase" of the experiment. For this purpose the SuperB interaction region and the SVT mechanics will be designed to ensure a rapid access to the detector for a fast replacement procedure of the Layer0.

The external SVT layers (1-5), with a radius between 3 and 15 cm, will be built with the same technology used for the BaBar SVT (double sided silicon strip sensor), that is adequate with the machine background conditions expected at that location in the SuperB accelerator scheme (i.e. with low beam currents).

The SVT angular acceptance, constrained by the interaction region design, will be 300 mrad in both the forward and backward directions, corresponding to a solid angle coverage of 95% in the center-of-mass frame.

3.1.2 Performance Studies

The SuperB interaction region design is characterized by the small size of the transversal section of the beams, at the level of few μm for σ_x , and hundreds of nm for σ_y . Therefore it will be possible to reduce the radial dimension of the beampipe tube, to 1 cm, while preventing the beams to scatter into the beampipe material within the detector coverage angle. The total amount of radial material of the beryllium beampipe, which includes a few μm of gold foil, and a water cooling channel, has been estimated to be less than 0.5% X_0 . For the proposed value for the center of mass boost in SuperB, $\beta\gamma = 0.28$ (7 GeV e^- beam against a 4 GeV e^+ beam), the average B vertex separation along the z coordinate, $\langle\Delta z\rangle \simeq \beta\gamma c\tau_B = 125\mu\text{m}$, is reduced almost by a half with respect to the

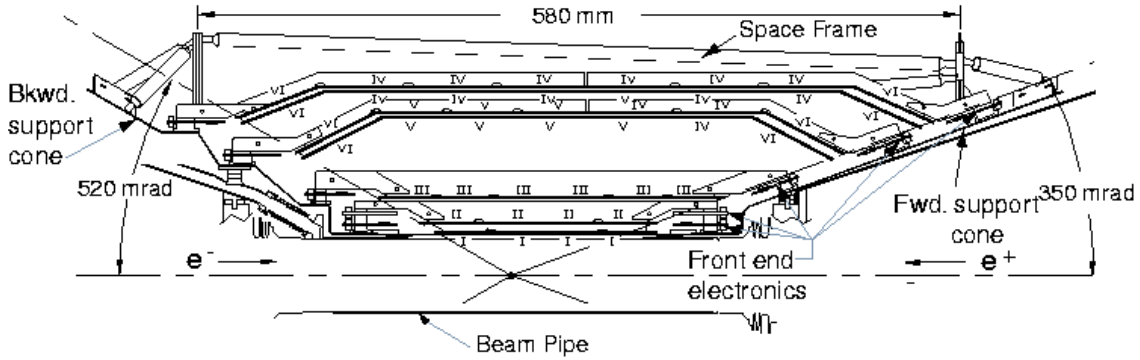


Figure 5: Longitudinal section of the SVT

BABAR experiment, where $\beta\gamma = 0.55$. In order to maintain a suitable resolution on Δt for time-dependent analyses, the proper time difference between the two B decays, it is necessary to improve the vertex resolution (about a factor 2 better) with respect to the current BABAR performances: typically $50 - 80 \mu\text{m}$ in z for exclusively reconstructed modes and $100150 \mu\text{m}$ for inclusively reconstructed modes. The vertex precision requirements for physics, have been achieved in the BABAR experiment, thanks to the performances of the silicon vertex tracker (SVT), a five-layer double-sided silicon detector. The configuration of the SuperB interaction region allows to measure the first hit of the tracks near the production vertex, by adding a vertex detector layer (Layer0) very close to the beampipe and keeping the BABAR SVT layout for the outer layers. This six-layer vertex detector solution would improve significantly the track parameter determination, matching the more demanding requirements on the vertex resolution, while maintaining the stand-alone tracking capabilities for low momentum particles.

The choice among the various options under consideration for the Layer0 (striplets, CMOS MAPS and hybrid pixels) has to take into account the physics requirements for the vertex resolution, depending on the pitch and the total amount of material of the modules. In addition, to assure optimal performance for track

reconstruction, the sensor occupancy has to be maintained under the level of a few percent, imposing further requirements on the sensor segmentation and on the front-end electronics. Radiation hardness should also be taken into account, although it is expected not to be particularly demanding compared to LHC detector specifications.

In order to simulate the resolution on the B decay vertices and on Δt for different Layer0 configurations, we have used the fast simulation program FastSim [?], which reproduces the detector response according to analytical parameterizations. Several studies have been performed where we have reconstructed exclusively one B of the event (B_{reco}) and evaluated the other B (B_{tag}) decay vertex using the charged tracks of the rest of the event after rejecting long-lived particles and tracks not compatible with the candidate vertex. We have considered different B decay modes as B_{reco} , such as $B \rightarrow \pi^+\pi^-$, ϕK_S^0 and also decay modes where the impact of the Layer0 on the decay vertex determination is less effective, such as $B \rightarrow K_S^0 K_S^0$, $K_S^0 \pi^0$. For each decay mode we have studied the resolution on Δt and the per-event error on the physical interesting quantity $\sin(2\beta_{eff})$.

The main result is that the resolution on Δt at SuperB allows a comparable or even better per-event error on $\sin(2\beta_{eff})$ for each B decay mode that we have considered. The conclusion

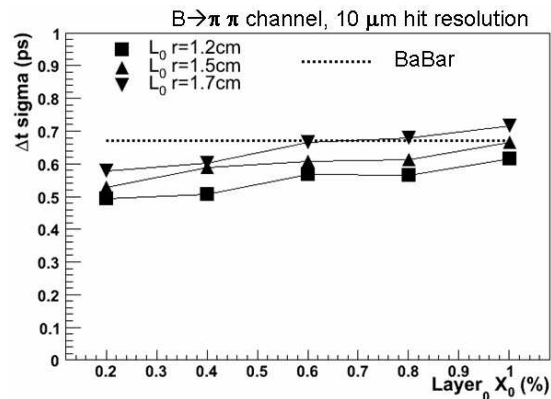


Figure 6: Resolution on the proper time difference of the two B mesons ($\beta\gamma = 0.28$), for different Layer0 radii, as a function of Layer0 thickness (in X_0 %).

is valid for all the technologies that we have considered for Layer0, (i.e., MAPS, triplets, Hybrid Pixels) and for reasonable values of the Layer0 radius and amount of radial material. As an example, in Fig. 6 is reported the resolution on Δt for different Layer0 radii as a function of the Layer0 thickness (in X_0 %) compared to the BaBar reference value. The dashed line represents the BABAR reference value using the nominal value of the boost, $\beta\gamma = 0.55$, according to FastSim.

We have also studied the impact of a possible Layer0 inefficiency on the sensitivity on $\sin(2\beta)$. The source of inefficiency could be related to several causes, for example a much higher background rate than expected causing dead time in the readout of the detector. In Fig. 7 is reported the $\sin(2\beta_{eff})$ per-event error for the $B \rightarrow \phi K_S^0$ decay mode as a function of the Layer0 hit efficiency for the different options (i.e. different material budget). The Layer0 radius in the study is about 1.6 cm. As it is evident from the plot, the triplet solution allows for better performances with respect to the BaBar reference value even in case of small inefficiency, and it has better performances compared to other Layer0 solutions. The main advantage of the

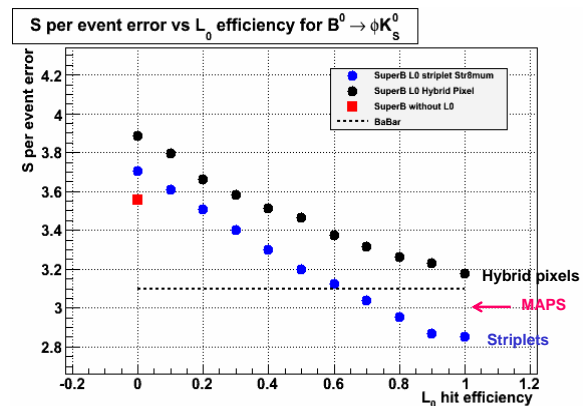


Figure 7: $\sin(2\beta_{eff})$ per event error as a function of the Layer0 efficiency for the different options (i.e. different material budget).

triplet solution is the smaller amount of radial material (about 0.5 % X_0) compared to the Hybrid pixel (about 1% X_0) and the MAPS solutions (about 0.7 % X_0). In fact, for particles of momentum up to few GeV/c the multiple scattering effect is the dominant source of uncertainty in the determination of their trajectory and a low material budget detector reduces this effect. A triplet-based Layer0 solution would have also a better intrinsic hit resolution (about 8 μm) with respect to the MAPS and the Hybrid Pixel (about 14 μm with a digital readout) solutions. For those reasons a Layer0 based on triplets has been chosen as the baseline solution for SuperB, capable to cope with the machine background according to the present estimates.

3.1.3 Background Conditions

Background considerations influence several aspects of the Silicon Vertex Tracker design: readout segmentation, electronics shaping time, data transmission rate and radiation hardness. Severe requirements are especially imposed on the Layer0 design. The different sources of background have been simulated with a detailed Geant4 detector and beamline description to estimate their impact on the experiment [1]. The

background expected in the external layers of the SVT (radius > 3 cm) is dominated by terms that scale with beam currents and is similar to background seen in the present BaBar SVT. The main background at the Layer0 radius is dominated by luminosity terms, in particular by $e^+e^- \rightarrow e^+e^-e^+e^-$ pair production, being radiative Bhabha events an order of magnitude smaller. Despite the huge cross section of the pair production process, the rate of tracks hitting Layer0 is strongly suppressed by the effect of the 1.5 Tesla magnetic field inside the detector. Particles produced, with low transverse momentum, loop in the detector magnetic field and only a small fraction reaches the SVT layers, with a strong radial dependence.

According to these studies the hit rate on the Layer0 at 1.5 cm is at the level of about 20 MHz/cm², mainly due to electrons in the MeV energy range. The equivalent fluence corresponds to $3.7 \times 10^{12} n/cm^2/yr$ and the dose rate to withstand is 3 Mrad/yr. It seems adequate working with a safety factor of five on this background estimate.

3.2 Layer0 options under study

The present status for the development of the various Layer0 options under study for the Technical Design Report preparation is described in this section. The Layer0 technologies proposed have different levels of maturity and expected performance, mainly due to the total material budget associated with the module based on the different technology: triplets modules based on high resistivity sensors with short strips (0.5% X_0), hybrid pixels (1% X_0) and thinner pixel module based on CMOS Monolithic Active Pixel Sensor (MAPS) (0.7% X_0).

R&D programs on more advanced pixel technologies are currently actively pursued, being a thin pixel detector the best solution for Layer0 in an higher background environment (higher luminosity or bad background conditions).

3.2.1 Triplets

Describe the triplets module design as in CDR FSSR2 readout chip

3.2.2 Hybrid Pixels

Hybrid pixels are a mature and viable solution but still requires some R&D to demonstrate that reduction in the front-end pitch and in the total material budget is possible with respect to hybrid pixel systems developed for LHC experiments to meet Layer0 requirements. A front-end chip for hybrid pixel sensor with $50 \times 50 \mu m^2$ pitch and a fast readout is under development. The adopted readout architecture has been previously developed by the SLIM5 Collaboration [3] for CMOS Deep NWell MAPS [4],[5]: the data-push architecture features data sparsification on pixel and timestamp information for the hits. This readout has been recently optimized for the target Layer0 rate of 100 MHz/cm² with promising results: VHDL simulation of a full size matrix (1.3 cm²) gives hit efficiency above 98% operating the matrix with a 60 MHz readout clock. A first prototype chip with 4k pixels has been submitted in September 2009 with the ST Microelectronics 130 nm process. The front-end chip, connected by bump-bonding to an high resistivity pixel sensor matrix, will be then characterized with beams in Autumn 2010.

3.2.3 MAPS

CMOS MAPS are a newer and more challenging technology. Their main advantage with respect to hybrid pixels is that they could be very thin, having the sensor and the readout incorporated in a single CMOS layer, only a few tenth of microns thick. As the readout speed is another relevant aspect for application in the SuperB Layer0 we proposed a new design approach to CMOS MAPS [4] which for the first time made it possible to build a thin pixel matrix featuring a sparsified readout with timestamp information for the hits [5]. In this new design the deep N-well (DNW) of a triple well commercial

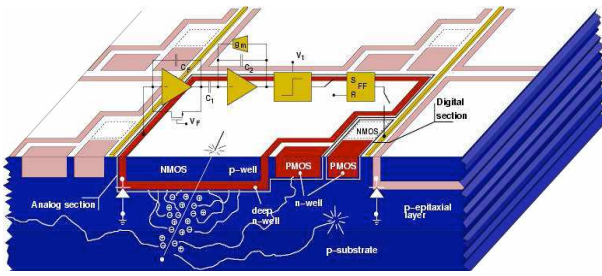


Figure 8: The DNW MAPS concept.

CMOS process is used as charge collecting electrode and is extended to cover a large fraction of the elementary cell (Fig.3.2.3). Use of a large area collecting electrode allows the designer to include also PMOS transistors in the front-end, therefore taking full advantage of the properties of a complementary MOS technology for the design of high performance analog and digital blocks. However, in order to avoid a significant degradation in charge collection efficiency, the area covered by PMOS devices and their N-wells, acting as parasitic collection centers, has to be small with respect to the DNW sensor area. Note that use of a charge preamplifier as the input stage of the channel makes the charge sensitivity independent of the detector capacitance. The full signal processing chain implemented at the pixel level (charge preamplifier, shaper, discriminator and latch) is partly realized in the p-well physically overlapped with the area of the sensitive element, allowing the development a complex in-pixel logic with similar functionalities as in hybrid pixels.

Several prototype chips (the “APSEL” series) have been realized with the STMicroelectronics, 130 nm triple well technology and proved the proposed approach is very promising for the realization of a thin pixel detector. The APSEL4D chip, a 4k pixel matrix with the new DNW cell and the sparsified readout has been characterized during the SLIM5 testbeam showing encouraging results [6]. Hit efficiency of 92% has been measured, a value compatible with the present sensor layout that is designed with a fill

factor (i.e. the ratio of the electrode over the total n-well area) of about 90%. Margins to improve the detection efficiency with a different sensor layout are being currently investigated [7]

Several issues still need to be solved to demonstrate the ability to build a working detector with this technology and require some R&D. Among others the scalability to larger matrix size and the radiation hardness of the technology are under evaluation for the TDR preparation.

Further material reduction and improved performance are also possible with the technology leap offered by vertical integration [8]. A first step in this direction has been the realization of a two-tier DNW MAPS by face to face bonding of two 130 μm CMOS wafer in the Chartered/Tezzaron process. The first submission of vertically integrated DNW MAPS, now in fabrication, includes a 3D version of a 8x32 MAPS matrix with the same sparsified readout implemented in the APSEL4D chip.

3.2.4 Pixel Module Integration

To minimize the detrimental effect of multiple scattering the reduction of the material is crucial for all the components of the pixel module in the active area.

The pixel module support structure needs to include a cooling system to evacuate the power dissipated by the front-end electronics, about $2\text{W}/\text{cm}^2$, present in the active area. The proposed module support will be realized with a light carbon fiber support with integrated microchannels for the coolant fluid (total material budget for support and cooling below 0.3 % X_0). Measurements on first support prototypes realized with this cooling technique indicate that a cooling system based on microchannels can be a viable solution to the thermal and structural problem of Layer0 [9].

The pixel module will also need a light multi-layer bus (Al/kapton based with total material budget of about 0.2 % X_0), with power/signal inputs and high trace density for high data speed to connect the front-end chips in the ac-

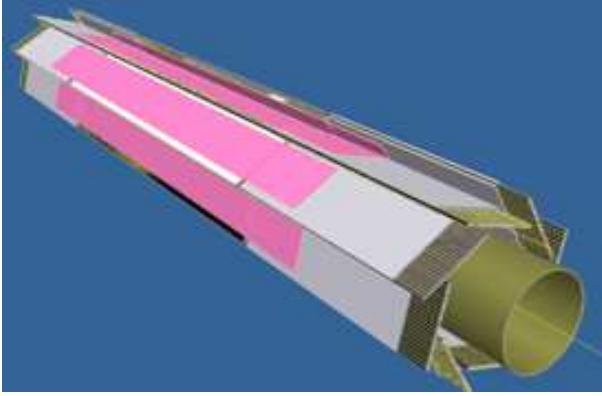


Figure 9: Schematic drawing of the full Layer0 made of 8 pixel modules mounted around the beam pipe with a pinwheel arrangement.

tive area to the HDI hybrid, in the periphery of the module. With the data push architecture presently under study and the high background rate expected data with a 160 MHz clock need to be transferred on this bus. With triggered readout architecture (being also investigated) the complexity of the pixel bus, and material associated, will be reduced.

Considering the various pixel module components (sensor and front-end with 0.4% X_0 , support with cooling, and multilayer bus with decoupling capacitors) the total material in the active area for the Layer0 module design based on hybrid pixel is about 1% X_0 . For a pixel module design based on CMOS MAPS, where the contribution of the sensor and the integrated readout electronics become almost negligible, 0.05% X_0 , the total material budget is about 0.65% X_0 . A schematic drawing of the full Layer0 made of 8 pixel modules mounted around the beam pipe with a pinwheel arrangement is shown in Fig. 3.2.4.

Due to the high background rate at the Layer0 location radiation-hard fast links between the pixel module and the DAQ system located outside the detector should be adopted. For all Layer0 options (that currently share a similar data push architecture) the untrig-

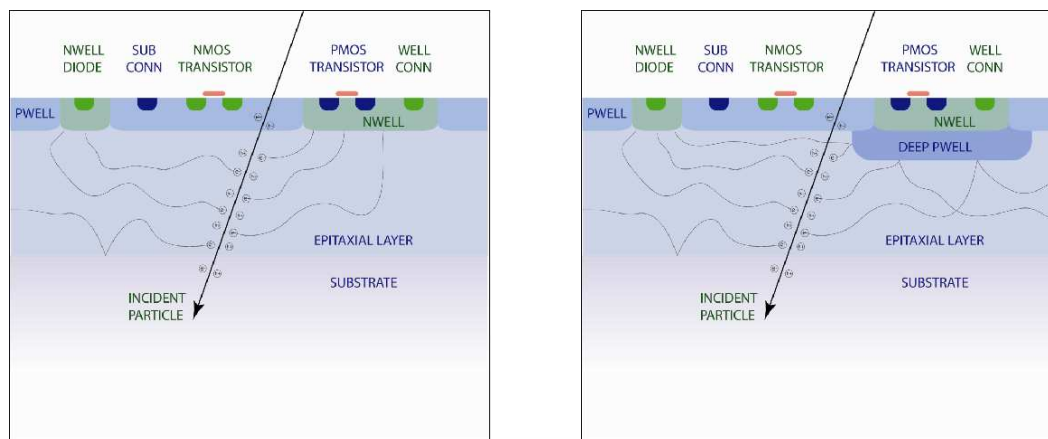
gered data rate is 16 Gbit/s/readout section, assuming a background hit rate of 100Mhz/cm². Triggered data rate is reduced to about 1 Gbit/s/readout section.

The HDI, positioned at the end of the module, outside the active area, will be designed to host several IC components: some glue logic, buffers, fast serializers, drivers. The components should be radiation hard for the application at the Layer0 location (several Mrad/yr).

The baseline option for the link between the Layer0 modules and the DAQ boards is currently based on a mixed solution. A fast copper link is foreseen between the HDI and an intermediate transition board, positioned in an area of moderate radiation levels (several tens of krad/yr). On this transition card the logic with LV1 buffers will store the data until the reception of the LV1 trigger signal and only triggered data will be send to the DAQ boards with an optical link of 1 Gibt/s. The various pixel module interfaces will be characterized in a test set-up for the TDR preparation.

3.3 A MAPS-based all-pixel SVT using a deep P-well process

Another alternative under evaluation is to have a all-pixel SVT using MAPS pixels with a pixel size of 50x50 μm . This approach uses the 180 nm INMAPS process which incorporates a deep P-well. A perceived limitation of standard MAPS is not having full CMOS capability as the additional N-wells from the PMOS transistors parasitically collect charge, thus reducing the charge collected by the readout diode. Avoiding the usage of PMOS transistors however does limit the capability of the readout circuitry significantly. A limited use of PMOS is allowed with the DNW MAPS design (APSEL chips), which anyway accounts for a small degradation in the collection efficiency. Therefore, a special deep P-well layer was developed to overcome the problems mentioned above. The deep P-well protects charge generated in the epitaxial layer from being collected by parasitic N-wells for the PMOS. This then ensures that all charge is being collected by the readout diode and max-



(a) CMOS MAPS without a deep P-well implant

(b) CMOS MAPS with a deep P-well implant

Figure 10: A CMOS MAPS without a deep P-well implant (left) and with a deep P-well implant (right).

imises charge collection efficiency. This is illustrated in Figure 10. This enhancement allows the use of full CMOS circuitry in a MAPS and opens completely new possibilities for in-pixel processing. The TPAC chip [10] for CALICE-UK [11, 12] has been designed using the IN-MAPS process. The basic TPAC pixel has a size of $50 \times 50 \mu\text{m}$ and comprises a preamplifier, a shaper and a comparator [10]. The pixel only stores hit information in a Hit Flag. The pixel is running without a clock and the timing information is provided by the logic querying the Hit Flag. For the SuperB application the pixel design was slightly modified. Instead of just a comparator, a peak-hold latch was added to store the analog information as well. The chip is organised in columns with a common ADC at the end of each column. The ADC is realised as a Wilkinson ADC using a 5 MHz clock rate. The simulated power consumption for each individual pixel is $12 \mu\text{W}$. The column logic constantly queries the pixels, but only digitises the information for the pixels with a "Hit Flag". This allows one to save both space and reduce the power usage and since the speed of the chip is limited by the ADC also increases the readout speed. Both the address of the pixel being hit and its ADC output are stored in a FIFO

at the end of the column. To further increase the readout speed, the ADC uses a pipelined architecture with 4 analog input lines to increase throughput of the ADC. One of the main bottlenecks is getting the data off the chip. It is envisaged to use the Level 1 trigger information to reject most of the events and to reduce the data rate on-chip before moving it off-chip. This will significantly reduce the data rate and therefore also the amount of power and services required .

For the outer layers, the requirements are much more relaxed in terms of occupancy, so in order to reduce the power, it is planned to multiplex the ADC's to let them handle more than one column in the sensor. This is possible due to the much smaller hit rate in the outer layers and the resulting relaxed timing requirements.

An advantage of the MAPS is the elimination of a lot of readout electronics, because everything is integrated in the sensor already which simplifies the assembly significantly. Also since we are using a industry CMOS process, there a significant price advantage compared to standard HEP-style silicon and the additional savings due to the elimination of a dedicated readout ASIC.

In order to evaluate the physics potential of MAPS based all-pixel vertex detector we are currently evaluating the performance of the SuperB detector with different geometries of the SVT, ranging from the SuperB baseline (Layer0 + 5 layers based on strip detectors), through to a 4 or 6 layer all-pixel detector with a realistic material budget for the support structure for all layers.

3.4 R&D Activities

(1 page)

References

- [1] The SuperB Conceptual Design Report, INFN/AE-07/02, SLAC-R-856, LAL 07-15, Available online at: <http://www.pi.infn.it/SuperB>
- [2] FastSim ref, Available online at: <http://www.pi.infn.it/SuperB>
- [3] SLIM5 Collaboration - Silicon detectors with Low Interaction with Material, <http://www.pi.infn.it/slim5/>
- [4] G. Rizzo for the SLIM5 Collaboration., "Development of Deep N-Well MAPS in a 130 nm CMOS Technology and Beam Test Results on a 4k-Pixel Matrix with Digital Sparsified Readout", *2008 IEEE Nuclear Science Symposium, Dresden, Germany, 19-25 October, 2008*
- [5] A. Gabrielli for the SLIM5 Collaboration, "Development of a triple well CMOS MAPS device with in-pixel signal processing and sparsified readout capability" *Nucl. Instrum. Meth. A* **581** (2007) 303.
- [6] M. Villa for the SLIM5 Collaboration, "Beam-Test Results of 4k pixel CMOS MAPS and High Resistivity Striplet Detectors equipped with digital sparsified readout in the Slim5 Low Mass Silicon Demonstrator" *Nucl. Instrum. Meth. A* (2010) doi:10.1016/j.nima.2009.10.035
- [7] E.Paoloni for the VIPIX collaboration, *Beam Test Results of Different Configurations of Deep N-well MAPS Matrices Featuring in Pixel Full Signal Processing*, Proceedings of the XII Conference on Instrumentation, Vienna 2010. To be published in Nucl. Instr. Meth, in Phys. Res. Section A
- [8] R. Yarema, "3D circuit integration for vertex and other detectors", *Proceedings 16th International Workshop on Vertex Detectors (VERTEX2007), Lake Placid (NY, USA), September 23 - 28, 2007, Proceedings of Science PoS(Vertex 2007)017*.
- [9] F.Bosi and M. Massa, "Development and Experimental Characterization of Prototypes for Low Material Budget Support Structure and Cooling of Silicon Pixel Detectors, Based on Microchannel Technology" *Nucl. Instrum. Meth. A* (2010) doi:10.1016/j.nima.2009.10.138
- [10] J. A. Ballin *et al.*, "Monolithic Active Pixel Sensors (MAPS) in a quadruple well technology for nearly 100% fill factor and full CMOS pixels," *Sensors* **8** (2008) 5336.
- [11] N. K. Watson *et al.*, "A MAPS-based readout of an electromagnetic calorimeter for the ILC," *J. Phys. Conf. Ser.* **110** (2008) 092035.
- [12] J. P. Crooks *et al.*, "A monolithic active pixel sensor for a tera-pixel ECAL at the ILC," CERN-2008-008.

4 Drift Chamber

The Super B drift chamber provides the charged particle momentum measurements and measurements of ionization energy loss used for particle identification. This is the only device in Super B to measure velocities of particles having momenta below approximately 700 MeV/c. Its design is based on that of $BABAR$, which has 40 layers of centimetre-sized cells strung approximately parallel to the beam line [1]. A subset of layers are strung at a small stereo angle in order to provide measurements along z , the beam axis.

The drift chamber is required to provide momentum measurements with the same precision as the $BABAR$ drift chamber (approximately 0.4% for tracks with a transverse momentum of 1 GeV/c) and, like $BABAR$ uses a helium-based gas mixture in order to minimize measurement degradation from multiple scattering. The challenge is to achieve comparable or better performance than $BABAR$ but in a high luminosity environment. Both physics and background rates will be significantly higher than in $BABAR$ and as a consequence the system is required to accommodate the 100 fold increase in trigger rate and luminosity-related backgrounds primarily composed of radiative Bhabhas and electron-pair backgrounds from two-photon processes. However, the beam current related backgrounds will only be modestly higher than in $BABAR$. The nature and spatial distributions of these backgrounds dictate the overall geometry of the drift chamber.

The ionization loss measurement is required to be at least as sensitive to particle discrimination as $BABAR$ which has a dE/dx resolution of 7.5%. In $BABAR$, conventional dE/dx drift chamber methods were used in which the total charge deposited on each sense wire was averaged after removing the highest 20% of the measurements as a means of controlling Landau fluctuations. In addition to this conventional approach, the Super B drift chamber group is exploring a *cluster counting* option which, in prin-

ciple, can improve the dE/dx resolution by approximately a factor of two. This technique involves counting individual clusters of electrons released in the gas ionization process. In so doing, we remove the sensitivity of the specific energy loss measurement to fluctuations in the numbers of electrons produced in each cluster, fluctuations which significantly limit the intrinsic resolution of conventional dE/dx measurements. As no experiment has employed *cluster counting*, this is very much a detector research and development project but one which potentially yields significant physics payoff at Super B .

4.1 System Design

4.1.1 Backgrounds

The dominant source of background in the Super B DCH is expected to be radiative Bhabha scattering. Photons radiated collinearly to the initial e^- or e^+ direction can bring the beams off-orbit and ultimately produce showers on the machine optic elements. This process can happen meters away from the interaction point and the hits are in general uniformly distributed over the drift chamber volume. “Real” $e^+e^- \rightarrow e^+e^-(\gamma)$ scattering has the well-known $1/\theta^4$ cross section; simulation studies are presently underway to evaluate the need to design tapered endcaps (either conical or a with stepped shape) at small radii to keep under control the occupancy in the very forward region of the detector. The actual occupancy and its geometrical distribution in the detector depend on the details of the machine elements, on the amount and placement of shields, and on the drift chamber geometry. Preliminary results obtained with GEANT4 simulations indicate that at nominal luminosity ($10^{36} \text{ cm}^{-2} \text{ s}^{-1}$) and background conditions the average occupancy is of $\mathcal{O}(1 \div 2\%)$. Intense work is presently underway to validate these results and study their dependence on relevant parameters.

4.2 Mechanical Structure

The Drift Chamber mechanical structure must sustain the wire load – about 3 tons for 10 000 cells – with small deformations, while at the same time offer minimum material to the surrounding detectors. Carbon Fiber-resin composites have high elastic modulus and low density, thus offering performances superior to Aluminum-alloys based structures. Endplates with curved geometry can further reduce material thickness respect to flat endplates for a given deformation under load. For example, the KLOE Drift Chamber [2] features 8 mm thick Carbon Fiber spherical endplates of 4 m diameter. Preliminary design of Carbon Fiber endplates for SuperB indicate that adequate stiffness ($\simeq \mathcal{O}(1\text{mm})$ maximum deformation) can be obtained with 5 mm thick spherical endplates, corresponding to $0.02X_0$ (compare $0.13X_0$ for the BABAR Aluminum DCH endplates).

Figure 11 shows two possible endcap layouts, respectively with spherical (a) or stepped (b) endplates. We are also considering a convex spherical endplate, which provides a better match to the geometry of the forward PID and calorimeter, and would reduce the impact of the endplate material on the performance of these detectors, at the cost of greater sensitivity to the wide-angle Bhabha background.

4.3 Drift Chamber Geometry

The SuperB drift chamber will have a cylindrical geometry. The dimensions have been re-optimized through detailed simulation studies respect to BABAR since: *a)* in SuperB there will be no *support tube*; *b)* the possibility is being considered to add a PID device between the drift chamber and the forward calorimeter, and an EMC in the backward direction.

Simulation studies performed on several signal samples with both high (*e.g.* $B \rightarrow \pi^+\pi^-$), and medium-low (*e.g.* $B \rightarrow D^*K$) momentum tracks indicate that: *a)* due to the increased lever arm, momentum resolution improves as the minimum drift chamber radius R_{min} de-

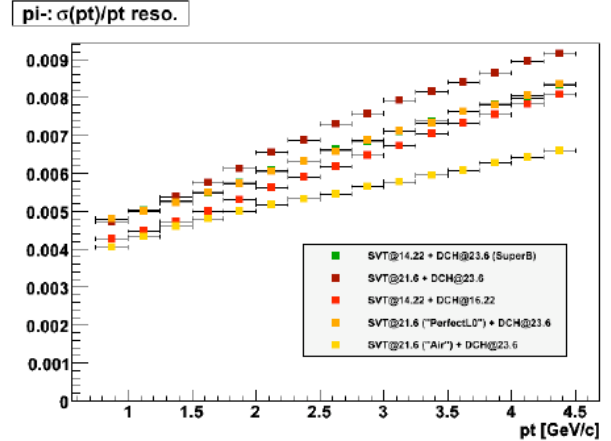


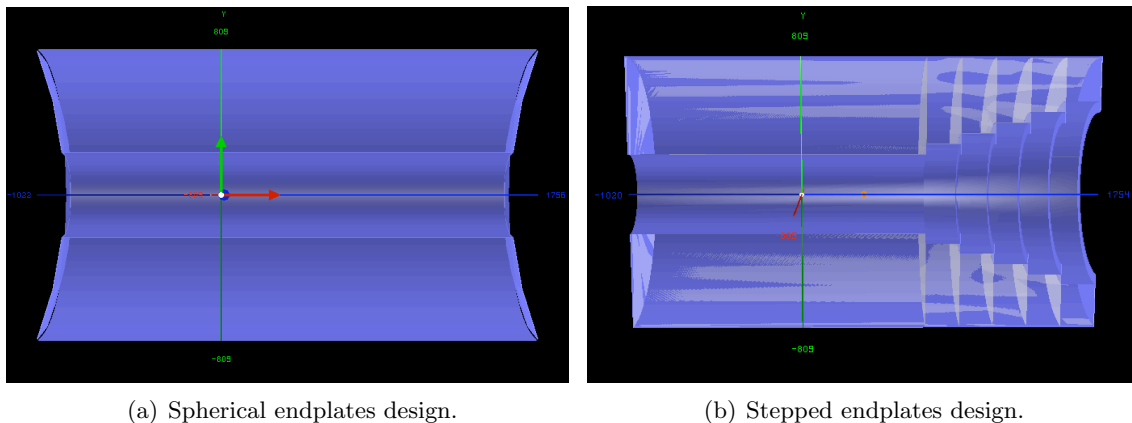
Figure 12: Track momentum resolution for different values of the drift chamber inner radius.

creases, see Fig. 12; R_{min} is actually limited by mechanical integration constraints with the cooling system and the SVT. *b)* The momentum and especially the dE/dx resolution for tracks going in the forward or backward directions are clearly affected by the change in number of measuring samples when the chamber length is varied of 10 – 30 cm. However the fraction of such tracks is so small that the overall effect is negligible.

The Drift Chamber outer radius is constrained to 809 mm by the DIRC quartz bars. As discussed before, the Drift Chamber inner radius will be as small as possible; since final designs of the cooling system are not available yet, in Fig. 11 the nominal BABAR Drift Chamber inner radius of 236 mm has been used. The maximum DCH length is 2764 mm; as the rest of the detector, the Drift Chamber is shifted by 367 mm with respect to the interaction point.

4.4 Gas Mixture

The gas mixture for SuperB should satisfy the requirements which already concurred to the definition of the BABAR drift chamber gas mixture (80%He – 20% iC_4H_{10}), *i.e.* low density, small diffusion coefficient and Lorentz angle, low sensitivity to photons with $E \sim 10$ keV. To

Figure 11: Possible Super B dch layouts.

match the more stringent requirements on occupancy rates of Super B , it could be useful to select a gas mixture with a larger drift velocity in order to reduce ion collection times and so the probability of hits overlapping from unrelated events. The *cluster counting* option would instead call for a gas with low drift velocity and primary ionization.

4.5 Cell Design and Layout

The baseline design for the drift chamber employs small rectangular cells arranged in 40 (place holder) concentric layers about the axis of the chamber which is approximately aligned with the beam direction. Each cell is approximately 15mm by 20 mm (place holders) along the radial and azimuthal direction, respectively. The cells are grouped radially into ten superlayers, each of which is four cells deep. The inner and outer superlayers are parallel to the chamber axis (axial) whereas the remaining eight superlayers are oriented at a small “stereo” angle (XX°) relative to the axis in order to provide the z -coordinates of the track hits. These eight stereo superlayers alternate in the sign of the stereo angle.

Each cell has one $20\mu\text{m}$ diameter gold coated sense wire surrounded by a rectangular grid of eight field wires. The sense wires vary in length from XX cm at the inner radius to YY cm at the

outer radius. They are strung under 50 g weight tension which keeps the gravitational sag of the wires at mid-length to less than $XX \mu\text{m}$. The baseline calls for a gas gain of approximately 5×10^4 which requires a voltage of approximately +2 kV to be applied to the sense wires with the field wires held at ground.

The field wires are aluminum with a diameter of $XX\mu\text{m}$, a value chosen to keep the electric field on the wire surface below 20 kV/cm as a means of suppressing the Malter effect. These wires are tensioned with XX g weights in order to provide a gravitational sag that matches that of the sense wires. The tension is no more than half the tensile strength of the wire.

At a radius inside the inner most superlayer the chamber has an additional layer of axially strung guard wires which serve to electrostatically contain very low momentum electrons produced from background particles showering in the DCH inner cylinder and SVT.

4.6 R&D work

Various R&D programs are underway towards the definition of an optimal drift chamber for Super B , in particular: make precision measurements of fundamental parameters (drift velocity, diffusion coefficient, Lorentz angle) of potentially useful gas mixtures; study with small drift chamber prototypes and simulations the

properties of different gas mixtures and cell layouts; verify the potential and feasibility of the *cluster counting* option.

A precision tracker made of 3 cm diameter Aluminum tubes operating in limited streamer mode with a single tube spatial resolution of around $100\ \mu\text{m}$ has been setup. A small prototype with a cell structure resembling the one used in the *BABAR* DCH has been also built and commissioned. Tracker and prototype have been collecting cosmic ray data since October 2009. Tracks can be extrapolated in the DCH prototype with a precision of $80\ \mu\text{m}$ or better. Different gas mixtures have been tried in the prototype: starting with the original *BABAR* mixture ($80\%He - 20\%iC_4H_{10}$) used as a calibration point, both different quencher proportions and different quenchers (e.g methane) have been tested in order to explore the phase space leading to lighter and possibly faster operating gas. Fig. 13a shows the space-time correlation for one prototype cell: as mentioned before, the cell structure is such as to mimic the overall structure of the *BABAR* DCH. Preliminary analysis shows that the spatial resolution are consistent with what has been obtained with the original *BABAR* DCH. A space to time relation is depicted in Fig. 13b with a $52\%He - 48\%iCH_4$ gas mixture. This gas is roughly a factor two faster and 50% lighter than the original *BABAR* mix: preliminary analysis shows space resolution performances comparable to the original mix, however detailed studies of the Lorentz angle have to be carried out in order to consider this mixture as a viable alternative.

To improve performances of the gas tracker a possible road could be the use of the *Cluster Counting* method. If the individual ionization cluster can be detected with high efficiency, it could in principle be possible to measure the track specific ionization by counting the clusters themselves, therefore with a resolution twice as better than the traditional truncated mean method. Having many independent time measurements in a single cell, the spatial accuracy could also in principle be improved substantially. These promises of exceptional energy

and spatial resolution must however fit with the available data transfer bandwidth, require a gas mixture with well-separated clusters and high detection efficiency. The preamplifier risetime and noise are also issues.

Comparisons of the traditional methods to extract spatial position and energy losses and the *cluster counting* method are being setup at the moment of writing the present report.

References

- [1] The *BABAR* Collaboration, *The BABAR Detector*, Nucl. Instr. Meth, in Phys Res. **A479** (2002) 1.
- [2] M.Adinolfi et al., The KLOE Collaboration, *The tracking detector of the KLOE experiment*, Nucl. Instr. Meth, in Phys Res. **b A488** (2002) 51.

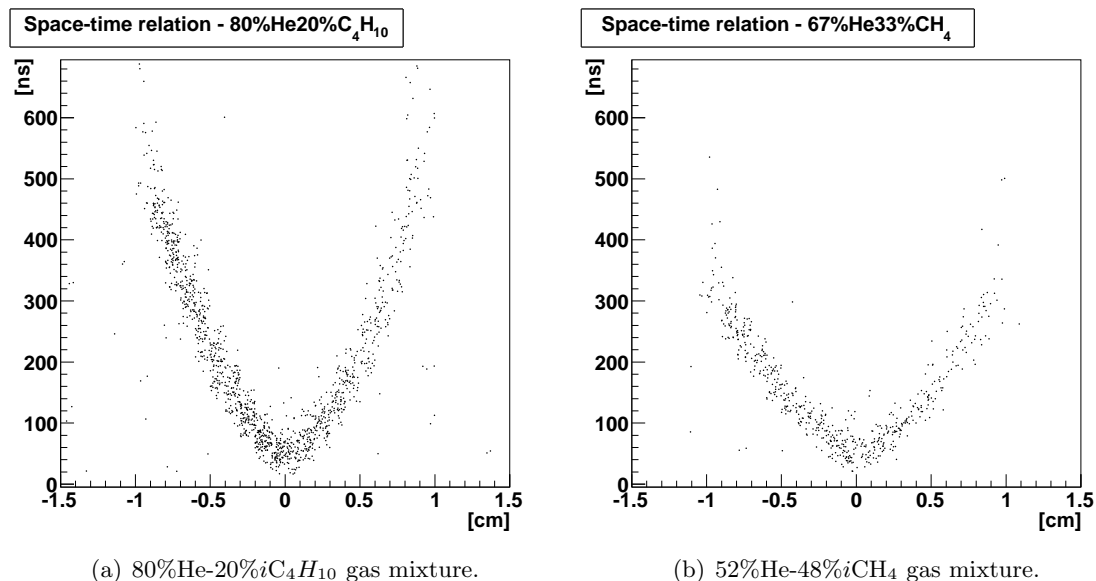


Figure 13: *Examples of measured space-time relation in different He-based gas mixtures.*

5 Particle Identification

5.1 Detector concept

The DIRC (Detector of Internally Reflected Cherenkov light) [1] is an example of innovative detector technology that has been crucial to the performance of the *BABAR* first-class science program. Excellent flavor tagging will continue to be essential for the program of physics anticipated at *SuperB*, and the gold standard of particle identification in this energy region is agreed to be that provided by internally reflecting ring-imaging devices (the DIRC class of ring imaging detectors). The challenge for *SuperB* is to retain (or even improve) the outstanding performance attained by the *BABAR* DIRC [2], while also gaining an essential factor of 100 in background rejection to deal with the much higher luminosity.

We are planning to build a new Cherenkov ring imaging detector for the *SuperB* barrel, called the Focusing DIRC, or FDIRC. It will use the existing *BABAR* bar boxes and mechanical support structure. We will attach to this

structure a new photon camera, which will be optically coupled to the bar box window. The new camera design combines a small modular focusing structure that images the photons onto a focal plane instrumented with very fast, highly pixilated, photon detectors (PMTs). These elements should combine to attain the desired performance levels while being at least 100 times less sensitive to backgrounds than the *BABAR* DIRC.

We are also considering several options for a possible PID detector in the forward direction. The design variables in our consideration are: (a) modest cost, (b) small mass in front of the LYSO calorimeter, (c) removal of a dE/dx ambiguity in π/K separation near 1 GeV/ c , and (d) enlarge the total PID coverage at low momenta. Presently, we are considering the following technologies: (a) DIRC-like time-of-flight [3], (b) pixilated TOF [4] and (c) Aerogel RICH [5]. The aim is to design the best possible *SuperB* detector by optimizing physics, performance and the cost, while being constrained to the existing *BABAR* geometry.

5.1.1 Charged particle identification at SuperB

The charged particle identification at SuperB relies on the same framework as the BABAR experiment. Electrons and muons are identified by the EMC and the IFR respectively, while energy losses (dE/dx) in the inner trackers (SVT and DCH) are used to distinguish low-momentum hadrons. At higher momenta (above $0.7 \text{ GeV}/c$ for pions and hadrons, above $1.3 \text{ GeV}/c$ for protons), a dedicated system, the FDIRC – inspired by the successful BABAR DIRC – will perform the π/K separation. One needs to cope with $100\times$ larger luminosity and possibly a higher background compared to BABAR. To achieve this goal, the PMTs will be highly pixilated, about 10 times faster and the total camera size will be about 25 times smaller compared to the BABAR DIRC. This new detector, described in Section 5.2, is expected to perform well over the entire momentum range for B -physics. But its geometrical coverage is limited to the barrel which is why there is an ongoing R&D effort to design a forward PID detector.

5.1.2 BABAR DIRC

The BABAR DIRC is a novel ring-imaging Cherenkov detector. The Cherenkov light is produced in ultra-pure synthetic fused silica bars and its image is preserved while propagating along the bar via internal reflections to the detector.

The entire DIRC has 144 quart bars, each 4.9 m-long, which are set along the beam line and cover the whole azimuthal range. They are used to produce Cherenkov light when charged particles cross them. Thanks to an internal reflection coefficient of ~ 0.9997 , these photons are transported to the back end of the bars with the magnitude of their angles conserved. They exit in a large volume of purified water (a medium chosen because its average index of refraction and its chromaticity index are very close to those of the fused silica), the standoff box (SOB). The PMTs are located at the rear of the SOB, about 1.2 m away from the quartz bar

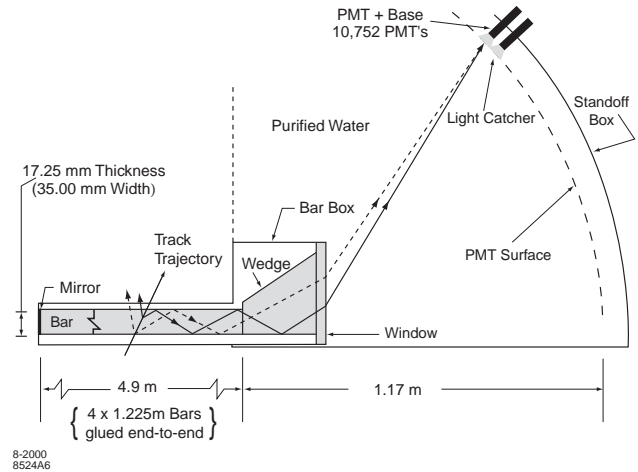


Figure 14: Schematic of the BABAR DIRC.

exit window. The DIRC is not only using the position of the photon hits but also their time of arrival to separate signal from background and to reconstruct the Cherenkov angles.

The reconstruction of the Cherenkov angles uses information from the tracking system in addition to the position of the PMT hits in the DIRC while the hit timing helps reducing the background. The outputs of this phase are twofold: first, a measurement of the Cherenkov angle track by track; second, a global analysis of the whole event based on an un-binned maximum likelihood formalism. Both types of results are then used in the PID selectors which identify the types of the charged particles crossing the BABAR detector.

The DIRC has been reliably and efficiently working over the whole BABAR data taking period (1999-2007). Detector physics performance remained the same, although some upgrades, such as addition of shielding and replacement of electronics, were necessary. Its main performance parameters are the following:

- measured time resolution of about 1.7 ns, close to the PMT transit time spread of 1.5 ns;
- single photon Cherenkov angle resolution of 9.6 mrad for dimuon events;

- Cherenkov angle resolution of 2.5 mrad in dimuon events;
- $K - \pi$ separation above 2.5 ' σ ' from the pion Cherenkov threshold up to 4.2 GeV/c.

5.2 Barrel PID at SuperB

5.2.1 Performance optimization

The *BABAR* DIRC [1, 2] is an innovative internally reflecting Ring Imaging Cherenkov Counter. It uses quartz bar radiators of Cherenkov light and the pinhole focusing technique onto an imaging device made up of individual conventional PMTs. Its success in *BABAR* motivated us to propose this concept again for the SuperB application. However, much larger rates and possibly larger background required modifications of its photon camera, the SOB. *BABAR* DIRC camera uses 1800 gallons of water as optical coupling medium in the region between the fused silica bars and the photon detectors. This makes this detector more sensitive to the photon and neutron backgrounds. We plan to replace the *BABAR* SOB with a focusing optics (FBLOCK), which would be machined out from radiation-hard solid pieces of fused silica. The major design constraints for the new camera are the following: (a) it has to be consistent with the existing *BABAR* bar box design as these elements will be reused in SuperB; (b) it has to coexist with the *BABAR* magnet mechanical constraints; (c) it requires a very fine photon detector pixelization.

The imaging is provided by a mirror structure focused onto an image plane containing highly pixilated photomultiplier tubes. The reduced volume of the new camera and the use of different material already reduce the sensitivity to background by about one order of magnitude compared to *BABAR* DIRC. The very fast timing of the new tubes will provide many additional advantages: (a) an improvement of the Cherenkov resolution; (b) a measure of the chromatic dispersion term in the radiator [6, 7, 8]; (c) the separation of ambiguous solutions in the folded optical system; and (d), another order

of magnitude improvement in background rejection.

Fig. 15 shows the new FDIRC camera design (see Ref. [9] for more detail). It consists of two parts: (a) the focusing block (FBLOCK), and (b) a new wedge. The new wedge rotates all rays onto the FBLOCK cylindrical mirror. It was necessary to add it as the old *BABAR* DIRC wedge is not long enough for the new optics to work properly: not all rays would strike the cylindrical mirror. This mirror is rotated appropriately to make sure that all rays reflect onto the FBLOCK flat mirror and that none of them goes back into the bar box itself; the flat mirror reflects them then onto the detector focal plane with an incidence angle of almost 90° , which avoids reflections. The focal plane is located in a slightly under-focused position to reduce the FBLOCK size and therefore its weight: there is no need to be exactly in focus as the pixel size would not take advantage of it. The total weight of the solid Fused silica FBLOCK is about 80 kg. This significant weight requires a good mechanical support.

There are several important advantages to moving from the *BABAR* pinhole focused design to a focused optical design made of solid Fused Silica: (a) the design is modular; (b) sensitivity to background, especially to neutrons, is significantly reduced; (c) the pinhole-size component of the angular resolution in the focusing plane can be removed and timing can be used to measure the chromatic dispersion, improving performance; (d) the total number of multi-anode photomultipliers (MaPMT) is reduced by about one half compared to a non-focusing design with equivalent performance; (e) there is no risk of water leaks into the SuperB detector, and no time-consuming maintenance of a water system, as required to operate *BABAR* safely.

The new camera will be attached to the *BABAR* bar box with an optical RTV glue, which will be injected in a liquid form between the bar box window and the new camera and will cure in this state. As Fig. 15 shows, focusing is in the radial (y) direction with a cylindrical mirror, while pinhole focusing is used in the di-

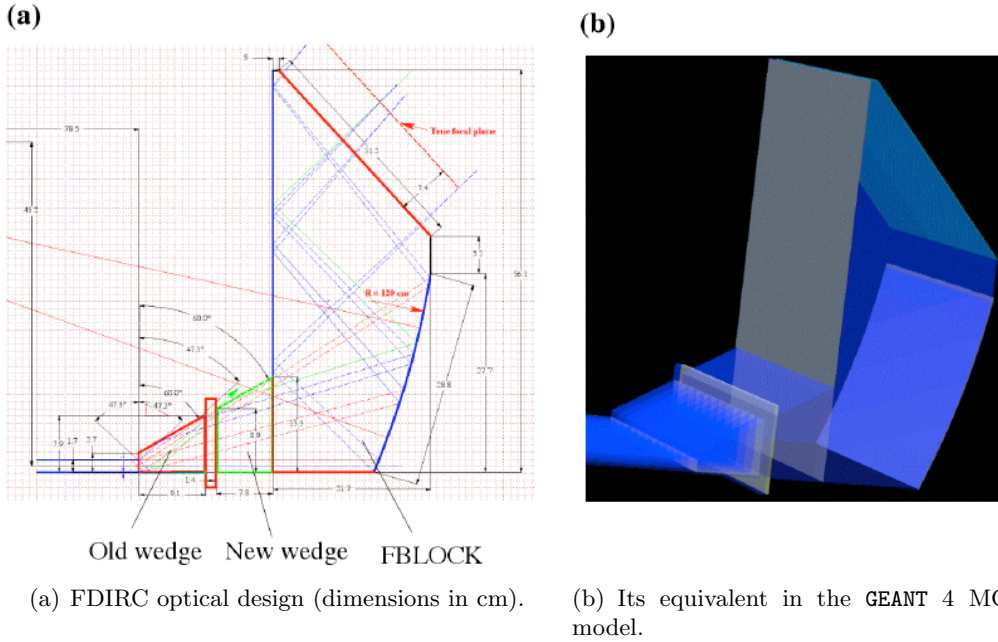


Figure 15: Barrel FDIRC Design.

rection out of the plane of the schematic (the x-direction). Photons that enter the FBLOCK at large x-angles reflect from the parallel sides, leading to an additional ambiguity. However, the folded design makes the optical piece small, and places the photon detectors in an accessible location, improving both the mechanics and the background sensitivity. Since the optical mapping is 1 to 1 in the y-direction, this reflection does not create an additional ambiguity. Since a given photon bounces inside the FBLOCK only 1-3 times, the requirements on surface quality and polishing for the optical piece are much less stringent than what was required for the DIRC bar box radiator bars. This reduces the cost significantly.

The internal DIRC wedge has a 6 mrad angle at the bottom. This was done intentionally for *BABAR* to do a simple focusing in the pin-hole optics to reduce the effect of a bar thickness. However, this angle somewhat worsens the new FDIRC optics resolution. We have two choices: (a) either leave it as it is, or (b) glue a micro-wedge. Adding the micro-wedge at the bottom of the old wedge is possible in principle,

although it is not a trivial operation, as one has to open the bar box.

The performance of the new FDIRC is simulated with a GEANT 4 MC program [10]. The preliminary results for the expected Cherenkov angle resolution are shown in Table 1 for different layouts [10]. Design #1, which is our preference (a 3 mm × 12 mm pixel size with the micro-wedge glued in) gives a resolution of ~ 8.1 mrad for 4 GeV/c pions at $\theta_{dip} = 90^\circ$. This can be compared with *BABAR* DIRC measured resolution of ~ 9.6 mrad for di-muon events. If we decide not to glue in the micro-wedge (design #2), the resolution will increase to 8.8 mrad, i.e., we lose about 0.7 mrad. Going to a coarser pixelization of 6 mm × 12 mm will worsen the Cherenkov angle resolution by about ~ 1 mrad (see designs #3 & #4). If one adds the chromatic correction to the Cherenkov angle using the timing information on each photon [6, 9, 11] the FDIRC resolution may improve by an additional 0.5-1 mrad.

FDIRC Design	Option	θ_C resolution [mrad]
1	3 mm \times 12 mm pixels with a micro-wedge	8.1
2	3 mm \times 12 mm pixels and no micro-wedge	8.8
3	6 mm \times 12 mm pixels with a micro-wedge	9.0
4	6 mm \times 12 mm pixels and no micro-wedge	9.6

Table 1: FDIRC performance simulation by GEANT 4 MC.

5.2.2 Design and R&D status

We plan to use MaPMTs as photon detectors. They are highly pixilated and about 10 times faster than the *BABAR* DIRC PMTs. Their design proved itself in high rate environments such as the HERA-B experiment. There are two options for the pixilization: (a) a pixel size of 3 mm \times 12 mm is achieved by shorting pads of the Hamamatsu 256-pixel H-9500 MaPMT, resulting in 64 readout channels per MaPMT. Fig. 16(a) [11] shows a relative single photoelectron response of this tube with such pixilization, normalized to the Photonis Quantacon PMT. Each camera will have ~ 48 H-9500 MaPMT detectors, which corresponds to a total of ~ 576 for the entire SuperB FDIRC, or ~ 36864 pixels in the entire system. This is about half of what is required for a non-focusing DIRC. (b) Another option – see Fig. 16(b) – is a pixel size of 6 mm \times 12 mm, which is achieved by shorting pads of the Hamamatsu 64-pixel H-8500 MaPMT, resulting in $64/2 = 32$ readout channels per MaPMT, i.e. half of the total pixel count compared to the H-9500 choice. To get

the best Cherenkov angle resolution, we prefer to use the pixel size of 3 mm in the vertical direction and 12 mm in the horizontal direction. This configuration, combined with a good single photon timing resolution, is expected to provide superior Cherenkov angle resolution using the full three-dimensional imaging available with the DIRC technique. This improved level of performance has been shown [6, 7, 8], including the first demonstration of the single photon chromatic dispersion correction in a smaller FDIRC prototype, albeit also in a somewhat different optical arrangement. Although we would prefer to use the smaller pixels of H-9500 MaPMT, a potential advantage of the H-8500 MaPMT solution would be a higher quantum efficiency (QE), and its wider use in the medical community yielding Hamamatsu emphasis on this tube. Hamamatsu could deliver reliably H-8500 tubes with QE $\sim 24\%$, which cannot be promised for the H-9500 tube at this point. Furthermore, the H-9500 delivery can extend up to 3.5 years, according to Hamamatsu itself. The final choice between the two MaPMTs will be made during the R&D period.

We are considering several choices for the FDIRC electronics. One option is to use a leading edge discriminator with a 100 ps/count TDC, together with an additional ADC to do a pulse height correction in order to obtain a good timing resolution at a level of 150-200 ps per single photon. An alternative is to use a waveform digitizing electronics, either based on the Waveform catcher concept [12] or the BLAB chip design [13]. These choices will be made during the R&D period.

Fig. 17 shows a possible design for the mechanical support. Each bar box has its own FBLOCK support, light sealing and individual access for maintenance. Each FBLOCK, weighing almost 100 kg, is supported on rods with ball bearings to be able to bring it very precisely to the bar box. The optical coupling between the FBLOCK and the bar box is done with a RTC coupling. Similarly, detectors are coupled to FBLOCK with a RTV cookie. There is a common magnetic shield mounted on hinges, which

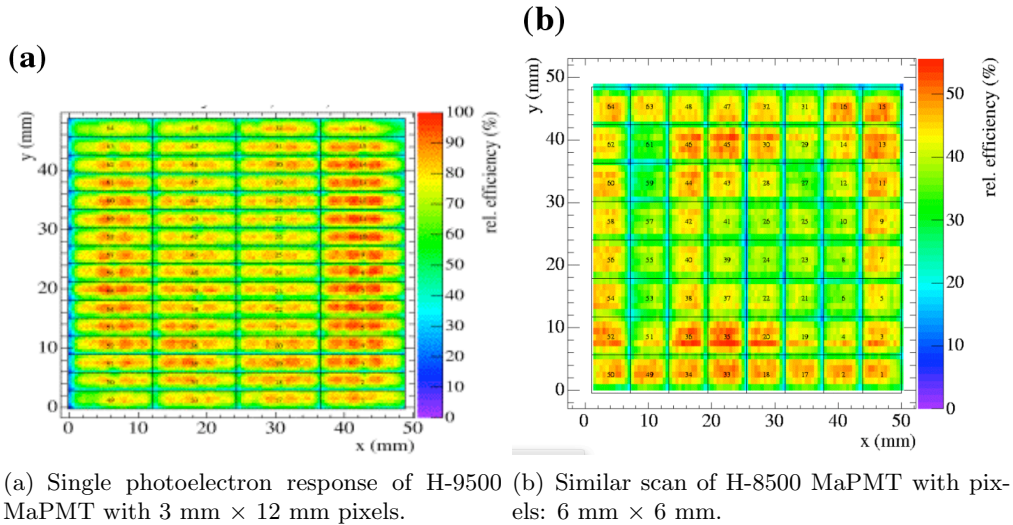


Figure 16: Single photoelectron response of MaPMTs.

would allow an easy access. This is possible as the entire volume of the new focusing optics is about 10 times smaller than the *BABAR* SOB.

We will test various electronics choices in the SLAC cosmic ray telescope (CRT) [14] with the FDIRC single bar prototype. We plan to replace it with a full size DIRC bar box equipped with the new focusing optics, and run it in the CRT sometimes between 2010-11. In parallel, we plan to revive the scanning setup to test photodetectors with the new electronics. Test bench setups are also planned at LAL-Orsay and in the University of Maryland.

Finally, a summary budget projecting the costs of the barrel FDIRC can be found in Section 11.

5.3 Forward PID at SuperB

5.3.1 Motivation for a forward PID detector

Outside of the barrel where the FDIRC detector will ensure a good $\pi - K$ separation up to about 4 GeV/c, hadron identification would only rely on dE/dx measurements from the DCH in a *BABAR*-like design. The performances of such device are limited above 700 MeV/c due to the π/K ambiguity near 1 GeV/c and relatively poor PID performance between 1 and 2 GeV/c.

This explains why various *BABAR* physics analyses would have benefited from additional dedicated PID systems on both ends of the detector. Gains in hermiticity and in PID performances provide higher efficiency in various exclusive B -channels and help killing specific backgrounds. In addition, the hadronic and semi-leptonic B reconstructions – a key ingredient of recoil physics analyzes – would be improved as well. For some of these channels, the reconstruction efficiency and the purity go up significantly: the higher the number of charged particles in the reconstructed final states, the faster the gain. Dedicated Monte-Carlo studies aiming at quantifying these improvements are ongoing within the SuperB Detector Geometry Working Group (DGWG).

For the backward side of SuperB, the EMC group is proposing a backward calorimeter which looks promising. Even if the energy resolution is not good enough to reconstruct π^0 's, detecting activity in this device helps reducing $B \rightarrow \tau\nu$ background for instance. Moreover, as the momenta of backward-going particles are quite low in average, a moderate timing resolution (around 100 ps) would make this device useful for a time-of-flight-based separation of hadrons.

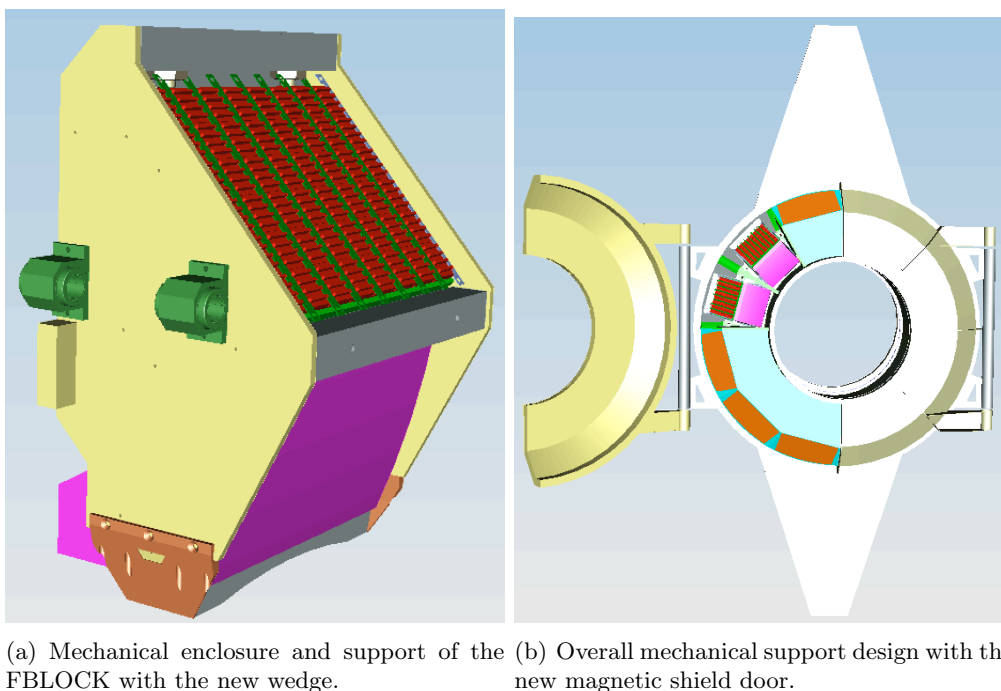


Figure 17: Possible mechanical design for the FDIRC.

The forward region is covering a larger fraction of the SuperB geometrical acceptance than the backward one because of the boost, although it is still less than 10% of the total. Another consequence of the beam energy asymmetry is that the particles crossing this region have higher momenta in average. Space is also limited in this area which is located at the interface between the DCH and the EMC endcap. All these constraints make more challenging the design of a suitable PID detector covering this polar angle range. Yet, the SuperB PID group is investigating this option in details with the help of the DGWG. The status of this ongoing R&D effort is reported in Section 5.3.3.

5.3.2 Forward PID requirements

A SuperB forward PID detector should be thin to fit well in the space between the DCH endplate and the EMC endcap: at most a thickness of ~ 10 cm. If it were bigger, the geometry and position of the nearby detectors would have to be modified: either a shorter DCH or a for-

ward shift of the EMC crystals. Moreover, the X_0 of this new device should be kept as low as possible, in order to avoid degrading the reconstruction of electromagnetic showers in the EMC endcap. Finally, the cost of such detector must be small with respect to the cost of the barrel PID, probably in proportionality to its solid angle fraction.

5.3.3 Status of the forward PID R&D effort

Three designs of forward PID detector are currently investigated: a 'DIRC-like' time-of-flight device, a 'pixilated' time-of-flight detector and a Focusing Aerogel RICH, the 'FARICH'.

'DIRC-like' time-of-flight detector concept

In this scheme [3], charged tracks cross a thin layer of quartz in which Cherenkov photons are emitted along the particle trajectories. These photons are then transported through internal reflections to one side of the quartz volume where they are detected by PMTs located outside of the SuperB acceptance. The PID separa-

ration is provided by the timing of the photons: at given momentum, kaons fly more slowly than pions as they are heavier. This method is challenging as the whole detector chain (the hardware and the reconstruction software) must be very accurate: for instance, 3 GeV/c kaon and pion are only separated by about 90 ps after 2 meters – roughly the expected particle flight distance using the current SuperB layout. On the other hand, such detector should fit without problem in the available space between the DCH and EMC and its X_0 is the smallest of all the studied layouts.

'Pixilated' time-of-flight detector concept

Like for the previous design, the Cherenkov light is produced in a quartz radiator [4]. However, in this case it is made of Al-coated cubes, which are matching pixilated photodetectors coupled to them. This layout makes the reconstruction much easier (a given track would only produce light in a particular pixel whose location would be predicted by the tracking algorithms), it is insensitive to chromatic time broadening, and it is less sensitive to background. On the other hand, the radiation length X_0 is larger as the photodetectors are located in front of the EMC calorimeter. In addition, as PMTs with excellent timing resolution (such as MCP-PMTs) and able to operate at 16 kG are very expensive, the total cost of this detector would exceed the DIRC-like solution by a significant factor.

However, we are presently investigating another possible iteration to this scheme: can one use the LYSO crystal fast light component to do a decent TOF measurement of about ~ 100 ps? This would be sufficient to resolve the π/K ambiguity near 1 GeV/c (where dE/dx is useless) and help PID below 700 MeV/c.

FARICH concept The FARICH detector [5] uses a 3-layer aerogel radiator with focusing effect and a water radiator. The Cherenkov light is detected by a wall of pixilated MCP-PMTs. MC simulations predict a π/K separation at the 3 ' σ ' level and better up to 5 GeV/c and a μ/π separation up to 1 GeV/c. The amount

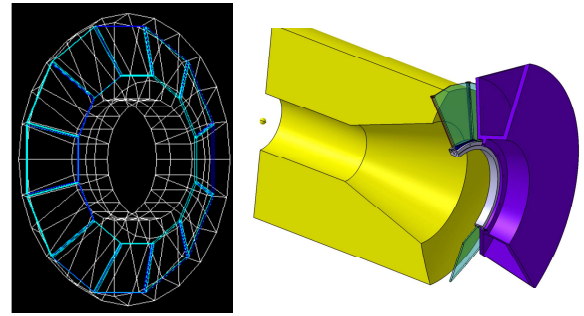


Figure 18: Left: the 'DIRC-like' TOF design, as currently implemented in GEANT 4 simulations. Right: a possible design for the mechanical integration of this detector (in green) in SuperB. The yellow (magenta) volumes represent the envelope of the DCH (forward EMC).

of material is about the same as in the 'pixilated' time-of-flight design while the number of channels is 4 times larger. The FARICH has the best PID performance of all detectors proposed for the forward direction. Its main drawbacks are thickness, cost and absence of beam test results.

Summary of 'DIRC-like' time-of-flight studies

Fig 18 shows the current layout of the 'DIRC-like' time-of-flight (TOF) detector, as implemented in GEANT 4-based simulations. Twelve tiles (1-2 cm thick) of fused silica provide a good azimuthal coverage of the forward side of the SuperB detector. The photons are transported inside the fused silica volume until the inner part of the tile where they are detected by MCP-PMTs. Simulations are in progress to understand and optimize the detector response to signal Cherenkov photons. The main topics addressed by these studies are the following.

- The pitch angle of the tiles with respect to the endcap calorimeter. With a null angle, photons from the tracks hitting the out-

ermost part of the tiles will not be transported by internal reflection to the PMTs. Moreover, the larger this angle, the lower the momentum threshold from which internal reflections are guaranteed. On the other hand this angle cannot be too large: first, because the space between the DCH and the EMC is limited; second, because the uniformity of the calorimeter response is affected by this value.

- The use of a photon trap applied on the tile sides at larger radius in order to select the photons which are allowed to propagate up to the PMTs. The final timing resolution is the result of a trade-off between the number of photoelectrons and their spread in time. The highest timing accuracy is due to photons propagating either directly or with one side bounce. One wants to prevent multiple reflections which only result in lower accuracy. This loss of accuracy is caused by the chromatic broadening of the timing resolution for photons with a long optical path length.
- The optimization of the tile thickness. The thicker it is, the higher the number of Cherenkov photons emitted. However, as these photons are distributed uniformly along the particle trajectory, their emission time spread increases as well. Moreover, the tiles should be kept thin in order to minimize pre-showering in front of the calorimeter endcap.
- There are many other effects to be taken into account given the timing accuracy goal: (a) the T_0 resolution due to bunch length; (b) the track length, direction and position in the quartz tile; (c) the quartz tile geometrical accuracy and alignment; (d) the detector transit time spread; (e) the electronics resolution; (f) the chromatic broadening; etc.
- One has also to demonstrate that this detector will be able to run at 16 kG and will

survive very high rates with small aging effects. This is a crucial issue for this particular concept.

In addition, as this new apparatus would have to be installed in a small and quite populated area between the DCH and the EMC forward endcap, its integration requires inputs and feedbacks from the two neighboring systems. In particular, a joint 'DIRC-like' time-of-flight & forward EMC mechanical design is mandatory as this new detector must be located as close as possible from the calorimeter endcap to minimize the loss of information due to pre-showers in the additional material.

Finally, the full timing accuracy of the 'DIRC-like' TOF detector should be very good to achieve the $\pi - K$ separation goal: a few tens of ps at most. As the front-end electronics must not be limiting the precision of the measurements, their precision must be at the few ps level. Therefore, R&D programs are currently ongoing in Hawaii and LAL-Orsay to design waveform digitizing electronics able to fulfill these requirements while being cheap enough and robust enough.

References

- [1] B. Ratcliff, SLAC-PUB-5946, 1992 and "Simple considerations for the SOB redesign for SuperB", <http://agenda.infn.it/conferenceDisplay.py?confId=458>, SuperB PID meeting, March 18, 2008.
- [2] I. Adam *et al.*, Nucl. Instrum. Methods Phys. Res., Sect. A **583** (2007) 281-357.
- [3] J. Va'vra, <http://agenda.infn.it/conferenceDisplay.py?confId=1161>, Perugia, June 2009, and <http://agenda.infn.it/conferenceDisplay.py?confId=1742>, October 2009, SLAC.
- [4] J. Va'vra *et al.*, Nucl. Instrum. Methods Phys. Res., Sect. A **606** (2009) 404-410.
- [5] S.Korpar *et al.*, Nucl. Instrum. Methods Phys. Res., Sect. A **553** (2005) 64-69.

- A.Yu.Barnyakov *et al.*, Nucl. Instrum. Methods Phys. Res., Sect. A **553** (2005) 70-75.
- E. Kravchenko, <http://agenda.infn.it/conferenceDisplay.py?confId=1161>, June 2009, Perugia.
- [6] J. Benitez *et al.*, SLAC-PUB-12236, October 2006.
- [7] J. Va'vra *et al.*, SLAC-PUB-12803, March 2007.
- [8] J. Benitez *et al.*, Nucl. Instrum. Methods Phys. Res., Sect. A **595** (2008) 104-107.
- [9] J. Va'vra, "Simulation of the FDIRC optics with Mathematica", SLAC-PUB-13464, 2008, and "Focusing DIRC design for SuperB", SLAC-PUB-13763, 2009.
- [10] D. Roberts, "Geant 4 model of FDIRC", <http://agenda.infn.it/conferenceDisplay.py?confId=1742>, October 2009, SLAC.
- [11] C. Field *et al.*, "Development of Photon Detectors for a Fast Focusing DIRC", SLAC-PUB-11107, 2004.
- [12] D. Breton, E. Delagnes, J. Maalmi, "Picosecond time measurement using ultra fast analog memories", talk and proceedings at TWEPP-09, Paris, September 2009.
- [13] G. Varner, Nucl. Instr. Methods Phys. Res., Sect. A **538** (2005) 447.
- [14] J. Va'vra, "SLAC cosmic ray telescope facility", SLAC-PUB-13873, Jan. 2010.

6 Electromagnetic Calorimeter

The SuperB electromagnetic calorimeter (EMC) provides energy and direction measurement of photons and electrons, and is an important component in the identification of electrons versus other charged particles. Three principle components make up this system, the barrel calorimeter, the forward endcap calorimeter, and the backward endcap calorimeter, see Fig. 1.

Table 2 shows the solid angle coverage of each calorimeter. The total solid angle covered for a massless particle in the center-of-mass (CM) is 94.1% of 4π .

In addition to the BaBar simulation for the barrel calorimeter, simulation packages for the new forward and backward endcaps are available, both in the form of a full simulation using the GEANT4 tools, and in the form of a fast simulation package for parametric studies. These packages are used in the optimization of the calorimeter, and to study the physics impact of different options.

6.1 Barrel Calorimeter

The barrel calorimeter for SuperB is the existing BABAR CsI(Tl) crystal calorimeter.[1] Estimated rates and radiation levels indicate that this system will continue to survive and function in the SuperB environment. It covers 2π in azimuth and polar angles from 26.8° to 141.8° in the lab. There are 48 rings of crystals in polar angle, with 120 crystals in each azimuthal ring, for a total of 5,760 crystals. The crystals range from 16-17.5 X_0 in length. The BaBar barrel calorimeter will be largely unchanged for SuperB; we indicate planned changes here.

We are considering adding one more ring of CsI crystals at the backward end of the barrel. These crystals will be obtained from the current BaBar forward calorimeter. Space is already available for the added crystals in the existing mechanical structure, although some modifica-

Table 2: Solid angle coverage of the electromagnetic calorimeters. Values are obtained assuming the barrel calorimeter is in the same location with respect to the collision point as for *BABAR*. The CM numbers are for massless particles and nominal 4 on 7 GeV beam energies. The barrel SuperB row includes one additional ring of crystals over *BABAR*.

Calorimeter	$\cos \theta$ (lab)	$\cos \theta$ (CM)	Ω (CM)(%)
Backward	(-0.974,-0.869)	(-0.985,-0.922)	3.1
Barrel (<i>BABAR</i>)	(-0.786,0.893)	(-0.870,0.824)	84.7
Barrel (SuperB)	(-0.805,0.893)	(-0.882,0.824)	85.2
Forward	(0.894,0.965)	(0.825,0.941)	5.8

tion is required to accommodate the additional readout.

The existing barrel PIN diode readout is kept at SuperB. In order to accommodate the higher event rate, the shaping time is decreased. The existing ‘‘CARE’’ chip covers the required dynamic range by providing four different gains to be digitized in a 10 bit ADC. However, this system is old, and the failure rate of the analog-to-digital boards (ADBs) is unacceptably high. Thus, a new ADB has been designed, along with new very front end boards. The new design, Fig. 19, incorporates a dual-gain scheme, to be digitized by a twelve-bit ADC. In order to provide good least-count resolution on the 6 MeV calibration source, an additional calibration range is provided on the ADB.

6.2 Forward Endcap Calorimeter

The forward electromagnetic calorimeter for SuperB will be a new device, based on LYSO (Lutetium Yttrium Orthosilicate, with Cerium doping) crystals. Coverage starts at the end of the barrel and extends to 300 mradian in the lab. The crystals maintain the almost projective geometry of the barrel. This system replaces the CsI forward calorimeter used in *BABAR*. The advantages of LYSO include a much shorter scintillation time constant (LYSO: 40 ns, CsI: 680 ns and 3.34 μ s), a smaller Molière radius (LYSO: 2.1 cm, CsI: 3.8 cm), and greater resistance to radiation damage. One radiation length is 1.14 cm in LYSO and 1.85 cm in CsI.

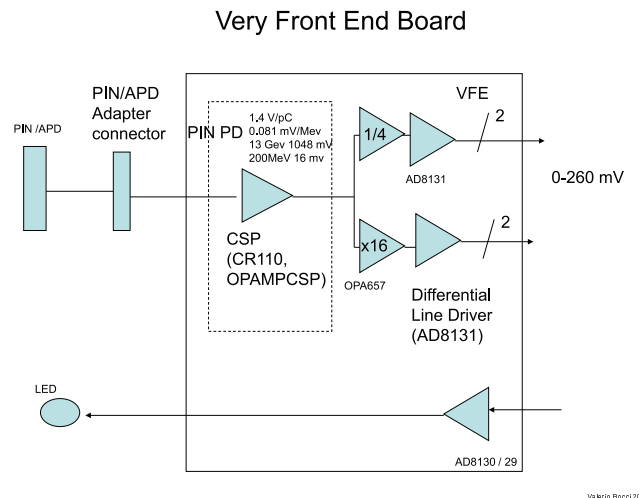


Figure 19: Block diagram for the very front end board, for the barrel and forward endcap signal readout.

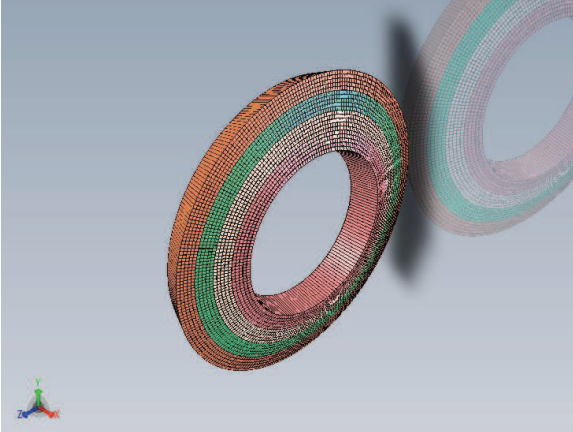


Figure 20: Arrangement of the LYSO crystals in groups of rings.

There are 20 rings of crystals, arranged in four groups of 5 layers each. Each group of five layers is arranged in modules five crystals wide. The preferred endcap structure is a continuous ring. However, the numbers of each type of module are multiples of 6, permitting the detector to be split in two halves, should that be necessary from installation considerations. The grouping of crystals is summarized in Table 3 and illustrated in Fig. 20.

Table 3: Layout of the forward endcap calorimeter.

Group	Modules	Crystals
1	36	900
2	42	1050
3	48	1200
4	54	1050
Total		4500

Each crystal is up to $2.5 \times 2.5 \text{ cm}^2$ at the back end, with a projective taper to the front. The maximum transverse dimensions are dictated by the Molière radius and by the desire to obtain two crystals from a boule. The length of each crystal is approximately 20 cm, or $17.5 X_0$.

The support structure for the crystals is an aveolar constructed of either carbon fiber or

glass fiber. This structure is bounded by two cones at the radial extremes. The outer cone is a carbon fiber structure, 6-10 mm thick, in order not to put too much material between the endcap and barrel. There is no such material issue for the inner cone, which is 20-30 mm of aluminum.

With the inclusion of the source calibration system (see below) and the front cooling system, the total front thickness may reach 20-30 mm. A good solution that minimizes material in front of the calorimeter is to embed the two pipe works into the foam core of a sandwich panel completed by two skins of 2-3 mm carbon fiber. An alternative is under investigation: Instead of adding the piping mass to the support material, the calibration and cooling circuits are depressions in pressed aluminum sheets forming the two skins of the front wall. The support at the back may be thick, and provides the load-bearing support for the forward calorimeter. It is constructed as either an open frame or closed plate, out of stainless steel.

Two possible readouts are under study, PIN diodes as used the barrel, and APDs (Avalanche Photodiodes). As for the barrel, redundancy is achieved with 2 APDs or PIN diodes per crystal. APDs, with a low-noise gain of order 50, offer the possibility of measuring signals from sub-MeV radioactive sources. This would obviate the need for a step with photomultipliers during the uniformity measurement process during calorimeter construction. The disadvantage of APDs is the gain dependence on temperature, requiring tight control of the readout temperature. The same electronics as for the barrel is used, with an adjustment to the VFE board gain with the APD choice.

The source calibration system is a new version of the 6.13 MeV calibration system already used in *BABAR*, as also used for the barrel calorimeter. This system uses a neutron generator to produced activated ^{16}N from fluorine in Fluorinert [2] coolant. The activated coolant is circulated near the front of the crystals in the detector, where the ^{16}N decays with a 7 s half-life.

The 6.13 MeV photons are produced in the decay chain $^{16}\text{N} \rightarrow ^{16}\text{O}^* + \beta$, $^{16}\text{O}^* \rightarrow ^{16}\text{O} + \gamma$.

Two beam tests are planned to study the LYSO performance and the readout options. The first beam test is at Frascati's Beam Test Facility, covering the 50-500 MeV energy range. The second beam test is at CERN, to cover the GeV energy range. In addition, a prototype avalanche is being constructed for the beam test structure.

Simulation studies are underway to optimize the detector configuration. In many cases, it is important to use a realistic clustering algorithm in these studies. In the actual event environment, clustering is important because there are multiple particles in an event, requiring pattern recognition. Fig. 21 shows how the measured energy distribution changes for different reconstruction algorithms.

It is also observed that adding material can remove photons from the peak into a long low-energy tail without showing up as a degradation in a local resolution measure such as FWHM. For example, for 100 MeV photons, the FWHM resolution does not worsen as one expects as large amounts of material is added. However, we may see that this is an artefact of the measure used by looking at the actual measured energy distributions in Fig. 22. The (FWHM) widths of the peaks for 25 and 60 mm of quartz preceding the calorimeter are about the same, but the distribution for 60 mm has a substantially larger low-energy tail.

Thus, a more meaningful measure that we may use is:

$$f_{90} \equiv \frac{E_{\text{true}} - E_{90}}{E_{\text{true}}},$$

where E_{true} is the energy of the generated photon and E_{90} gives the 10% quantile of the measured energy distribution. That is, 90% of measurements of the photon energy are above this value.

With this measure, the effect of putting material, such as a forward time-of-flight particle identification system, in front of the forward calorimeter has been studied. Fig. 23 shows the effect on the f_{90} measure of resolution.

Ideally, the transition between the barrel and forward calorimeters should be smooth, in order to contain the electromagnetic showers and to keep pattern recognition simple. Some possibilities for particle identification however require the forward calorimeter to be moved back from the IP relative to the smooth transition point. The effect of this on photon energy resolution has been studied, see Fig. 24. The resolution degrades in the barrel-endcap transition region as expected. The dependence on the z -position is not strong, and only appears at low energies.

6.3 Backward Endcap Calorimeter

The backward electromagnetic calorimeter for SuperB will be a new device (*BABAR* has none) based on a multi-layer lead-scintillator stack. The principal intent of this device is to increase hermeticity at modest cost. Excellent energy resolution is not a requirement; in any event there will be significant material from the drift chamber in front of it. Thus a high quality crystal calorimeter is not planned for the backward region. Longitudinal segmentation will provide capacity for π/e separation.

The backward calorimeter is located starting at $z = -1320$ mm, allowing room for the drift chamber front end electronics. The inner radius is 310 mm, and the outer radius 750 mm. The total thickness is $12 X_0$. It is constructed from a sandwich of 2.8 mm Pb alternating with 3 mm plastic scintillator (e.g., BC-404 or BC-408). The scintillator light is collected for readout in wavelength-shifting fibers (e.g., 1 mm Y11).

To provide for transverse spatial shower measurement, each layer of scintillator is segmented into strips. The segmentation alternates among three different patterns for different layers:

- Right-handed logarithmic spiral;
- Left-handed logarithmic spiral; and
- Radial wedge.

This set of patterns is repeated eight times to make a total of 24 layers. With this arrangement, the fibers all emerge at the outer radius

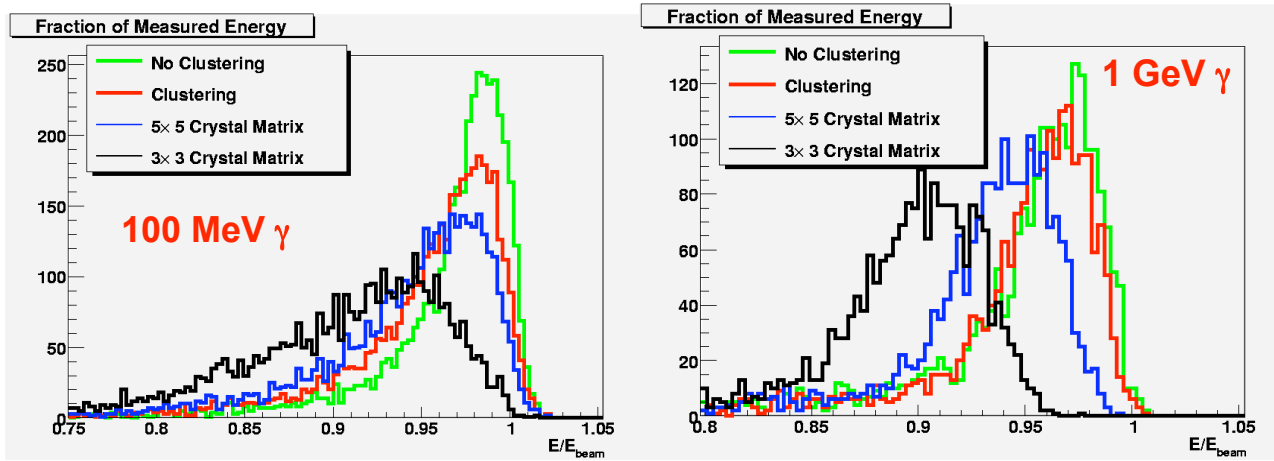


Figure 21: Effect on the measured energy distribution for various reconstruction algorithms. The “No clustering” distribution results from simply adding all crystal energies greater than 1 MeV. The “Clustering” distribution results from the algorithm used in *BABAR*. Left: 100 MeV photons; Right: 1 GeV photons.

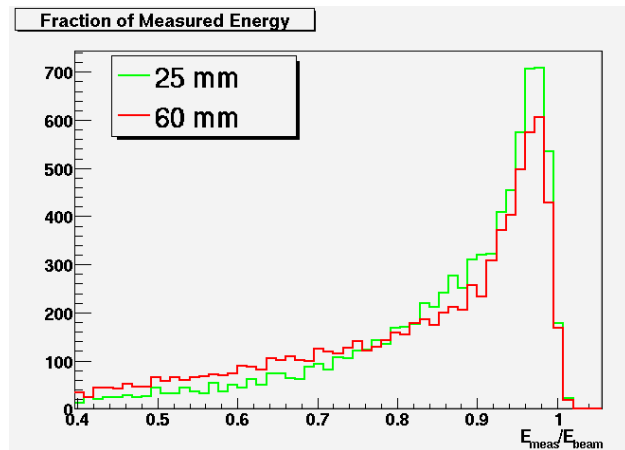


Figure 22: Measured energy in the forward calorimeter for 100 MeV photons and two different thickness of quartz in front of the calorimeter.

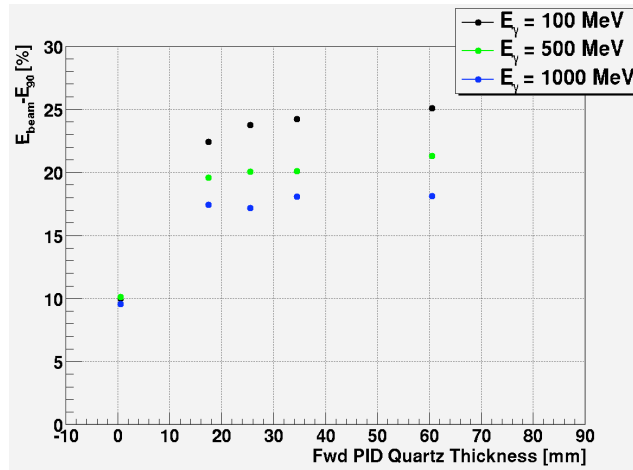


Figure 23: The effect of quartz material in front of the forward calorimeter, as a function of thickness and photon energy. The ordinate is f_{90} , expressed as per cent

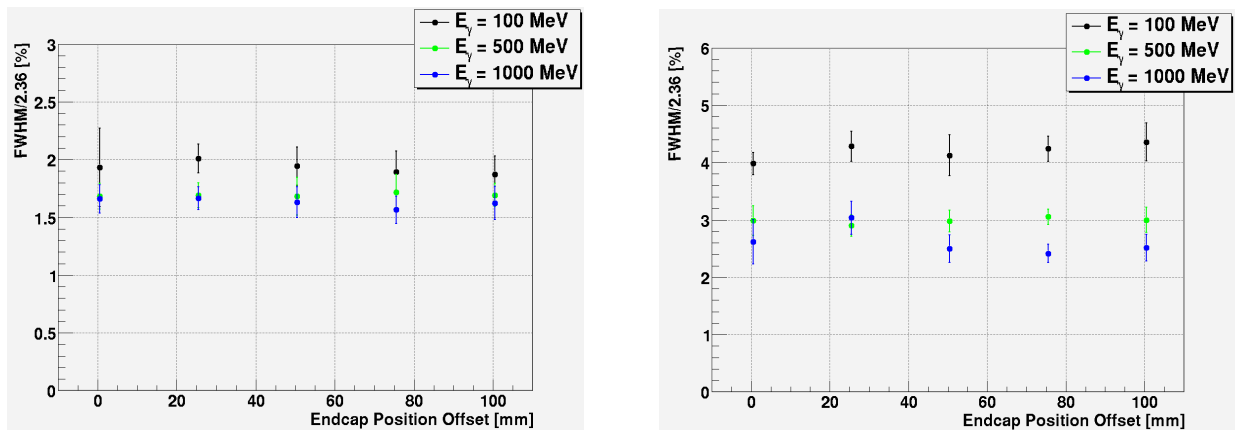


Figure 24: Effect on resolution of z -position of forward calorimeter. Left: Resolution as a function of position for showers away from the edges of the forward calorimeter. Right: Resolution as a function of position for showers in the transition region between the barrel and forward calorimeters.

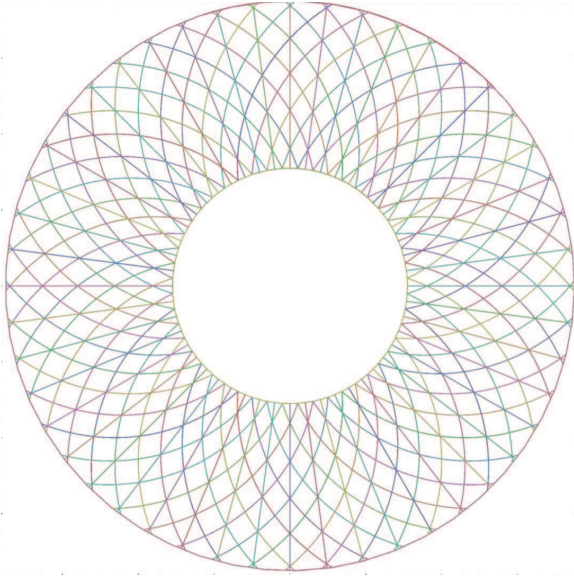


Figure 25: The backward EMC, showing the scintillator strip geometry for pattern recognition.

of the detector. There are 48 strips per layer, for a total of 1152 strips. The strip geometry is illustrated in Fig. 25

It is desirable to maintain mechanical integrity by constructing the scintillator layers with several strips from a single piece of scintillator, and not completely severing them. Isolation is achieved by cutting grooves at the strip boundaries. The optimization of this with respect to cross-talk and mechanical properties is under investigation.

The readout fibers are embedded in grooves cut into the scintillator. Each fiber is read out at the outer radius with a $1 \times 1 \text{ mm}^2$ multi-pixel photon counter (MPPC, or SiPM, for “silicon photomultiplier”). A mirror is glued to each fiber at the inner radius to maximize light collection. The SPIROC (SiPM Integrated Read-Out Chip) integrated circuit [3] developed for the ILC is used to digitize the MPPC signals, providing both TDC (100 ps) and ADC (12 bit) capability. Each chip contains 36 channels.

A concern with the MPPC’s is radiation hardness. Degradation in performance is observed in studies performed for the SuperB IFR, be-

ginning at integrated doses of order 10^8 1-MeV equivalent neutrons/cm² [4]. This needs to be studied further, and possibly mitigated with shielding.

Simulation studies are being performed to investigate the performance gain achieved by the addition of the backward calorimeter. The $B \rightarrow \tau \nu_\tau$ decay presents an important physics channel where hermeticity is a significant consideration. The measurement of the branching fraction has been studied in simulations to evaluate the utility of the backward calorimeter. Events in which one B decays to $D^0 \pi$, with $D^0 \rightarrow K^\pm \pi^\mp$, are used to tag the events, and several of the highest branching fraction one-prong τ decays are used.

Besides the selection of the tagging B decay, and one additional track for the τ , the key selection criterion is on E_{extra} , the energy sum of all remaining clusters in the EMC. This quantity is used to discriminate against backgrounds by requiring events to have low values; a reasonable criterion is to accept events with $E_{\text{extra}} < 400$ MeV.

In this study we find that the signal-to-background ratio is improved by approximately 20% if the backward calorimeter is present (Fig.26). The corresponding improvement in precision ($S/\sqrt{S+B}$) for 75 ab^{-1} is approximately 8% (Fig.3). We note that only one tag mode has so far been investigated, and this study is ongoing with work on additional modes to obtain results for a more complete sample analysis.

We are investigating the possibility of using the backward endcap for particle identification as a time-of-flight measuring device. Figure 27 shows, for example, for 100 ps timing resolution, a separation of more than three standard deviations can be achieved for momenta up to 1 GeV and approximately 1.5σ up to 1.5 GeV.

6.4 R&D

6.4.1 Barrel Calorimeter

The main R&D question for the barrel concerns the shaping time. Simulation work is underway

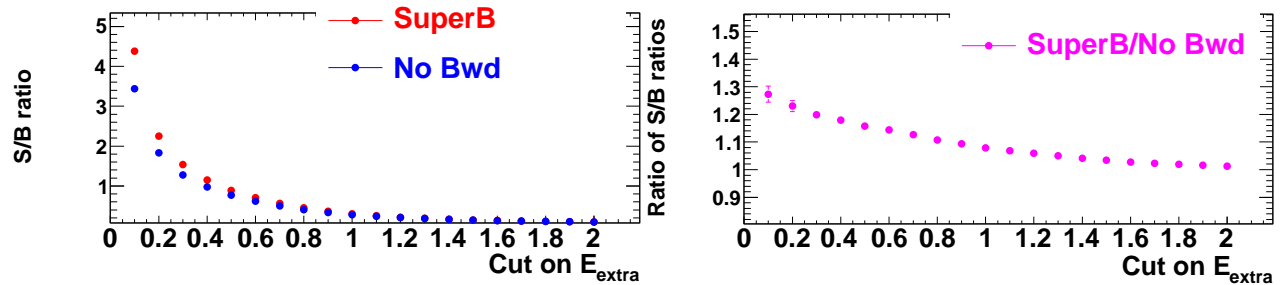


Figure 26: Left: Signal-to-background ratio with and without a backward calorimeter, as a function of the E_{extra} selection. Right: Ratio of the S/B ratio with a backward calorimeter to the S/B ratio without a backward calorimeter, as a function of the E_{extra} selection.

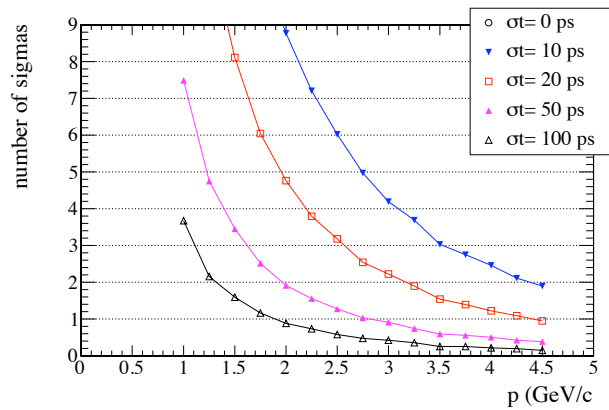


Figure 27: Kaon-pion separation versus measured momentum for different timing resolutions in the backward EMC region. The finite separation for perfect timing resolution is because measured momentum is used.

to investigate the pile-up from backgrounds. In addition, still to be addressed are the electronics and software issues connected with the possibility of adding one more ring of CsI crystals at the back end.

6.4.2 Forward Calorimeter

The forward calorimeter is a new device, and we are planning for two beam tests to test the performance of an LYSO crystal array as well as our solutions for the electronics and mechanical designs. We are investigating the use of PIN diodes and APDs as readout options. We plan as well to investigate the presence of material in front of the crystals in the beam test. Simulation work is ongoing to predict performance and backgrounds. There is an ongoing R&D effort with vendors to produce crystals with good light output and uniformity. The crystal support and integration of the calibration and cooling circuits with the mechanical structure is under investigation in consultation with vendors.

6.4.3 Backward Calorimeter

A beam test of the backward calorimeter is also planned, probably concurrent with the forward calorimeter beam test at CERN. The mechanical support and segmentation of the plastic scintillator is being investigated for a solution that achieves simplicity and acceptable cross-talk. The use of multi-pixel photon counters is being studied, including the radiation damage issue. The timing resolution for a possible time-of-flight measurement is an interesting question. Further simulation studies are being made to characterize the performance impact of the backward calorimeter.

References

- [1] The *BABAR* Collaboration, *The BABAR Detector*, Nucl. Instr. Meth, in Phys Res. **A479** (2002) 1.
- [2] Flourinert is the trademark name for polychlorotrifluoro-ethylene), manufac-

tured by 3M Corporation, St. Paul, MN, USA.

- [3] M. Bouchel, et al., “SPIROC (SiPM Integrated Read-Out Chip): Dedicated very front-end electronics for an ILC prototype hadronic calorimeter with SiPM read-out”, NSS '07 IEEE **3** (2007) 1857.
- [4] M. Angelone *et al.* “Silicon Photo-Multiplier radiation hardness tests with a beam controlled neutron source” arXiv:1002.3480.

7 Instrumented Flux Return

The Instrumented Flux Return (IFR) is designed primarily to identify muons, and, in conjunction with the electromagnetic calorimeter, to identify neutral hadrons, such as K_L^0 . This section describes the performance requirements and a baseline design for the IFR. The iron yoke of the detector magnet provides the large amount of material needed to absorb hadrons. The yoke, as in the *BABAR* detector, is segmented in depth, with large area particle detectors are inserted in the gaps between segments, allowing the depth of penetration to be measured.

In the Super*B* environment, the critical regions for the backgrounds are the small polar angles sections of the endcaps and the edges of the barrel internal layers, where we estimate that in the hottest regions the rate is a few $\times 100$ Hz/cm². These rates are too high for gaseous detectors. While the *BABAR* experience with both RPC's and LST's has been, in the end, positive, detectors with high rate characteristics are required in the high background regions of Super*B*. A scintillator-based system provides much higher rate capability than the gaseous detectors: for this reason, the baseline technology choice for the Super*B* detector is extruded plastic scintillator using WLS fiber read out with avalanche photodiode pixels operated in Geiger mode. The detailed discussion of all components will be done in the following subsections.

The IFR system must have high efficiency for selecting penetrating particles such as muons, while at the same time rejecting charged hadrons (mostly pions and kaons). Such a system is critical in separating signal events in $b \rightarrow s\ell^+\ell^-$ and $\rightarrow d\ell^+\ell^-$ processes from background events originating from random combinations of the much more copious hadrons. Positive identification of muons with high efficiency is also important in rare B decays as $B \rightarrow \tau\nu_\tau(\gamma)$, $B \rightarrow \mu\nu_\mu(\gamma)$ and $B_d(B_s) \rightarrow \mu^+\mu^-$ and in the search for lepton flavour-violating processes

such as $\tau \rightarrow \mu\gamma$. Background suppression in reconstruction of final states with missing energy carried by neutrinos (as in $B \rightarrow \mu\nu_\mu(\gamma)$) can profit from vetoing the presence of energy carried by neutral hadrons. In the *BABAR* detector, about 45% of relatively high momentum K_L^0 's interacted only in the IFR system. A K_L^0 identification capability is therefore required.

7.1 Performance optimization

7.1.1 Identification Technique

Muons are identified by measuring their penetration depth in the iron of the return yoke of the solenoid magnet. Hadrons shower in the iron, which has a hadronic interaction length $\lambda_I = 16.5$ cm [1]. The survival probability to a depth d scales as \exp^{-d/λ_I} . Fluctuations in shower development and decay in flight of hadrons with muons in the final state are the main source of hadron misidentification as muons. The penetration technique has a reduced efficiency for muons with momentum below 1 GeV/ c , due to ranging out of the charged track in the absorber. Moreover, only muons with a sufficiently high transverse momentum can penetrate the IFR to sufficient depth to be efficiently identified.

Neutral hadrons interact in the electromagnetic calorimeter as well as in the flux return. A K_L^0 tends to interact in the inner section of the absorber, therefore K_L^0 identification capability is mainly dependent on energy deposited in the inner part of the absorber, thus a fine segmentation at the beginning of the iron stack is needed. Best performance can be obtained by combining the initial part of a shower in the electromagnetic calorimeter with the rear part in the inner portion of the IFR. An active layer between the two subsystems, external to the solenoid, is therefore desirable.

7.1.2 Baseline Design Requirements

The total amount of material in the *BABAR* detector flux return (about 5 interaction lengths at normal incidence in the barrel region including the inner detectors) is suboptimal for μ

identification [2]. Adding iron with respect to the *BABAR* flux return for the upgrade to the Super*B* detector can produce an increase in the pion rejection rate at a given muon identification efficiency. One of the goals of the simulation studies is to understand if the *BABAR* iron structure can be upgraded to match the Super*B* muon detector requirements. A possible longitudinal segmentation of the iron is showed in Fig. 28. The three inner detectors are most useful for K_L^0 identification; the coarser segmentation in the following layers preserves the efficiency for low momentum muons.

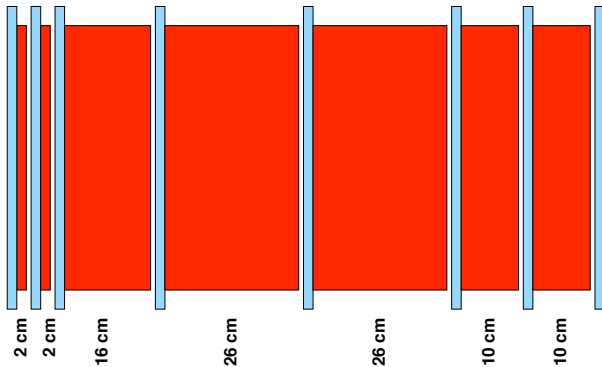


Figure 28: Sketch of the longitudinal segmentation of the iron absorber (red) in the baseline configuration. Active detector positions are shown in light blue from the innermost (left) to the outermost (right) layers.

The layout presented in Fig. 28 has a total amount of 92 cm of iron and can allow the reuse of the *BABAR* flux return with some mechanical modification. It's currently our baseline configuration, nevertheless it's only one among different possible designs that are under study. The final steel segmentation will be chosen on the basis of Monte Carlo studies of muon penetration and charged and neutral hadron interactions. Preliminary results of the simulation studies are shown in the next paragraph.

7.1.3 Design optimization and performance studies

We are performing the detector optimization by means of a GEANT4 based simulation in order to have a reliable description of the hadronic showers. The simulation includes also some detector feature coming from R&D studies such as spatial resolution, detection efficiency and electronic noise. Single muons and pions with momentum ranging between 0.5 GeV/*c* and 4 GeV/*c* have been shot in the detector and their tracks reconstructed and analyzed to extract relevant quantities for a cut based muon selector. Preliminary results obtained using the baseline detector configuration reveal an average muon efficiency of about 87% with a pion contamination of 2.1% over the entire momentum range. The efficiency and misidentification probability for muons and charged pions as function of the particle momentum are shown in Fig. 29.

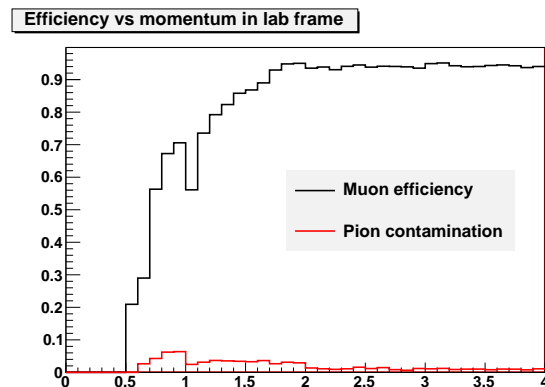


Figure 29: Efficiency and misidentification probability for muons and charged pions as function of the particle momentum. Study performed with baseline detector configuration.

Despite the good results obtained with the baseline configuration more extensive studies are needed before taking the final decision for the detector design: a fine comparison with other iron layouts will be done by means of a neural network algorithm for the particle identi-

fication. Further simulation studies will include also the effect of the machine background on the detector performances and a detailed investigation of the neutral hadrons.

7.2 R&D

Scintillators. Main requirements for the scintillator are a good light yield and a fast response. Both these requirements depend on the scintillator material characteristics and on the geometry adopted for the bar layout. Since more than 20 Metric Tons of scintillator will be used in the final detector, another major constraint is the cost that should be minimized. We found the extruded scintillator produced by the FNAL-NICADD facility (used also in the MINOS experiment [3]) suitable for our detector.

Given the foreseen space constraints, (the gaps between two iron absorbers are roughly 25 mm), the bar thickness shouldn't exceed 20 mm. The bar width is 4 cm and the fibers are placed in 3 holes extruded with the scintillator. We have two possible layouts for the bar:

- 1 cm thick, to put inside a gap two separate detection layers.
- 2 cm thick, in this case the gap is filled with only one bigger active layer.

The two scintillator layouts have been used to study two different readout options: a Time readout and a Binary readout. In the Time readout, one coordinate is determined by the scintillator position and the other by arrival time of the signal read with a TDC. In this case both the coordinates will be measured by the same scintillator bar (that is 2 cm thick) so there is no ambiguity in case of multiple tracks, but the resolution of one coordinate is limited by the time resolution of our system that is about 1ns. In the Binary readout option, the track is detected by two orthogonal 1-cm-thick scintillator bars. The spatial resolution is driven by the width of the bars (that is 4 cm as for the Time readout), but in case of multiple tracks a combinatorial association of the hits must be done.

WLS Fibers. For our application the fibers are required to have a good Light Yield, to ensure a high detection efficiency and a time response fast enough to allow a $\simeq 1 ns$ time resolution. We have tested WLS fibers from Saint-Gobain (BCF92) and from Kuraray (Y11-300) [4]. Both companies produce multicladd fibers with a good attenuation length ($\lambda \simeq 3.5 m$) and trapping efficiency ($\varepsilon \simeq 5\%$) but Kuraray have a higher light yield while Saint-Gobain have a faster response (decay time $\tau = 2.7ns$, while for the Kuraray $\tau \simeq 9.0ns$).

Photodetectors. Recently developed devices, called Geiger Mode APDs, suit rather well our needs of converting the light signal in a tight space and high magnetic field environment. These devices have high gain ($\simeq 10^5$), good Detection Efficiency ($\simeq 30\%$), fast response (risetime $\approx 200 ps$), and are very small (few mm) and insensitive to magnetic field. But then they have a rather high dark count rate ($\approx 1 MHz/mm^2$ at 1.5 p.e.) and the sensitivity to radiation. We tested $1 \times 1 mm^2$ SiPM, produced by IRST-FBK and MPPC, produced by Hamamatsu [5]. The comparison between SiPMs and MPPCs showed a lower detection efficiency of the former but also a faster response and a less critical dependence from temperature and bias voltage. In order to couple the photodetector with up to four $\phi = 1.0 mm$ fibers, we also tested $2 \times 2 mm^2$ FBK and $3 \times 3 mm^2$ Hamamatsu devices; the latter was too noisy for our purpose, therefore we are currently considering the SiPM as baseline.

7.2.1 R&D tests and results

R&D Studies were performed using mainly cosmic rays, with the setup placed inside a custom built 4 m long "dark box" to keep scintillators, fibers and photodetectors in a light tightened volume.

Given the sensitivity to radiation we studied the possibility to keep the SiPMs off detector, in a low radiation area, and bring the light signal to the photodetectors through about 10 m of clear fibers. We tried to recover the light

loss using more than one fiber per scintillator bar: Fig. 30 shows the comparison of the collected charge in a $2 \times 2 \text{ mm}^2$ SiPM through 1, 2, 3 WLS fibers. With 3 fibers in the scintillator we would recover a factor 1.65 while putting a fourth fiber would add only another 10% of more light: not enough for our purposes. The light loss is too high to bring the photodetector out of the iron therefore we have to couple the SiPM to the WLS fibers inside the detector, at the end of the scintillator bars and to shield them properly.

A systematic study has then been performed with the photodetectors directly coupled to the WLS fibers. The detection efficiency (ε) and the time resolution (σ_T) have been measured in the most critical points. Fig. 31 (right) shows a typical time distribution while all the results are reported in Table 4. The goal is to have a detection efficiency $\varepsilon > 95\%$ and, for the Time readout only, a time resolution $\sigma_T \simeq 1 \text{ ns}$ (that would translate to a longitudinal coordinate resolution $\sigma_z \simeq 20 \text{ cm}$). From Table 4 we see that, in order to have some safety margin, the minimum number of fibers to be placed inside the scintillator is 3.

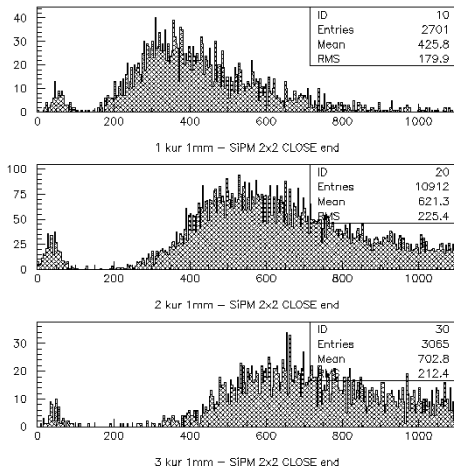


Figure 30: Light collected by 1, 2 and 3 fibers coupled to a SiPM $2 \times 2 \text{ mm}^2$.

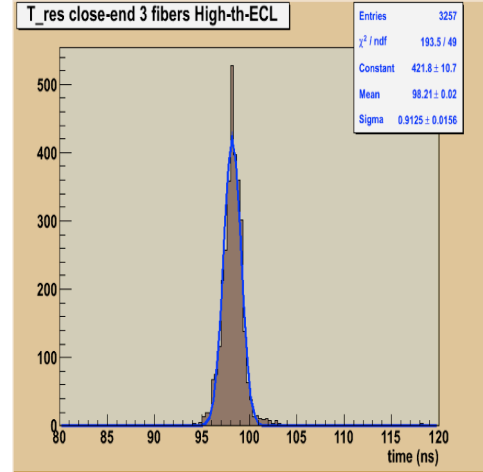


Figure 31: Fit to the time distribution of the SiPM signal.

A radiation test have also been carried out at the Frascati Neutron Generator facility (ENEA laboratory). First results ([7]) show that radiation effects start from an integrated dose of $\simeq 10^8 \text{ n/cm}^2$ and remain rather stable up to a dose of $\simeq 7 \times 10^{10} \text{ n/cm}^2$; in this range, the irradiated SiPMs continue to work with lower efficiency and higher dark rate.

7.2.2 Prototype

R&D achievements will be tested on a full scale prototype that is currently in preparation and that will be used to validate the simulation results. The prototype is composed by a full stack of iron with a segmentation which allows the study of different detector configurations. The active area is $60 \times 60 \text{ cm}^2$ for each gap. Scintillator slabs, full length WLS fibers and photodetectors will be located in light-tightened boxes (one for each active layer) placed within the gaps. The prototype will be equipped with 8 active layers: 4 having Binary readout and 4 with Time readout. A beam test will be done at Fermilab using a muon/pion beam with momentum ranging between $1 \text{ GeV}/c$ to $5 \text{ GeV}/c$. Beside the muon identification capability with different iron configurations, which is the main purpose of the beam test, detection efficiency

TIME READOUT						
	Time Resolution (ns)			Detection Efficiency (%)		
2 fibers	1.5 p.e.	2.5 p.e.	3.5 p.e.	1.5p.e.	2.5p.e.	3.5 p.e.
0.3 m	0.91	0.95	–	95.4	98.6	–
2.2 m	1.38	1.44	–	95.9	96.5	–
3 fibers	1.5 p.e.	2.5 p.e.	3.5 p.e.	1.5p.e.	2.5p.e.	3.5 p.e.
0.3 m	0.89	0.91	0.97	94.2	98.9	99.4
2.2 m	1.16	1.17	1.26	95.9	99.1	99.1

BINARY READOUT						
	Time Resolution (ns)			Detection Efficiency (%)		
2 fibers	1.5 p.e.	2.5 p.e.	3.5 p.e.	1.5p.e.	2.5p.e.	3.5 p.e.
2.4 m	1.87	2.16	2.14	98.8	97.4	91.6
3 fibers	1.5 p.e.	2.5 p.e.	3.5 p.e.	1.5p.e.	2.5p.e.	3.5 p.e.
2.4 m	1.60	1.65	1.76	98.7	99.2	98.5

Table 4: Summary of measurements for the Time and Binary readout. The few % lowering of the detection efficiency at 1.5 p.e. threshold is a dead time effect due to the high rate

and spatial resolution of the detector will be also measured.

7.3 Baseline Detector Design

Although the final detector design will be decided after the prototype test, a baseline layout can be preliminary derived by the R& D studies, the simulation results and the experience with the *BABAR* muon detector. Both Binary and Time readout have pros and cons from the performance point of view, but they both match the requirements for *SuperB*. Mechanically, the installation of the Binary readout, with orthogonal layers of scintillator, would be rather complicated in the barrel due to the limited access to the gaps. On the other hand, the region of the endcaps at low radii is subjected to high radiation and it's not a suitable place for the photodetectors. Therefore we currently plan to instrument the barrel region with Time readout, with the photodetectors on both ends of the bars and to instrument the endcaps with Binary readout reading the bars only on one side. The number of fibers is 3 per scintillator bar for each readout mode, the photodetectors are placed inside the gaps just at the end of the bars. The signal is brought to the electronics card, placed

outside the iron, by means of about 10 meters of coaxial cable. A detailed description of the Frontend electronics will be given in the Electronics section.

7.3.1 Flux Return

The baseline configuration foresees the reuse of the *BABAR* Flux Return with some mechanical modifications. The design thickness of the absorbing material in *BABAR* was 650 mm in the Barrel and 600 mm in the Endcaps; in order to improve the muon identification the thickness was then increased up to 780 mm in the Barrel and up to 840 mm in the Forward Endcap by replacing some active layers with brass plates and adding a steel plate in the forward part of the Endcap. In the *SuperB* baseline design, the total thickness of the absorbing material is 920 mm, corresponding to 5.5 interaction lengths. This can be achieved both by filling more gaps with metal plates (brass or low permeability stainless steel), or by recovering a 100 mm steel thickness in the Barrel which was not used in *BABAR*. The last point requires heavy modifications to the support structures surrounding the Barrel Flux Return. Due to the increased

weight a general reinforcement of the support elements has to be foreseen.

References

- [1] W.-M. Yao *et al.*, “Review of Particle Physics”, *J. Phys. G* **33**, 1 (2006).
- [2] B. Aubert *et al.* [BABAR Collaboration], “The *BABAR* Detector” *Nucl. Instrum. Methods Phys. Res., Sect. A* **479**, 1 (2002) [arXiv:hep-ex/0105044].
- [3] MINOS collaboration, “The MINOS Technical Design Report” *NuMI Note*, NuMI-L-337.
- [4] Bicron specs @ <http://www.detectors.saint-gobain.com/fibers.aspx>
Kuraray specs @ <http://www.df.unife.it/u/baldini/superB/Kuraray.pdf>
- [5] C. Piemonte *et al.*, ”Development of Silicon PhotoMultipliers at FBK-irst”, *Il Nuovo Cimento C*, vol. 30, no. 5, pp. 473-482
MPPC specs @ <http://sales.hamamatsu.com/en/products/solid-state-division/si-photodiode-series/mppc.php>
- [6] M. Andreotti *et al.*, “A Muon Detector based on Extruded Scintillators and GM-APD Readout for a Super B Factory”, *Nuclear Science Symposium Conference Record*, 2009. NSS '09. IEEE(2009).
- [7] M. Angelone *et al.* “Silicon PhotoMultiplier radiation hardness tests with a beam controlled neutron source” arXiv:1002.3480 [physics.ins-det].

8 Electronics, Trigger, DAQ and Online

8.1 Overview of the Architecture

The architecture proposed for the Super*B* Electronics, Trigger, Data acquisition and Online systems (ETD) has evolved from the *BABAR* architecture, thanks to the experience gained from running *BABAR* and building the LHC experiments. The detector side of the system is synchronous and all sub-detector readouts are now triggered. This limits the number of links between the front-end electronics (FEE) and the readout modules (ROMs) and permits a good understanding and easy commissioning of the experiment. In Super*B* standard links like Ethernet are the default, custom hardware links are only used where necessary.

A crucial difference to *BABAR* is that the potentially higher radiation levels make it mandatory to design radiation-safe on-detector electronics.

The first-level hardware trigger uses specialized data streams from the sub-detectors and provides its information to the fast control and timing system (FCTS) which is the centralized bandmaster of the system. The FCTS distributes the clock and the fast commands to all elements of the architecture and controls the readout of the events.

8.1.1 Trigger Strategy

The *BABAR* and Belle experiments both chose to use “open triggers”, attempting to preserve nearly 100% of $B\bar{B}$ events of all topologies, and a very large fraction of $\tau^+\tau^-$ and $c\bar{c}$ events. This choice has facilitated the very broad physics program of these experiments, albeit at the cost of a large cross-section of events to be logged and reconstructed, since it is quite difficult to reliably separate the signal from the $q\bar{q}$ ($q = u, d, s$) continuum and from higher-mass two-photon physics.

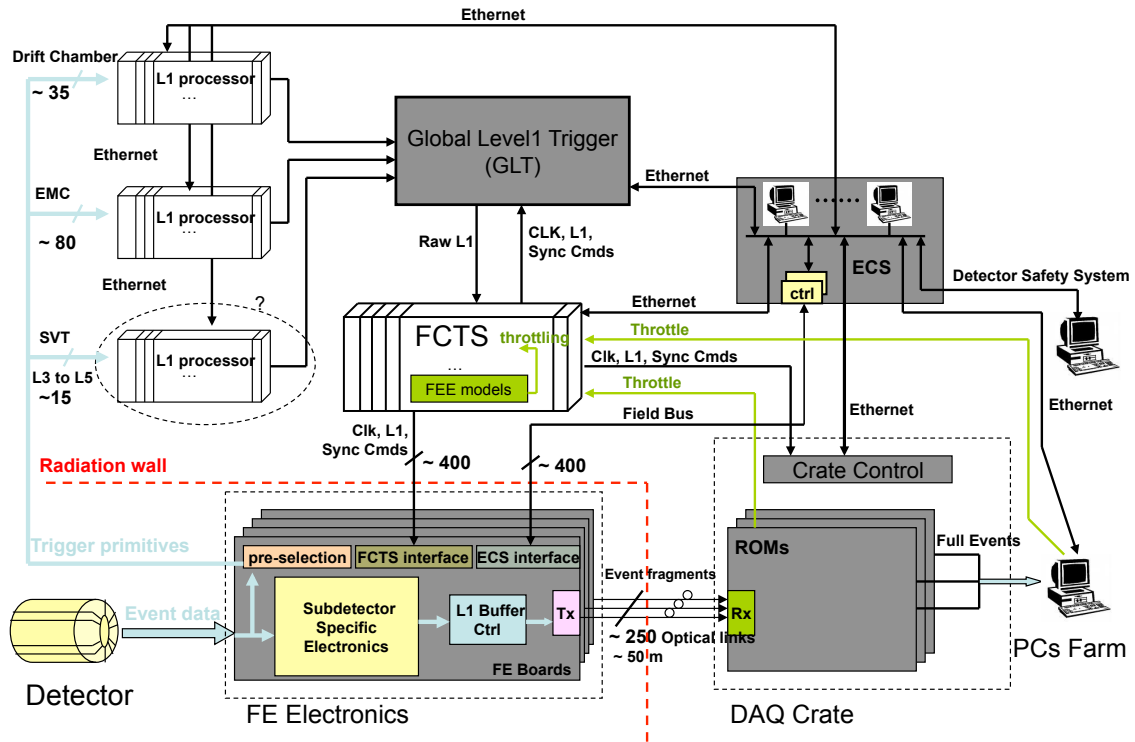


Figure 32: Overview of the ETD and Online global architecture

The physics program envisioned for Super B requires very high efficiencies for a wide variety of $B\bar{B}$ events and depends on continuing this strategy, since few classes of the relevant B decays provide the kinds of clear signatures that would allow the construction of specific triggers.

The trigger system consists of the following components¹:

Level 1 (L1) Trigger A synchronous, fully pipelined trigger that receives continuous data streams from the detector independently of the event readout and delivers readout decisions with a fixed latency and a time window (due to the fact that the collision rate is much higher than the trigger precision). While we do not yet

¹ While at this time we do not foresee a “Level 2” trigger that acts on partial event information in the data path, the data acquisition system architecture would allow the addition of such a trigger stage at a later time, hence the nomenclature.

have conducted detailed trigger studies, we expect the L1 trigger to be similar to the $BABAR$ L1 trigger, operating on reduced-data streams from the drift chamber and the calorimeter. We will study the possibilities of including SVT information, taking advantage of faster FPGAs, faster drift chamber sampling, the faster forward calorimeter and improvements to the trigger readout granularity of the EMC.

Level 3 (L3) and Level 4 (L4) Triggers The L3 trigger is a software filter that runs on a commodity computer farm and bases its decisions on a specialized fast reconstruction of complete events.

Additionally, a “Level 4” filter may be implemented to reduce the volume of permanently recorded data. It would base its decision on partial or full reconstruction of complete events. Depending on the worst-case performance guarantees of the reconstruction algorithms, it may

be necessary to decouple this filter from the “dead time path”, hence its designation as a separate stage. Throughout this document, the L3 and L4 triggers are also referred to as “High Level Triggers” (HLT).

8.1.2 Trigger Rates and Event Size Estimation

Compared to the CDR, the L1-accept rate capability of the system has been increased from 100 kHz to 150 kHz. This allows more flexibility at the L1 trigger level and adds headroom to accommodate increased backgrounds (e.g. during machine commissioning) or the machine exceeding its design luminosity of $10^{36} \text{ cm}^{-2}\text{sec}^{-1}$.

The event size estimate still has large uncertainties. Raw event sizes (between front-end electronics and ROMs) are now understood well enough to determine the number of fibres required, however it is still not known what algorithms will be applied in the ROMs for data size reduction (such as zero suppression or feature extraction) and what reduction can be achieved. While the 75 kbytes event size extrapolated from *BABAR* for the CDR is still our best estimate, the event size could be increased significantly by the Layer 0 of the SVT and/or the forward calorimeter. **In this document we will use 150 kHz L1-accept rate and 75 kbytes per event as a baseline.**

With the prospect of future luminosity upgrades, we should study how the system can be upgraded to handle up to four times the design luminosity, which elements need to be designed upfront to allow or facilitate such an upgrade, and, ultimately, what the associated cost would be.

8.1.3 Dead Time and Buffer Queue Depth Considerations

The readout system should be designed to handle an average rate of 150kHz and to be able to absorb the expected instantaneous rates, both without incurring dead time² of more than 1%

²Dead time is generated and managed centrally by the FCTS which will drop valid L1 trigger requests that

under normal operating conditions at design luminosity. The average rate requirement determines the overall system bandwidth, the instantaneous trigger rate requirement affects the FCTS, the data extraction capabilities of the front-end-electronics and the depth of the de-randomization buffers. The average time interval between bunch crossings at design luminosity is about 5 ns (future luminosity upgrades will further reduce this time). Compared to the detector response times, this interval is so short that for the purposes of trigger and FCTS design we can assume “continuous beams”. The burst handling capabilities (minimum time between triggers and maximum burst length) to achieve the dead time goal are therefore dominated by the capability of the L1 trigger to separate events in time and by the ability of the trigger and readout systems to handle events that are partially overlapping in space or time (pile-up, accidentals, etc.). Detailed detector and trigger studies are needed to determine these parameters.

8.2 Electronics, Trigger and DAQ

The Electronics, Trigger and DAQ (ETD) system covers all the hardware elements in the architecture, including the Fast Control and Timing System (FCTS), sub-detector-specific (FEE) and common parts (CFEE) of the front-end electronics for data readout and control, the Level 1 hardware trigger, the Readout Module boards (ROMs), the Experiment Control System (ECS) and the various links that interconnect these components.

The general design approach is to standardize components across the system as much as possible, to use mezzanine boards to isolate sub-system-specific functions from the standard design and to use commercially available common off-the-shelf (COTS) components where viable.

We will now describe the main components of the ETD in more detail:

would not fit into the readout system’s envelope for handling of average or instantaneous L1 trigger rates.

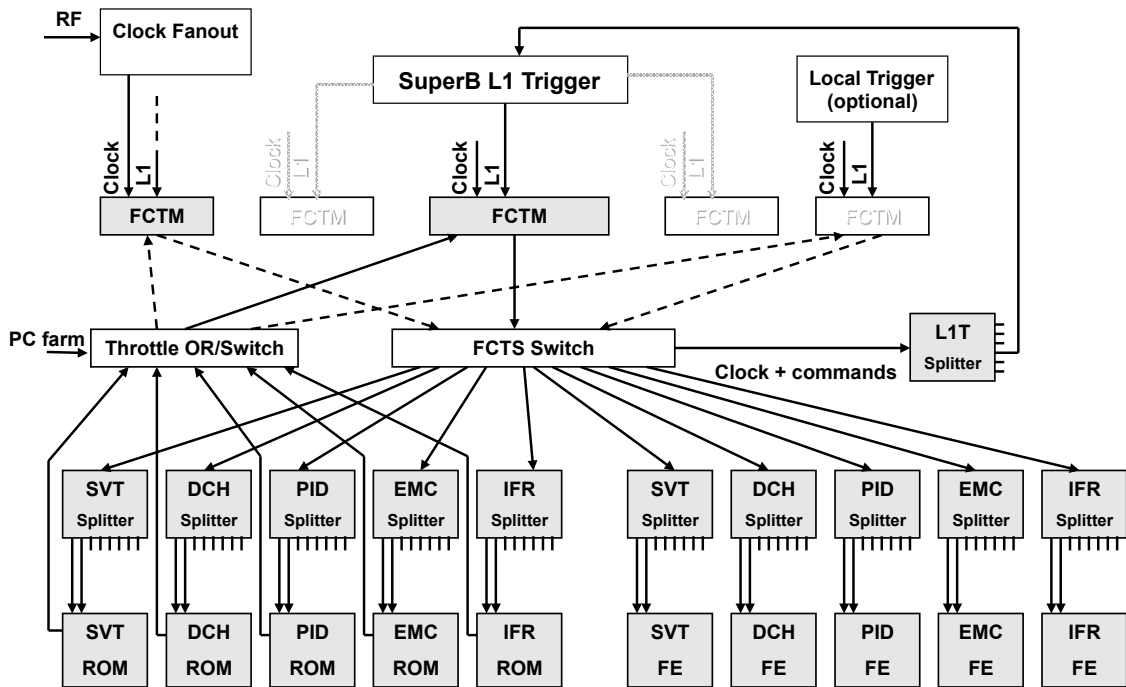


Figure 33: Fast Control and Timing System

8.2.1 Fast Control and Timing System

The Fast Control and Timing System (FCTS, Fig. 33) manages all elements linked to clock, trigger and event readout and is responsible for the partitioning of the detector into indepen-

dent sub-systems for testing and commissioning purposes.

The FCTS should be implemented in a crate where the backplane can be used to distribute all the necessary signals in point-to-point mode. This would permit delivery of very clean synchronous signals to all the boards and avoid the use of external cables. The Fast Control and Timing Module (FCTM, shown in Fig. 34) provides the main functions of the FCTS:

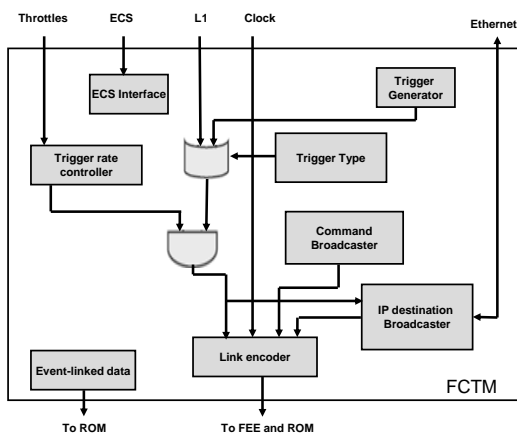


Figure 34: Fast Control and Timing Module

Clock and Synchronization The FCTS synchronizes the experiment with the machine, distributes the clock throughout the experiment, buffers the clock and generates synchronous reset commands.

Trigger Handling The FCTS receives the raw L1 trigger decisions, throttles them as necessary and broadcasts them to the sub-detectors.

Calibration and Commissioning The FCTS generates calibration pulses and flexibly programmable local triggers for calibration and commissioning.

Event Handling The FCTS generates event identifiers, manages the event routing and distributes event routing information to the ROMs. It also keeps a trace of all event-linked data that needs to be included with the readout data.

The FCTM board design will allow it to be present in the FCTS crate in as many instances as the number of partitions needed. One FCTM will be dedicated to the unused sub-systems in order to provide them with the clock and the minimum necessary commands.

To be able to partition the system into independent sub-systems or groups of sub-systems, two dedicated switches are required. One switch distributes clock and commands to the front-end boards, the other collects the throttling requests from the readout electronics or the ECS. These switches could be implemented on dedicated boards, connected with the FCTMs, and would need to receive the clock. To reduce the number of connections between ROM crates and the global throttle switch board, throttle commands could be combined at the ROM crate level before sending them to the global switch.

Instantaneous throttling of the data acquisition by directly inhibiting the raw L1 trigger from the front-end electronics will not be possible because the induced latency would be too long. Instead, models of the front-ends and the L1 event buffer queues will be emulated in the FCTM to instantaneously reduce the trigger rate if data volume exceeds the front-end capacity.

The FCTM also manages the distribution of events to the HLT farm for event building, deciding the destination farm node for every event. There are many possible implementations of the event building network protocol and the routing of events based on availability of HLT farm machines, so at this point we can only provide a high-level description.

Because of the simplicity and natural synchronization properties, we strongly prefer to use the FCTS for the distribution of event routing information to the ROMs. Management of event destinations would be implemented in FCTM firmware and/or software and may need to implement functions such as bandwidth management for the event building network and protocols to manage the event distribution based on the availability of farm servers.

“Continuation events” to deal with pile-up could either be merged in the ROMs or in the high-level trigger farm, but we strongly prefer to merge them in the ROMs. Merging them in the trigger farm would complicate the event builder and require the FCTS to maintain event state and adjust the event routing accordingly so that all parts of a continuation event are sent to the same HLT farm node.

8.2.2 Clock, Control and Data Links

The different serial links required for SuperB (for data transmission, timing and control commands distribution and read-out) represent a main element of the TDR phase by themselves.

Because of the fixed latency and low jitter constraints, simple solutions relying on off-the-shelf electronics components have to be thoroughly tested to validate them for use in clock and control links. Moreover, because of the expected radiation levels on the detector side, some R&D projects will be necessary to qualify the selected chipsets.

The difference in requirements for the various link types may lead to the choice of different technical solutions for different link types.

The links are used to distribute the frequency-divided machine clock (running at 56 MHz) and fast control signals such as trigger pulses, bunch crossing, event IDs or other qualifiers, to all components of the ETD system. Copper wires are used for short haul data transmission (< 1m), optical fibres for medium and long haul. To preserve the timing information, suitable commercial components will be chosen so that the latency of transmitted data and the phase of the clock recovered from the serial stream do

not change with power cycles, resets and loss-of-locks. Encoding and/or scrambling techniques will be used to minimize the jitter on the recovered clock. The same link architecture is also suitable for transmitting regular data instead of fast controls or a combination of both. Link types can be divided into two classes:

A-Type: Homogeneous links with both ends off-detector. Given the absence of radiation, they might be implemented with Serializer-Deserializers (SerDes) embedded in FPGAs. Logic in the FPGA fabric will be used to implement fixed latency links and to encode/decode fast control signals. A-Type links are used to connect the FCTS system to the DAQ crate control and to the Global Level 1 Trigger. A-Type links run at approximately 2.2 Gbits/s.

B-Type: Hybrid links with one end on-detector and the other end off-detector. The on-detector side might be implemented with off-the-shelf radiation-tolerant components, the off-detector end might still be implemented with FPGA-embedded SerDes. B-Type links connect the FCTS crate to FEE and the FEE to ROMs. The B-Type link speed might be limited by the off-the-shelf SerDes performance, but is expected to be at least 1 Gbit/s for the FCTS to FEE link and about 2 Gbits/s for the FEE to ROM link.

All links could be implemented as plug-in boards or mezzanines, allowing an easy upgrade of the links without affecting the host boards. A modular approach would also decouple the development of the user logic from the high-speed link design and simplify the user board layout. Mezzanine specifications and form-factors would likely be different for A- and B-Type links, but they would share as much as possible a common interface to the host board.

8.2.3 Common Front-End Electronics

Common Front-End Electronics (CFEE) designs and components would allow us to exploit the commonalities between the sub-detector

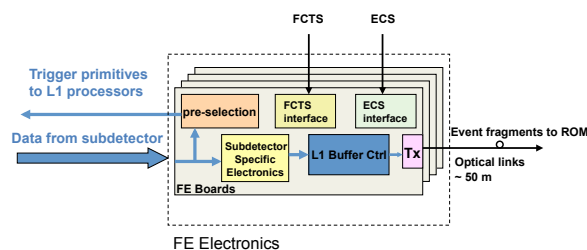


Figure 35: Common Front-End Electronics

electronics and avoid separate design and implementation of common functions for each sub-detector.

In our opinion it would be best to implement the separate functions required to drive the FEE in dedicated independent elements. These elements could be mezzanines or circuits directly mounted on the front-end modules (acting as carrier boards) and be standardized across the sub-systems as much as possible. For instance, as shown in Fig. 35, one mezzanine could be used for FCTS signal and command decoding, and one for ECS management. To reduce the number of links, it might also be possible to decode the FCTS and ECS signals on one mezzanine and then distribute them to the neighbouring boards.

Driving the L1 buffers may also be implemented by a dedicated common control circuitry inside a radiation-tolerant FPGA. This circuitry would handle the L1 accept commands and provide the signals necessary to control the reading of the latency buffer and the writing/transmitting of the proper event buffer. The latency buffers could be implemented either in the same FPGA or directly on the carrier boards. One such circuit could be able to drive numerous data links in parallel, thus reducing the amount of electronics on the front-end.

The control circuit would also have to handle the fast multiplexer feeding the optical link serializer, the special treatment of pile-up events (if implemented) and the possibility to extend the readout window back in time after a rejected Bhabha event (if implemented).

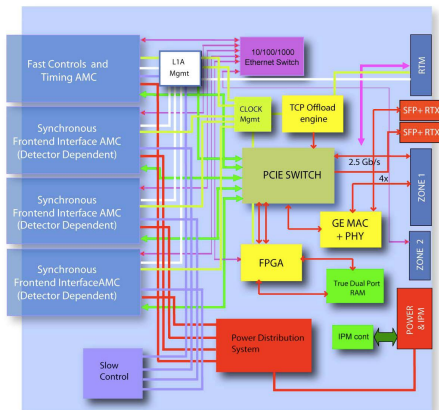


Figure 36: Readout Module

An important advantage of this approach is that it permits the alternative of implementing an analog L1 buffer inside an ASIC. Then the only (potentially non-trivial) constraint is that the analog output of the ASIC has to be able to drive an internal or an external ADC at a 56 MHz rate in order to keep the synchronization with the rest of the system. It may be possible to relax this rate constraint by running slower ADCs in parallel.

Serializers and link optical drivers should also reside on carrier boards, mainly for mechanical and thermal reasons. Fig. 35 shows a possible implementation of the L1 buffers, their control electronics and the outputs towards the optical readout links. The control electronics may sit within a dedicated FPGA. Both digital and analog buffer types are shown.

Another important requirement is that all (rad-tolerant) FPGAs in the FEE have to be reprogrammable without dismounting a board. This could be done through dedicated front panel connectors, which might be linked to numerous FPGAs, but it would be preferable if the reprogramming could be done through the ECS without any manual intervention on the detector side.

8.2.4 Readout Module

The Readout Module (ROM, Fig. 36) receives event fragments from the sub-detectors' front-end electronics, tags them with front-end identifiers and absolute time-stamps, buffers them in de-randomizing memories, performs processing (still to be define) on the fragment data, and eventually injects the formatted fragment buffers in the event builder processing farm. To accommodate different sub-detector requirements a modular approach is mandatory, while the use of standards across the system simplifies development and keeps the costs low. ROMs will be located in a non-hazardous area and connected to the front-end electronics via optical fibres.

Signals from optical receivers (which could be mounted on mezzanine cards) will be routed to the de-serializers of commercial FPGAs where data processing can take place. Special constraints or custom requirements of sub-detectors will be accommodated by custom-built mezzanines mounted on common carriers. One of the mezzanine sites on the carrier will host an interface to the FCTS to receive global timing and trigger information. The carrier itself will host memory buffers and 1 Gbit/s or 10 Gbits/s links to the event building network.

A baseline of 8 optical fibres per card currently seems like a good compromise between the number of ROM boards and their complexity. This density would allow to have one ROM crate per sub-detector and corresponds nicely to the envisaged FCTS partitioning.

8.2.5 Experiment Control System

The complete SuperB experiment (power supplies, front-end, DAQ, etc.) must be accessible through the control of the Experiment Control System (ECS). As shown in Fig. 32, the ECS will be responsible for the overall control of the experiment and the monitoring of its correct functioning:

Configuring the Front-ends Numerous front-end parameters must be initialized to spe-

cific values before the system can work correctly. The amount of parameters per channel can range from a few to complete per-channel lookup tables. If the system is working reliably, the loading of the front-end parameters does not need to be performed frequently. However some of the front-end electronics located on or near the detector may require frequent reloading of the complete set of front-end parameters to ensure that the local registers have not been corrupted by radiation-induced single event upsets. Since it is difficult to estimate size of this problem, it is critical to not have bottlenecks in the ECS itself and in the ECS' access to the front-end hardware. The ECS may also need to read back parameters from registers in the front-end hardware to check the status or verify that the contents have not changed.

Calibration Calibration runs require an extended functionality of the ECS. After loading calibration parameters, event data collected with these parameters must be sent through the DAQ system and analyzed, then the ECS must load the parameters for the next calibration cycle into the front-ends.

Testing the FEE We favour using the ECS for the remote testing of electronics modules located in the FEE over implementing an independent self-test capability for all modules, therefore dedicated software routines in the ECS context are required to perform these tests.

Monitoring the Experiment The ECS continuously monitors the correct functioning of the experiment. This includes independent spying on event data for data quality checks, monitoring of the correct function of power supplies (voltage and current limits, etc.) and of the cooling of crates and modules. Support for monitoring the FEE modules themselves must to a large extent be built into the FEE hardware so that the ECS can be informed about FEE failures. The ECS also acts as a first line of defense in protecting the experiment from hazards. In addition, an independent detector safety system

(part of the Detector Control System, see 8.3.6) has to protect the experiment against equipment damage in case the software-based ECS is not operating correctly.

The specific ECS bandwidth and functionality requirements of all sub-systems for loading front-end parameters, executing calibrations and tests, and experiment monitoring and control must be determined (or at least estimated) as early as possible so that the ECS can be designed according to these requirements. Development of calibration, test and monitoring routines must be considered an integral part of sub-system development as its functions require detailed knowledge about the sub-system internals.

Possible ECS Implementation The field bus used for the ECS has to be radiation tolerant on the detector side and provide very high reliability. Such a bus has been designed for the LHCb experiment: it is called SPECS (Serial Protocol for Experiment Control System) [4]. It is a bidirectional 10 Mbits/s bus that runs over standard Ethernet Cat5+ cable and provides all possible facilities for ECS (like JTAG and I2C) on a small mezzanine. It could be easily adapted to the SuperB requirements. Moreover, in the context of the upgrade of LHCb, SPECS which was initially based on PCI boards is currently being translated to an Ethernet-based system also integrating all the functionalities for the out-of-detector elements.

For the electronics located far from the detector, Ethernet will be used for ECS communication.

8.2.6 Level 1 Hardware Trigger

The L1 Trigger will be built as a synchronous machine running at 56 MHz, based on primitives produced by dedicated electronics located on the front-end boards or other dedicated boards of the respective sub-detector.

The main elements of the L1 trigger are shown in Fig. 37:

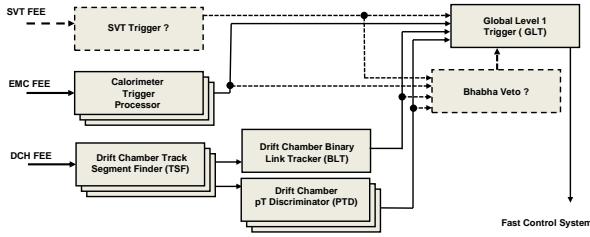


Figure 37: Level 1 Trigger Overview

Drift chamber trigger (DCT) The DCT consists of a track segment finder (TSF), binary link Tracker (BLT) and a p_t discriminator (PTD)

Electromagnetic Calorimeter Trigger (EMT)

The EMT processes the trigger output from the calorimeter to find clusters.

Global Trigger (GLT) The GLT processor combines the information from DCT and EMT (and possibly other inputs such as an SVT trigger or a Bhabha veto) and forms a final trigger decision that is sent to the FCTS.

The current baseline is to re-implement the *BABAR* L1 architecture with state-of-the art FPGAs and to investigate the addition of an SVT trigger and a Bhabha veto. If not fully custom, the standard chosen for the crates would most likely be ATCA for the crates and the back-planes.

Since the trigger latency directly impacts size and cost of the L1 data buffers in the sub-detectors, it is very desirable to reduce the trigger latency compared to the $12\ \mu\text{s}$ latency of the *BABAR* trigger. Faster sampling of the DCH, the new fast forward EMC, and a shortened shaping time of the barrel EMC may allow to improve the trigger event time precision which may ultimately enable us to reduce readout window sizes and the size of raw events.

Other opportunities of L1 trigger improvements enabled by faster FPGAs (e.g. tracking or clustering algorithm improvements) and the improved readout granularity of the EMC will be studied.

The raw L1 decisions are sent to the FCTM boards which applies a throttle if necessary and then broadcasts them to the whole experiment.

To debug and monitor the trigger and to provide cluster and track seed information to the higher trigger levels, select trigger information supporting the trigger decisions are read out on a per-event basis through the regular readout system. In this respect, the low-level trigger acts like just another sub-detector.

8.3 Online System

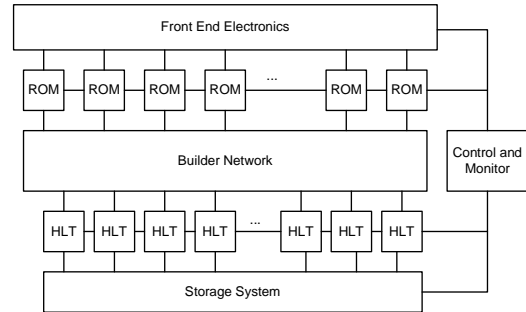


Figure 38: High-level view of the Online System

The Online system is responsible for reading out the ROMs, building complete events, filtering events according to their content (High Level Triggers, HLT) and to finally archive the accepted events for further physics analysis (Data Logging). It is also responsible for the continuous monitoring of the acquired data to understand detector performance and detect detector problems (Data Quality Monitoring). The Detector Control System (DCS) monitors and controls the detector and its environment.

Assuming a L1 trigger rate of 150 kHz and an event size of 75 kbytes, the input bandwidth of the Online system is about 12 Gbytes/s, corresponding to about 120 Gbits/s with overhead. The uncertainty of the event size and the overall system design suggests a safety factor of ~ 2 , so we should consider 250 Gbits/s as a baseline for the Online system input bandwidth.

Assuming that the HLT will accept a cross-section of about 25 nb leads to 25 kHz of ac-

cepted events at a luminosity of $10^{36} \text{ cm}^{-2}\text{sec}^{-1}$, or a logging data rate of $\sim 1.9 \text{ Gbytes/s}$.

The main elements of the Online system (Fig. 38) are described in the following sections.

8.3.1 ROM Readout and Event Building

The ROMs provide a parallel readout of the event fragments from sub-detector front-end electronics and the buffering of such fragments in deep de-randomizing memories. The information related to an event is then transferred into the ROM memories and sent over a network to an event buffer in one of the machines of the HLT farm. This collection task, called event building can be performed in parallel for multiple events, thanks to the depth of the ROM memories and bandwidth of the event building network switch (preferably non-blocking). Because of this inherent parallelism, the building rate can be scaled up as needed (up to the bandwidth limit of the event building network). We expect to use Ethernet as basic technology of the event builder and to use 1 Gbits/s and 10 Gbits/s links.

8.3.2 High Level Trigger Farm

The HLT farm needs to provide sufficient aggregate network bandwidth and CPU resources to handle the full Level 1 trigger rate on its input side. The Level 3 trigger algorithms should be able to operate and log data entirely free of event time ordering constraints and need to be able to take full advantage of modern multi-core CPUs. Extrapolating from *BABAR* we would expect 10 ms core time per event to be more than adequate to implement a software L3 filter, using a specialized fast reconstruction. With such a filter an output cross-section of 25 nb should be achievable.

To further reduce the amount of permanently stored data, an additional filter stage (L4) could be added that acts only on the events accepted by the L3 filter. This L4 stage could be an equivalent (or extension) of the *BABAR* offline physics filter, rejecting events based on a partial or full event reconstruction. If the worst-case

behavior of the L4 reconstruction code is well controlled, it could be run in near-real-time as part of or directly after the L3 stage, otherwise it may be necessary to use deep buffering to decouple the L4 filter from the near-real-time performance requirements imposed on the L3 stage. The discussion in the SuperB CDR about the risks and benefits of such a L4 filter still applies.

8.3.3 Data Logging

The output of the HLT is logged to disk storage. We assume at least a few Tbytes of usable space per farm node, either implemented as directly attached low-cost disks in a redundant (RAID) configuration or as a storage system connected through a network or SAN. We do not foresee aggregation of data from multiple farm nodes into larger files. Instead, the individual files from the farm nodes will be maintained in the downstream system. The bookkeeping system and data handling procedures need to be designed to handle non-monotonic runs and missing run contribution files. A switched Gigabit Ethernet network separate from the event builder network is used to transfer data asynchronously to archival storage and/or near-online farms for further processing. It has not been decided where such facilities will be located, but network connectivity with adequate bandwidth and reliability will need to be provided and the local storage available to the HLT farm will need to be sized to allow data buffering for the expected periods of link down time.

The format for the raw data has not been determined yet, some requirements are efficient sequential writing, reasonably compact representation of the data and the freedom to tune file sizes as needed to optimize storage system performance.

8.3.4 Event Data Quality Monitoring and Display

Event data quality monitoring is based on quantities calculated by the L3 (and possibly L4) trigger, as well as quantities calculated by a fast reconstruction pass on a subset of the data. A

distributed histogramming system collects the monitoring output histograms from all sources and makes them available to automatic monitoring processes and operator GUIs.

8.3.5 Run Control System

The control and monitor of the experiment is performed by the Run Control System, providing a single point of entry to operate and to monitor the whole experiment. It is a collection of software and hardware modules that handle the two main functions of this component: control, configuring and monitoring the whole Online system and provide its user interface. To achieve these goals, RCS interacts both with the Experiment Control System (ECS) and with the Detector Control System. We expect modern web technologies to be used for developing this component.

8.3.6 Detector Control System

The Detector Control System (DCS) is responsible for ensuring detector safety, controlling the detector and detector support system and for monitoring and recording detector and environment conditions.

Efficient detector operations in factory mode require a very high degree of automation and automatic recovery from problems. The DCS plays a key role in maintaining high operational efficiency and a tight integration with the Run Control System is highly desirable.

Low-level components and interlocks responsible for detector safety (Detector Safety System, DSS) will typically be implemented as simple circuits or with programmable logic controllers (PLCs).

The software component will be built on top of a toolkit that provides the interface to whatever industrial buses, sensors, and actuators may be used. It must provide a graphical user interface for the operator, have facilities to generate alerts automatically, and have an archiving system to record the relevant detector information. It must also provide software interfaces for programmatic control of the detector.

We expect to be able to use existing commercial products and controls frameworks developed by the CERN LHC experiments.

8.3.7 Other Components

Electronic Logbook A web-based logbook, integrated with all major Online components that allows operators to keep an ongoing log of the experiment status, activities and changes.

Databases Online and experiment-wide databases such as configuration, conditions and ambient databases to respectively keep track of intended detector configuration, calibrations and actual state and time-series information from the detector control system.

Configuration Management A configuration management system that defines and records all hardware and software configuration parameters in a configuration database.

Performance Monitoring A system to monitor performance across all components of Online.

Software Release Management A strict software release management and tracking system that allows to determine what software version (including any patches) was running at a given time in any part of the ETD/Online system. Release management should cover FPGA and other firmware.

Computing Infrastructure An Online computing infrastructure (specialized and general-purpose networks, file, database and application servers, operator consoles and other workstations) that is designed to provide high availability where affordable and to be self-contained and sufficiently isolated and firewalled to minimize external dependencies and downtime.

8.3.8 Software Infrastructure

The Online system is basically a distributed system built with commodity hardware elements.

We expect most of the developing efforts to be devoted to design the software components and a homogeneous approach is needed to drive both the design and implementation phase. An On-line software infrastructure helps in this direction. As a framework, it should provide basic memory management, communication services and the executive where the Online applications are executed. Online applications make use of these services to perform in a simplified way their functions. Middleware designed specifically for data acquisition exists and could provide a simple, consistent and integrated distributed programming environment.

8.4 Front-End Electronics

8.4.1 SVT Electronics

The SVT electronics shown in Fig. 39 has been designed to take advantage, where possible, of the data-push characteristics of the front-end chips. The time resolution of the detector will be dominated by the minimal time resolution of the FSSR2 chip, which is 132 ns. Events will be built from packets of three such minimal time slices (396 ns event time window). The readout chain in layer 0 will start from a half-module holding two sets of pixel chips (2 readout sections, ROS). Data will be transferred on wires to a few meters away from the interaction region where local buffers will store the read hits. As discussed in the SVT chapter, for layer 0

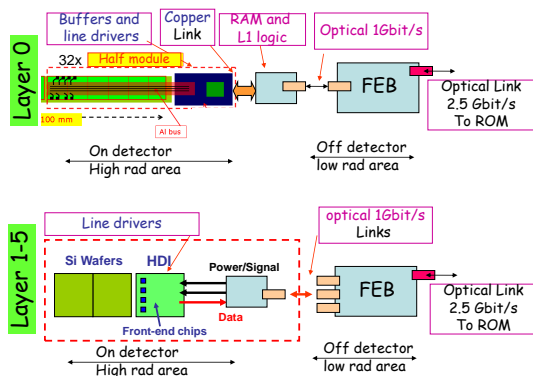


Figure 39: SVT Electronics

the data rate is dominated by the background and the bandwidth needed is in the range of 16 Gbits/s/ROS. The large bandwidth is the main reason to store hits close to the detector and transfer only hits from triggered events.

For events accepted by the L1 trigger, the bandwidth requirement is only 0.85 Gbits/s and data from each ROS can be transferred on optical links (1 Gbit/s) to the front-end boards (FEB) and then to ROMs through the standard 2 Gbits/s optical readout links. Layers 1-5 will be read out continuously and the hits will be sent to the front-end boards on 1 Gbit/s optical links. On the FEBs hits will be sorted in time and formatted to reduce event size (timestamp stripping). Hits of triggered events will then be selected and forwarded to the ROMs on the 2 Gbits/s standard links.

Occupancies and rates on layers 3-5 make them suitable for fast track searching so that SVT information could be used in the L1 trigger. The SVT could provide the number of tracks found, the number of tracks not originating from the interaction region and the presence of back-to-back events in the ϕ coordinate. A possible option for SVT participation to the L1 trigger would require two L1 trigger processing boards each one linked to the FEBs of layers 3-5 with synchronous optical links.

In total, the SVT electronics will require 58 FEBs and 58 ROMs plus optionally two L1 trigger processing boards, 58 optical links at 2 Gbits/s, 308 links at 1 Gbit/s (radiation hard) and - optionally - about 40 links at 1.25 Gbits/s for L1 trigger processing.

8.4.2 DCH Electronics

The design is still in a very early stage, so we only provide a baseline description of the drift chamber front-end electronics which does not include additional front-end features currently under study (such as a cluster counting capability).

The DCH will be used to provide charged particle tracking, dE/dx and trigger information. The front-end electronics must measure the drift time of the first electron and the total

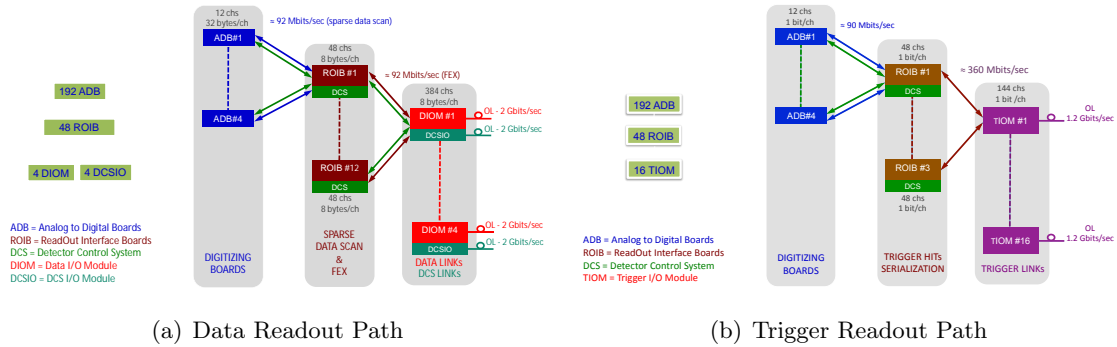


Figure 40: DCH Electronics

charge collected on the sense wires and generate the information to be sent to the L1 trigger.

The DCH front-end chain can be divided into three different blocks:

Very Front End Boards (VFEB) The VFEBs contain HV distribution and blocking capacitors, protection networks and preamplifiers. They could also host discriminators. The VFEBs must be located on the (backward) chamber end-plate to maximize S/N ratio.

Data Conversion and Trigger Pattern Extraction Data conversion includes TDC (1 ns resolution, 10 bits dynamic range) and continuous sampling ADC (6 bits dynamic range). Trigger data contains the status of the discriminated channels, sampled at about 7 MHz (compared to 3.7 MHz in *BABAR*). This section of the chain can be located either on the end-plate (power dissipation, radiation environment and material budget are issues) or in external crates (micro-coax or twisted cables must be used to carry out preamplifier signals).

Readout Modules The ROMs collect the data from the DCH FEE and send zero-suppressed data to DAQ and trigger.

The number of links required for data transfer to the DAQ system has been estimated based

on the following parameters: 150 kHz L1 trigger rate, 10k channels, 20% chamber occupancy in a $1 \mu\text{s}$ time window, 32 bytes per channel. At a data transfer speed of 2 Gbits/s per link, about 40 links are needed. 56 synchronous 1.25 Gbits/s links are required to transmit the trigger data sampled at 7 MHz. The topology of the electronics suggests that the number of ECS and FCTS links should be the same as the number of readout links.

8.4.3 PID Electronics

Forward PID Option There are currently two detector options for the forward PID.

The first option is to measure the time of flight (TOF) of particles from the interaction point to the PID detector. Two implementations are possible, a pixel detector which would lead to a large number of channels (7200), or a DIRC-like detector with quartz bars which would require only 192 channels. Both implementations would make use of fast Micro Channel Plate PMTs (MCP-PMT) and would have to provide a measurement of the hit time with a precision of ~ 10 ps. The readout would use fast analog memories which as of today are the best solution for a picosecond time measurement. To achieve this time resolution, the clock distribution will have to be very carefully designed and will likely require the direct use of the machine clock at the beam crossing frequency.

The second option is a Focusing Aerogel Cherenkov detector. It has the advantage of a higher resolution than the TOF option, but as it would reside in the magnetic field, standard multi-anode PMTs cannot be used. Thus its $\sim 115,000$ channels would have to be equipped with MCP-PMTs. Since the time precision needed is at the same level as that of the barrel, the same type of electronics could be used. 50 links would be the minimum amount necessary for the readout, and the maximum for the ECS and FCTS.

Barrel PID The barrel PID electronics has to provide the measurement of the arrival time of the photons produced in the quartz bars with a precision of about 100 ps rms. The new detector baseline is a focusing DIRC, which will permit using multi-anodes photo multipliers. The new design (reduced camera volume, different materials) reduces the background sensitivity by at least one order of magnitude, thus reducing the rate requirement for the front-end electronics.

As a baseline, the design would be implemented with 16-channel TDC ASICs offering the required precision of 100 ps rms. The amplitude could also be measured by a 12-bit ADC at least for calibration, monitoring and survey, and transmitted with the hit time. To provide both the sampling of the analog signal and its discrimination, a 16-channel front-

end analog ASIC also has to be designed. Both ASICs would be connected to a radiation-tolerant FPGA which would handle the hit readout sequence and push data into the L1 trigger latency buffers.

All this electronics setup has to sit right on the MAPMT base, where space is very limited and cooling is difficult. Therefore, crates concentrating front-end data and driving the fast optical links could be located outside the detector in a convenient place where some space is available. They would be connected to the front-end through standard commercial cables (like Cat 5 Ethernet cables). The readout mezzanines would be implemented there, as well as the FCTS and ECS mezzanines from where signals would be forwarded to the front-end electronics electrically through the same cables.

The system would be naturally divided into 12 sectors like the DIRC in *BABAR*. Using the baseline numbers (36,864 channels, 150 kHz trigger rate, 100kHz/channel hit rate, 32 data bits/hit, 2 Gbits/s link rate), the readout link occupancy should be of only $\sim 15\%$, thus offering a pleasant safety margin. A solution with other models of PMTs providing half the number of channels is also being studied.

Another option would be to use analog memories instead of TDCs to perform both time and amplitude measurements. This option offers more information on the hit signals but would be more expensive in terms of amount of electronics and of links. Its advantages and disadvantages are still under study.

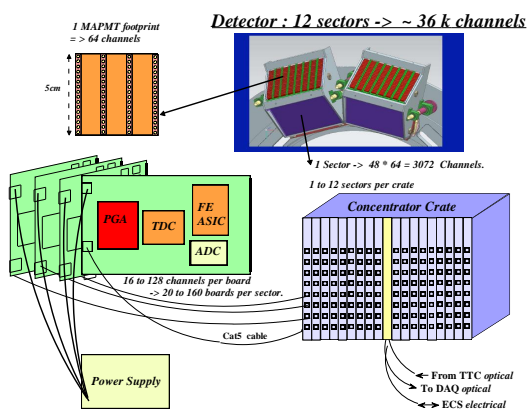


Figure 41: PID Electronics

8.4.4 EMC Electronics

For the EMC system, two options were considered: A *BABAR*-like push architecture where all calorimeter data are sent over synchronous optical 1 Gbit/s links to L1 latency buffers residing in the trigger system, or a “triggered” pull architecture where the trigger system receives only sums of crystals (via synchronous 1 Gbit/s links), and only events accepted by the trigger are sent to the ROMs through standard 2 Gbits/s optical links.

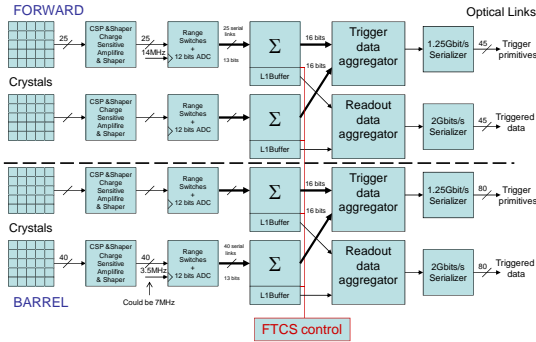


Figure 42: EMC Electronics

The triggered option, shown in Fig. 42, requires a much smaller number of links and was chosen as the baseline implementation. The reasons for this choice and the implications are discussed in more detail below.

To support the activated liquid-source calibration, where no central trigger can be provided, both the barrel and the end-cap readout systems need to support a free running “self-triggered” mode where only samples with an actual pulse are sent to the ROM. Pulse detection may require digital signal processing to suppress noisy channels.

Forward Calorimeter The 4500 crystals are read out with PIN or APD photodiodes. A charge preamplifier translates the charge into voltage and the shaper uses a 100 ns shaping time to provide a pulse with a FWHM of 240 ns.

The shaped signal is amplified with two gains (x1 and x64), and at the end of the analog chain an autorange circuit decides which gain will be digitized by a 12 bits pipeline ADC running at 14 MHz. The 12 bits of the ADC plus one bit for the range thus permits to cover the full scale from 10 MeV to 10 GeV with a resolution better than 1%. A special gain is set during calibration using a programmable gain amplifier in order to optimize the scale used during calibration with a neutron-activated liquid-source system around 6 MeV.

Following the design of the *BABAR* detector a push architecture with a full granularity readout scheme was first explored. The information of 4

channels is grouped using copper serial links to have an aggregate rate of 0.832 Gbits/s of the synchronous optical link 1 Gbit/s payload, requiring a total number of 1125 links. The main advantage of this architecture is the flexibility of the trigger algorithm that can be implemented off detector using state of the art FPGAs without the constraint of radiation. The main drawback is the cost due to the huge number of links.

The number of links can be reduced by summing channels together on the detector side and only sending the sums to the trigger: The natural granularity of the forward detector is a module which is composed of 25 crystals. In this case, data coming from 25 crystals is summed together, forming a word of 16 bits. Then the sums coming from 4 modules are aggregated together to produce a payload of 0.896 Gbits/s. In this case the number of synchronous links toward the trigger is only 45. The same number of links would be sufficient to send the full detector data with a 500 ns trigger window. This architecture limits the trigger granularity and implies more complex electronics on the detector side but reduces the numbers of links by a large amount (1125 down to 90). However, it cannot be excluded that a faster chipset appears on the market which could significantly reduce this gain.

Barrel Calorimeter The EMC barrel reuses the 5760 crystals and PIN diodes from *BABAR*, however the shaping will be reduced from 1 μ s to 500 ns and the sampling rate doubled from 3.5 MHz to 7 MHz. The same considerations about serial links for the forward EMC apply to the barrel EMC. If full granularity data were pushed synchronously to the trigger, about 520 optical links would be necessary.

The number of synchronous trigger links can be drastically reduced by performing sums of 4x3 cells on the detector side, so that 6 such energy sums could be continuously transmitted through a single optical serial link. This would permit to reduce the number of trigger links to match the topology of the calorimeter electronics boxes, which is split into 40 ϕ sectors on

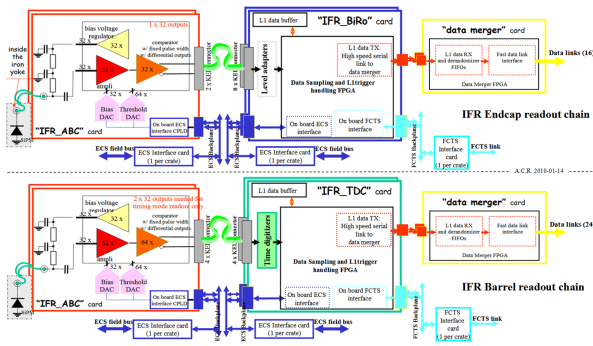


Figure 43: IFR Electronics

both sides of the detector. The total number of links would thus be 80 for the trigger and 80 for data readout toward the ROMs, both with a wide margin (factor > 1.5).

8.4.5 IFR Electronics

The IFR is equipped with plastic scintillators coupled to wavelength shifting fibres. Although different options have been explored, it is currently assumed that single photon counting devices (SiPM) will be located “inside” the iron, as close as possible to the scintillating assemblies. Each SiPM will be biased and read out through a single coaxial cable.

A schematic diagram of the IFR readout electronics is shown in Fig. 43. The first stage of the readout chain is based on the IFR_ABC boards which provide (for 32 channels each):

- Amplification, presently based upon off-the-shelf components (COTS)
- Individually programmable bias voltages for the SiPMs
- Comparators with individually programmable thresholds, presently based on COTS

To minimize the length of the coaxial cables from the SiPMs to the IFR_ABC boards, these boards need to be placed as close to the iron yoke as possible. The digital outputs of the IFR_ABC boards will then be processed in different ways for the IFR barrel and end-caps.

IFR Barrel The signals from the scintillators in the IFR barrel (all parallel to the beam axis) are read out with IFR_TDC 64-channel timing digitizer boards. Recording the time of arrival of pulses from both ends of the scintillating elements permits to determine the Z-position of particle hits (during reconstruction).

The channel count estimate for the barrel is: 14,400 TDC channels: 3600 scintillating assemblies in the barrel read out at both ends, 2 comparators (with different threshold) per channel to improve timing resolution.

IFR End-caps The signals from the scintillators in the IFR end-caps (which are positioned vertically and horizontally) are read out with IFR_BiRO 128 channel “Binary Readout” boards, which sample the status of the input lines and update a circular memory buffer from which data is extracted upon trigger request.

The channel count estimate for the end-caps is: 9,600 BiRO channels: 2 end-caps, each with 2,400 scintillating assemblies in X, 2,400 scintillating assemblies in Y and a single comparator per channel.

The IFR_TDC and IFR_BiRo digitizers should be located as closely as possible to the IFR_ABC boards to minimize the cost of the interconnecting cables, preferably in an area of mitigated radiation flux. In this case commercial TDC ASICs could be used in the design. Alternatively, radiation-tolerant TDCs could be used closer to the detector. The FPGAs used in the digitizers should be protected against radiation effects by architecture and by firmware design.

The output streams from the IFR_TDC and IFR_BiRO boards would go through custom “data concentrators” to merge the data coming from a number of digitizers and send the resulting output data to the ROMs via the standard optical readout links.

In total, 225 IFR_TDC boards (12 crates) and 75 IFR_BiRO boards (4 crates) are needed. The total number of links to the ROMs is presently estimated to 24 for the barrel (2 links per digi-

tizer crate) and 16 for the end-caps (4 links per digitizer crate).

To optimize the electronics topology, the number of ECS and FCTS links should match the number of readout links.

8.5 R&D

For the overall EDT/Online system, the main R&D topics are the global system requirements and possible upgrade paths to handle luminosities of up to $4 \times 10^{36} \text{ cm}^{-2}\text{sec}^{-1}$ during the lifetime of the experiment.

Data Links The data links for SuperB will require R&D in the following areas: Studying jitter related issues and filtering by means of jitter cleaners, coding patterns for effective error detection and correction, radiation qualification of link components and performance studies of the serializers/deserializers embedded in the new generation of FPGAs (Virtex6, Xilinx, etc.)

Readout Module Readout Module R&D would include investigation of 10 Gbits/s Ethernet technology and detailed studies of the I/O sub-system on the ROM boards. The possibility of implementing the ROM functions in COTS computers by developing suitable PCIe boards (such as optical link boards for FCTS and FEE links or personality cards to implement sub-detector-specific functions) should be investigated.

Trigger For the L1 trigger, the minimally achievable latency and physics performance will need to be studied. The studies will need to take into account and address: Improved time resolution and trigger-level granularity of the EMC, faster sampling of the DCH, potential inclusion of SVT information at L1, possibility of a L1 Bhabha veto, possibilities of handling pile-up and overlapping (spatially and temporally) events at L1 and opportunities created by modern FPGAs to improve the trigger algorithms.

For the HLT, studies of achievable physics performance and rejection rates need to be conducted, including the risks and benefits of a possible L4 option.

ETD Performance and Dead Time The design parameters for the ETD system driven by trigger rates and dead time constraints will need to be studied in detail to determine the requirements for trigger distribution through the FCTS, FEE/CFEE buffer sizes and the required capabilities for handling pile-up and overlapping events. Input from the L1 trigger R&D and from background studies will be required.

Event Builder and HLT Farm The main R&D topics for Event Builder and HLT Farm are: Applicability of existing tools and frameworks for constructing the event builder and HLT farm framework, event building protocols and how they map onto network hardware.

Software Infrastructure Investigate how much of the software infrastructure, frameworks and code implementation can be shared with Offline computing. Determine the correct level of reliability engineering required in such a shared approach. Develop frameworks to take advantage of multi-core CPUs.

8.6 Conclusions

Designing the architecture of the ETD system for SuperB our main goal was to optimize its simplicity and reliability while keeping its cost as reasonable as possible. Experience has been taken from building, commissioning and running the BABAR experiment as well as from building and commissioning the LHC experiments. The proposed system is simple and safe. Trigger and data readout are fully synchronous which permits an easy understanding and commissioning. Safety margins have been included everywhere possible, especially concerning background and radiation levels. Event readout and event building is centrally supervised by the FCTS system which continuously

collects all the information necessary to consequently optimize the trigger rate. Hardware trigger will be redesigned to improve its efficiency and reduce its latency and the event size will be kept reasonable.

For the Online components the same considerations apply: leveraging existing experience, technology and toolkits developed by *BABAR* and the LHC experiments and COTS computing and networking, we will build a simple and operationally highly efficient system to serve the needs of *SuperB* factory-mode data taking.

References

- [1] *SuperB Conceptual Design Report*, <http://www.pi.infn.it/SuperB/CDR> arXiv:0709.0451v2 [hep-ex]
- [2] The *BABAR* Collaboration, *The BABAR Detector*, Nucl. Instr. Meth, in Phys Res. **A479** (2002) 1.
- [3] The *BABAR* Trigger Web Pages, <http://www.slac.stanford.edu/BFROOT/www/Detector/Trigger/index.html>
- [4] The SPECS Web Page, <https://lhcb.lal.in2p3.fr/Specs/>

9 Software and Computing

The computing models of the *BABAR* [?] and *BELLE* [?] experiments have proven to be quite successful for a flavor factory in the $\mathcal{L} = 10^{34} \text{ cm}^{-2}\text{s}^{-1}$ luminosity regime. A similar computing model can work also for a super flavor factory at a luminosity of $\mathcal{L} = 10^{36} \text{ cm}^{-2}\text{s}^{-1}$. Predictable progress in computing industry will indeed provide much of the performance increase needed to cope with the larger data volumes. The actual development of the *SuperB* computing model is planned to start with a dedicated R&D effort in the second half of 2010 and to finish with the completion of the Computing TDR by the end of 2011. However, to illustrate the scale of the project, a description of the current baseline model and a summary of the computing requirements are presented here.

During the last two years, the main effort of the computing group has been devoted to the development and the support of the simulation software tools and the computing production infrastructure needed for the design of the detector and the evaluation of its physics performance. The description of the current status of such activities is therefore also reported.

9.1 The baseline model

The “raw data” coming from the detector are permanently stored, and run through the reconstruction pass that consist of two steps:

- a “prompt calibration” pass performed on a subset of the events to determine various calibration constants.
- a full “event reconstruction” pass on all the events that uses the constants derived in the previous step.

Reconstructed data are also permanently stored and data quality is monitored at all steps in the process.

A comparable amount of Monte Carlo simulated data is also produced in parallel and processed in the same way.

In addition to the physics triggers, the data acquisition also records random triggers that are used to create “background frames”. Monte Carlo simulated data, incorporating the calibration constants and the background frames on a run-by-run basis, are prepared.

Reconstructed data, both from the detector and from the simulation, are stored in two different format:

- the Mini that contains reconstructed tracks and energy clusters in the calorimeters as well as detector informations. It is a relatively compact format, through noise suppression and efficient packing of data.
- the Micro that contain only informations essential for physics analysis.

Detector and simulated data are made available to physics analysis in a convenient form through the process of “skimming”. This involves the production of selected subsets of the data, the “skims” designed for different areas of analysis. Skims are very convenient for physical analysis, but increase the storage requirement because the same events can be present in more than one skim.

From time to time, as improvements in constants, reconstruction code, or simulation are implemented, the data may be “reprocessed” or new simulated data generated. If a set of new skims become available, an additional skim cycle can be runned on all the reconstructed events.

9.1.1 The requirements

The SuperB computing requirements can be estimated using as a basis the present experience with *BABAR* and applying a scaling of about two orders of magnitude. Fortunately, much of this scaling exercise is quite straightforward.

As a baseline, we simply scale all rates linearly with luminosity. Only a few parameters have been modified to keep into account improved efficiency of utilization of the computing resources that are likely to be obtained with SuperB, i.e.:

- the skimmed data storage requirements have been reduced (by $\sim 40\%$), assuming a more aggressive use of events indexing technique;
- the CPU requirements for physics analysis are reduced by a factor of two as a result of more stringent optimization goals that can be achieved in SuperB;
- the backup copy of the raw data has been dropped, since in *BABAR* less than 3

The resulting CPU and storage requirements are shown in Table 5 for a typical year of data taking at nominal luminosity.

Table 5: Summary of computing requirements for a typical year of SuperB data taking at nominal luminosity, expressed as increments over the preceding year.

Parameter	typical Year
Luminosity (ab^{-1})	12
Storage (PB)	
Tape	27.8
Disk	11.5
CPU (MSpecInt2000)	
Data reconstruction	14.7
Skimming	21.5
Monte Carlo	93.2
Physics analysis	44.4
Total	173.8

The total amount of computing resources to be made available for one year of data taking at nominal luminosity will be similar to the corresponding figure estimated by the Atlas or CMS experiments for the year 2010. As it’s the case for the LHC experiments, SuperB will make large use of distributed computing resources accessible via the Grid infrastructures. This will introduce an important flexibility factor in provisioning the required level of computing resources.

9.2 Computing tools and services for the Detector TDR studies

9.2.1 Detector fast simulation

9.2.2 Bruno: the SuperB full simulation tool

The availability of reliable tools for full simulation is crucial in the present phase of the design of both the accelerator and the detector.

First of all, the background rate at the sub-detectors needs to be carefully assessed for each proposed accelerator design. Secondly, for a given background scenario, the designs of the sub-detectors themselves must be optimized to obtain optimal performance. The full simulation tool can be used to improve the results of the fast simulation in some particular cases, as discussed in the following. The choice was made to re-write from scratch the core simulation software, aiming at having more freedom to better profit from both the Babar legacy and the experience gained in the development of the full simulation for the LHC experiments. Geant4 as the underlying technology was therefore the natural choice, as well as C++ as the programming language.

While the implementation is still at a very early stage, its present status already allows the resulting software to be usable. Basic functionality is in place, and more is being added following user requests. We will give in the following a short overview of the main characteristics, emphasizing areas where future development is planned.

Geometry description The need to re-use as much as possible the existing geometrical description of the Babar full simulation, called for some interchange, application-independent format to convey the information concerning the geometry and materials of the sub-detectors. Among the formats currently used in High Energy Physics applications, the Geometry Description Markup Language (GDML) was chosen due to the availability of native interfaces in Geant4 and ROOT and the easyness of human inspection and editing provided by the XML-based structure.

The choice of GDML also brings in some limitations, of course, one being for example the limited support for loops and volume parameterization. In the longer term, with the progressive stabilization of the detector layout, it is not to be excluded that the GDML-based approach will be dropped in favor of some custom solution, thus gaining in flexibility while losing the no-more-crucial easyness of inspection.

Simulation input: Event generators Bruno can be interfaced to an event generator in two ways: either by direct embedding of the generator code or by using an intermediate exchange format.

In the latter case, the event generator is run as a different process and its results are saved in a file, which is then used to seed the full simulation job. Bruno presently supports two interchange formats: a plain ASCII file and a purely ROOT-based one, using persistified instances of the TParticle class.

9.3 Simulation output: Hits and MonteCarlo Truth

Hits from the different sub-detectors, which represent the simulated event as seen from the detector, are saved in the output (ROOT) file for further processing. Also the MonteCarlo Truth (MCTruth), intended as a summary of the event as seen by the simulation engine itself, i.e. with full detail, is saved and can be exploited in Bruno in several useful ways, the most important being the estimation of the particle fluxes at sub-detector boundaries by means of full snapshots taken at different scoring volumes.

9.4 Staged simulation

In particular in the design phase, a very frequent use-case will be the one in which a detector modifies its layout and wants to use full simulation to better evaluate the effect of the change. This would normally trigger the need of productions of large set of events which, with all sub-detectors working in parallel, may

lead to a large and inefficient use of computing resources. In Bruno this potential risk is mitigated by the implementation of staged simulation, where snapshots of particles taken at a specific detector boundaries, can be read back and used to start a new simulation process without the need of retracking particles through sub-detectors that sit at inner positions.

9.5 Interplay with fast simulation

As already mentioned in the introduction, full simulation can also be used to help the fast simulation programs in certain particular contexts. The design of the interaction region in particular has a deep influence on the background rates as seen from the detector. Simulating such a complex geometry with the required level of details would be beyond the purpose of the fast simulation. On the other hand, full simulation is not fast enough to generate the high statistics needed for signal events.

SuperB implements presently a hybrid approach to this problem:

- Bruno is used to simulate background events up to (including) the interaction region
- a snapshot of the simulation status is saved, along the lines of what already discussed above
- in order to gain time, the full simulation of the event can optionally be aborted once the relevant information has been saved

The result of this procedure is a set of *background frames*, which can be read back in the fast simulation program whose role would be, at this point, to propagate those particle through the simplified detector geometry and overlay the resulting hits to the ones coming from signal events.

This approach allows to combine the two simulations and effectively use each one only for the tasks it performs better.

Another aspect where the interplay between fast

and full simulation is needed is the evaluation of the neutron background. The idea is to make Bruno handle all particle interactions within the interaction region, as explained above, *plus* all neutron interactions afterwards. Neutrons are tracked in full simulation until they decay, and the decay products saved in the output file, as part of the background frame. Fast simulation can then include these interactions the overlaying procedure.

All these functionalities are presently implemented, and have been used in the recent productions.

9.5.1 The distributed production environment

9.5.2 The software development and collaborative tools

References

10 Mechanical Integration

This is the Integration Section (4-5 pages)

References

11 Budget and Schedule

The Super*B* detector cost and schedule estimates, presented in this chapter, rely heavily on experience with the *BABAR* detector at PEP-II. The reuse and refurbishing of existing components has been assumed whenever technically possible and financially advantageous. Though these Super*B* estimates are based on a bottoms-up evaluation using a detailed work breakdown schedule, it should be emphasized that the detector design is still incomplete, with numerous technical decisions remaining to be made, and limited detailed engineering to date, so that that cost and schedule can not yet be evaluated at the detailed level expected in a technical design report.

The costing model used here is similar to that already used for the Super*B* CDR. The components are estimated in two different general categories; (1) "LABOR" and, (2) M & S (Materials and Services). The "LABOR" estimates comprise two sub categories which are kept and costed separately as they have differing cost profiles; (1) EDIA (Engineering, Design, Inspection, and Administration) and (2) Labor (general labor and technicians). Estimates in both categories are presented in manpower work units (Man-Months) and not monetarized, as a monetary conversion can only be attempted after institutional responsibilities have been identified. M&S costs are given in 2010 Euros. since the project starting time cannot be defined at this time. The total project cost can be calculated, once the responsibilities are identified, by summing the monetary value of these three categories.

Given the long term nature of this multinational project, there are challenging general issues in arriving at appropriate costs; (1) fluctuating currency exchange rates, and (2) escalation. M&S costs and factory quotes that have been directly obtained in Euros can be directly quoted. M&S estimates in US dollars are translated from dollars to Euros using the exchange rate as of Jan 1, 2010 (.694155 Euros/US\$). For cost in Euros that were obtained in earlier years, the yearly escalation is rather small. For simplicity, we use a cost escalation rate of 2% per year which is consistent with the long term HICP (Harmonized Index of Consumer Prices) from the European Central bank. Costs given in 2007 Euros are escalated by the net escalation rate (1.061) for three years to arrive at the 2010 cost estimates given here [1].

For all items whose cost basis is BaBar, we accept the procedure outlined in the CDR which arrived at the 2007 costs in Euros. This procedure escalated the corresponding cost (including manpower) from the PEP-II and *BABAR* project from 1995 to 2007 using the NASA technical inflation index [2] and then converted from US Dollars to Euros using the average conversion rate over the 1999–2006 period [3]. The overall escalation factor in the CDR from 1995 dollars to 2007 Euro is thus $1.21 = 1.295 * 0.9354$.

Similarly, the replacement values ("Rep.Val.") of the reused components, *i.e.*, how much would be required to build them from scratch, as presented in separate columns of the cost tables, have been obtained by escalating the corresponding cost (including manpower) from the *BABAR* project from 1995 to 2007. Though it is tempting to sum the two numbers to obtain an estimate of the cost of the project if it were to be built from scratch, this procedure yields somewhat misleading results because of the different treatment of the manpower (rolled up in the replacement value; separated for the new cost estimate) and because of the double counting when the refurbishing costs are added to the initial values.

Contingency is not included in the tables. Given the level of detail of the cost estimates, a contingency of about 35% would be appropriate.

11.1 Detector Costs

The costs, detailed in the Table are presented for the detector subsystem at WBS level 3/4. The Super*B* detector is not completely defined: some components, such as the forward PID, have overall integration and performance implications that need to be carefully studied before deciding to install them; for some other components, such the SVT layer 0, promising new technologies require additional R&D before they can be definitively used in a full scale detector. The cost estimates list the different technologies separately, but the rolled-up value includes the baseline detector choice that is considered most likely to be used. Technologies that are not included in the rolled-up value are shown in italics in the table.

Table 6: SuperB detector budget.

WBS	Item	EDIA mm	Labor mm	M&S kEuro	Rep.Val. kEuro
1	SuperB detector	4063	2602	41282	47462
1.0	Interaction region	10	4	216	0
1.0.1	Be Beampipe	10	4	216	0
1.0.1.1	Vertex chamber design	4	0	0	0
1.0.1.2	Finalize Physics Req.mnts	1	0	0	0
1.0.1.3	Fab method	1	0	0	0
1.0.1.4	Design Review	1	0	0	0
1.0.1.5	Chamber detailing	2	0	0	0
1.0.1.6	Support procurement	2	0	4	0
1.0.1.7	Procure Beampipe Assembly	0	0	203	0
1.0.1.8	Procure Vx chamber Misc parts	0	0	10	0
1.0.1.9	Assemble Vx chamber, test, clean	0	2	0	0
1.0.1.A	Assemble Vx chamber fixtures	0	2	0	0
1.1	Tracker (SVT + Strip + MAPS)	295	381	5370	0
1.1.1	SVT	166	317	3605	0
1.1.1.1	Mechanical	14	186	333	0
1.1.1.2	Cooling	4	5	129	0
1.1.1.3	Silicon Wafers and Fanout	37	107	2202	0
1.1.1.4	On-detector electronics	69	11	844	0
1.1.1.5	Detector monitoring	4	4	77	0
1.1.1.6	Detector assembly	2	4	0	0
1.1.1.7	System Engineering	36	0	20	0
1.1.2	L0 Striplet option	23	33	452	0
1.1.2.1	Mechanical	7	17	50	0
1.1.2.2	Cooling	2	1	40	0
1.1.2.3	Silicon Wafers and Fanout	10	15	272	0
1.1.2.4	On-detector electronics	5	1	90	0
1.1.3	L0 MAPS option	106	32	1313	0
1.1.3.1	Mechanical	12	18	75	0
1.1.3.2	Cooling	2	2	80	0
1.1.3.3	MAPS Modules Components	92	12	1158	0
1.1.4	L0 Hybrid Pixel option	106	32	1403	0
1.1.4.1	<i>Mechanical</i>	12	18	75	0
1.1.4.2	<i>Cooling</i>	2	2	80	0
1.1.4.3	<i>Hybrid Pixel Modules Components</i>	92	12	1248	0
1.2	DCH	238	214	4240	0
1.2.1	System engineering	24	0	50	0
1.2.2	Endplates	16	6	550	0
1.2.3	Inner cylinder	8	2	167	0
1.2.4	Outer cylinder	6	2	100	0
1.2.5	Wire	4	6	257	0
1.2.6	Feedthroughs	9	10	366	0
1.2.A	Gas System	10	8	200	0
1.2.B	Test	6	9	40	0
1.3	PID	116	236	4107	7131
1.3.1	DIRC Barrel (Focusing DIRC)	116	236	4107	7131
1.3.1.1	Radiator Support Structure	4	4	7	2514
1.3.1.2	Radiator box/FBLOCK assembly	14	40	1989	4511
1.3.1.3	New Camera mechanical boxes	14	28	215	0
1.3.1.4	Photodetector assembly	18	32	1840	0
1.3.1.5	Calibration System	2	4	42	0
1.3.1.6	Mechanical Utilities	4	8	14	106

Continued on next page

Table 6 – continued from previous page

WBS	Item	EDIA mm	Labor mm	M&S kEuro	Rep.Val. kEuro
1.3.1.7	System Integration	60	120	0	0
1.4	EMC	227	375	9276	30120
1.4.1	Barrel EMC	20	5	171	30120
1.4.1.1	Crystal Procurement	0	0	0	20560
1.4.1.2	Light Sensors \& Readout	0	0	0	2570
1.4.1.3	Crystal Support Modules	0	0	0	2824
1.4.1.4	Barrel Structure	0	0	0	3306
1.4.1.5	Calibration Systems	0	0	0	625
1.4.1.6	Project Management	0	0	0	233
1.4.1.7	Barrel Transport	20	5	171	0
1.4.2	Forward EMC	171	312	8730	0
1.4.2.1	Crystal Procurement	25	102	7031	0
1.4.2.2	Light Sensors \& Readout	47	70	724	0
1.4.2.3	Crystal Support Modules	26	64	375	0
1.4.2.4	Endcap Structure	26	52	370	0
1.4.2.5	Calibration Systems	24	24	130	0
1.4.2.6	Project Management	24	0	100	0
1.4.3	Backward EMC	36	58	376	0
1.4.3.1	Scintillator	2	10	87	0
1.4.3.2	Radiator	1	4	16	0
1.4.3.3	Fibers	4	8	14	0
1.4.3.4	Photodetectors	2	5	38	0
1.4.3.5	Mechanical support	17	15	109	0
1.4.3.6	Front end electronics	8	15	91	0
1.4.3.7	Project Management	2	2	20	0
1.5	IFR	112	354	3600	0
1.5.1	Scintillators	0	0	335	0
1.5.2	WLS fibers	0	0	456	0
1.5.3	Photodetectors and PCBs	1	2	862	0
1.5.4	Mechanics (Production and QC)	24	94	76	0
1.5.5	Electronics	57	77	1871	0
1.5.6	Module Installation	30	181	0	0
1.6	Magnet	87	47	1639	10210
1.6.0	System Management	36	0	0	612
1.6.1	Superconducting solenoid	0	0	0	2421
1.6.2	Mag. Power/Protection	0	0	0	181
1.6.3	Cryogenics	34	36	1461	0
1.6.4	Cryo monitor/Control	17	11	178	0
1.6.5	Flux return	0	0	0	6481
1.6.6	Installation/test equipment	0	0	0	515
1.7	Electronics	994	342	7359	0
1.7.1	SVT	11	21	468	0
1.7.2	DCH	74	76	1390	0
1.7.3	PID Barrel (32k channels)	136	18	460	0
1.7.4	EMC	110	164	2272	0
1.7.5	IFR	38	51	1239	0
1.7.6	Infrastructure	4	12	171	0
1.7.7	Systems Engineering	12	0	0	0
1.7.8	Hardware Trigger	97	0	369	0
1.7.9	ETD (without Trigger)	512	0	990	0
1.8	Online System	912	24	1463	0
1.8.1	Event Flow	282	0	1183	0
1.8.2	Run Control / Slow Controls / ECS	270	0	37	0

Continued on next page

Table 6 – continued from previous page

WBS	Item	EDIA mm	Labor mm	M&S kEuro	Rep. Val. kEuro
1.8.3	Infrastructure	48	12	174	0
1.8.4	Software Triggers	216	0	0	0
1.8.5	Coordination and Commissioning	72	12	0	0
1.8.6	Online System R&D	24	0	69	0
1.9	Installation and integration	353	624	3830	0
1.9.1	Disassembly	95	161	510	0
1.9.2	Assembly	222	463	3320	0
1.9.3	Structural analysis	36	0	0	0
1.A	Project Management	720	0	180	0
1.A.1	Project engineering	300	0	100	0
1.A.2	Budget, Schedule and Procurement	300	0	40	0
1.A.3	ES \& H	120	0	40	0

[THESE SUBSECTIONS NEED TO BE UPDATED BY THE SYSTEMS]

Vertex Detector and Tracker System cost is estimated based on the experience of the *BABAR* detector. A detailed estimate is provided for the cost of the main detector (layers-1 to 5), while the layer-0 is analyzed separately, with two different estimates provided, corresponding to the triplets and the monolithic pixel option. The total cost is obtained summing the main detector cost to the MAPS layer0 cost.

Drift Chamber The DCH costing is based on an extrapolation to 2010 of the costs for the existing *BABAR* chamber, since as discussed in sec. 4 the main design elements are comparable. In particular, although the cell layout is still being finalized, the total cell count will be likely be about 25% larger than in *BABAR*. As a consequence, many related components, such as the length of wire, number of feedthroughs, duration of wire stringing, etc., can be reliably estimated. The endplates will be fabricated from carbon fiber composites: while this technique will require a somewhat longer period of R&D and engineering design, it is not foreseen to result in significantly larger production costs for the final endplates.

Particle Identification Barrel PID costs and replacement values are derived from *BABAR* costs as extrapolated to 2010. The main component of the new barrel FDIRC budget is its new optics. It consists of FBLOCK, the New Wedge and possibly a Micro-Wedge. We have contacted about 12 optics companies and received 4 preliminary bids. We use the lowest bid in the present budget projection. The chosen company had DIRC experience previously. We are now preparing the final drawings and hope to go for a final bidding to refine the values further. The photon detector cost was estimated based on the Hamamatsu bid for 600 H-8500 MaPMTs. Regarding the forward PID system, no detailed budget is provided in this document: various

options are still being studied and it has not been decided yet to build one such detector. Should this happen, the forward PID detector should cost must less than the barrel one.

Electromagnetic Calorimeter There are four components to the calorimeter cost: (i) the barrel calorimeter from BaBar; (ii) the forward calorimeter; (iii) the replacement of the front-end preamps in the barrel; and (iv) the backward calorimeter. As described in the calorimeter section, there are a number of uncertainties remaining in the design. The present estimate represents an estimate of costs for our baseline design.

The reuse value of the barrel calorimeter is based on the actual cost of the barrel escalated for inflation from the time of construction to the current year. Manpower estimates for the barrel construction were obtained by using the costs for ED&I and Labor, knowledge of the mix of engineers and technicians who contributed to the design and fabrication of individual components, and knowledge of their salaries. Manpower and costs for engineering and tooling required for the removal and transport of the barrel EMC from SLAC are engineering estimates.

The main cost driver for the forward endcap is the cost of LYSO crystals. This is estimated based on guideline quotes from vendors. The next largest element is the APD photodetectors, with a cost based on a quote from the vendor. The estimate for the crystal support modules is based on costs for the beam test prototype. Estimates for the remaining smaller items are based on estimator experience and judgement.

The cost estimate for replacing the preamplifiers in the barrel calorimeter is based on the endcap preamplifier cost as well as the cost of dealing with the mechanical issues.

For the backward endcap, the scintillator, lead, wavelength-shifting fiber, and readout MPPC costs are all based on vendor quotes, as well as some of the other minor materials. Other items are based on experience and estimator judgement.

Instrumented Flux Return The IFR cost is based on quotations received for the prototype construction appropriately scaled to the real detector dimension. While the active part of the detector is quite inexpensive the total cost is driven by the electronics and the photodetectors. The current baseline design allow the reuse of the *BABAR* iron structure with some modification that need to be taken into account. Manpower and cost for engineering and module installation is based on the *BABAR* experience. No contingency has been applied.

Electronics, Trigger, DAQ and Online The cost for the Electronics and Trigger subsystems were estimated with a combination of scaling from the *BABAR* experience and from direct estimates. For items expected to be similar to those used in *BABAR* (such as infrastructure, high and low voltage or the L1 trigger) we made the estimation by scaling the costs from *BABAR*. The same methodology was used to estimate the EDIA and labor costs for the Online system, however some modifications based on “lessons learned” were applied, in particular, we are including development work that in our opinion should have been centralized across sub-detectors in *BABAR* (but wasn’t) and work that should have been done upfront but was only done or completed as part of *BABAR* Online system upgrades.

The readout systems for which the higher data rates require redesigned electronics were estimated from the number of different components and printed circuit boards, and their associated chip and board counts. This is also true for the new detectors (forward EMC, backward EMC, forward PID) and for the elements of the overall system architecture (which is very different from that of *BABAR*).

The hardware cost estimates for the online computing system (including the HLT farm) are - very conservatively - based on the current prices of hardware necessary to build the system, with the assumption that Moore’s Law will result in future systems with the same unit costs but higher performance. This is justified

by our observation that for COTS components, constraints from system design, topology and networking are more likely to set minimum requirements for the *number* of devices than for the per-device performance.

Transportation, installation, and commissioning Installation and commissioning estimates, including disassembling and reassembling *BABAR* are based on the *BABAR* experience, using a detail schedule of activities and corresponding manpower requirement.

Although transportation costs are expected to be significant, they are not included in this estimates, because of lack of detailed information at the time of writing.

11.2 Schedule

The accelerator and detector construction schedule is shown in Fig. ???. The present PEP-II accelerator (2.2 km with two rings) was built in about four years, but the tunnel already existed. For the Super*B* schedule, we have added an additional year for tunnel and support building construction. The construction starts with environmental, design finalization, and contract bidding. The accelerator infrastructure is constructed with a phased approach, moving around the ring. The accelerator components are installed, again with a phased approach around the ring followed by system checkout. Finally, beam commissioning starts, as well as first beam collisions. The detector schedule is dominated by the time required to disassemble the *BABAR* detector, transport it to the new site, and reassemble it. The total construction and commissioning time is estimated to be a little over 5 years.

References

- [1] Euro Inflation Rates, <http://www.ecb.int/stats/prices/hicp/html/index.en.html>

- [2] NASA Inflation Calculator, <http://cost.jsc.nasa.gov/inflation/nasa/inflateNASA.html>
- [3] Federal Reserve Foreign Exchange Rates, <http://www.federalreserve.gov/releases/g5a/>